EFFECTS OF CHIRALITY AND COHERENCE ON LIGHT SCATTERING

A Dissertation

by

JIANPING LIU

Submitted to the Office of Graduate and Professional Studies of
Texas A&M University
in partial fulfillment of the requirements for the degree of

DOCTOR OF PHILOSOPHY

Chair of Committee,	George W. Kattawar
Committee Members,	Roland E. Allen
	Edward Fry
	Ping Yang
Head of Department,	George R. Welch

August 2014

Major Subject: Physics

ABSTRACT

In the first part of this dissertation, we study the light scattering properties of particles with chiral structures. Special attention is paid to the dinoflagellates, known for their circular polarization effects and as a causative agent of the red tide. Based on experimental observations and previous works, we build a helical plywood liquid crystal model for the nucleus of dinoflagellates, and apply the Discrete Dipole Approximation (DDA) method to investigate the light scattering properties of dinoflagellates. The backscattering signals display strong sensitivity to the wavelength of the incident beam, and they are most prominent when the wavelength matches the pitch of the chromatic helix. Our results indicates a promising means to monitor and detect the specific species of dinoflagellates.

In the second part of the dissertation, we investigate the the problem of light scattering when the incident light has finite coherence length. The conventional Lorenz-Mie theory and DDA method are generalized to include a partially spatially coherent source. The formalism is applied to atmospheric particles such as water droplets and hexagonal ice crystals. Given that the solar source is partially coherent, our results have practical implications in remote sensing. Using the same technique, we also study the effects of incoherence on particle characterization using digital holographic microscopy. We show that holography is rather robust against incoherence and demonstrate the possibility of retrieving the coherence length of the illumination.

DEDICATION

To my family and friends.

ACKNOWLEDGEMENTS

First of all, I would like to thank my advisor Dr. George Kattawar for his guidance and support in the past two years. I also want to thank my thesis committee members, Dr. Ping Yang, Dr. Roland Allen and Dr. Edward Fry, for their help and suggestions on my thesis.

I also want to take this opportunity to thank my formal advisor Dr. Artem Abanov and co-advisor Jairo Sinova for their support during the first two years and their tremendous understanding when I tried to switch my research field.

I would like to thank my colleagues and friends, Meng Gao, Xin Huang, Bingqiang Sun, Angela Marotta, Dayou Chen, Bi Lei, Chao Liu, for their countless help. It was their kindness and patience that introduced me to this new field.

I also want to thank my friends here, especially Zilong Chang. They made my life in College Station much easier and happier.

I want to express my sincere gratitude to my family in China. Their love and support has been with me for the last four years. Special thank goes to my girlfriend Mengxiao for her companionship and love.

TABLE OF CONTENTS

Page

ABSTRACT ii

DEDICATION iii

ACKNOWLEDGEMENTS iv

TABLE OF CONTENTS v

LIST OF FIGURES vii

LIST OF TABLES xi

1. INTRODUCTION 1

    1.1 Chirality 1
    1.2 Coherence 3

2. FORMALISM 7

    2.1 Scalar Description of Light: Radiance and Irradiance 7
    2.2 Vector Description of Light: Stokes Vector 8
    2.3 Single Particle Scattering: Amplitude Matrix and Mueller Matrix 11
    2.4 Properties of Mueller Matrices 13
    2.5 Mirror Symmetry and Chirality 15

3. NUMERICAL METHODS 19

    3.1 Lorenz-Mie Theory 19
    3.2 Discrete Dipole Approximation Method 23

4. DETECTION OF DINOFLAGELLATES BY THE LIGHT SCATTERING PROPERTIES OF THE CHIRAL STRUCTURE OF THEIR CHROMOSOMES . . . 25

    4.1 Introduction 26
    4.2 Models and Methods 28
        4.2.1 Model of a Cell 28
        4.2.2 Model of a Chromosome 30
    4.3 Results of Single Chromosome Scattering 33

4.3.1 Light propagating along the chromosome axis 33
4.3.2 Light scattering from oriented chromosomes 35
4.3.3 Light scattering from orientation averaged chromosomes 35
4.4 Results of Nucleus Scattering 40
4.4.1 Light Scattering from a Single Immobilized Dinoflagellate 40
4.4.2 Light Scattering from a Suspension of Dinoflagellates 43
4.4.3 Effects of Coherence and Interactions 46
4.5 Conclusions 46

5. SCATTERING OF PARTIALLY COHERENT ELECTROMAGNETIC BEAMS BY WATER DROPLETS AND ICE CRYSTALS 48

5.1 Introduction 48
5.2 Scattering of Partially Coherent Light by a Sphere 50
5.2.1 Theory of Coherence 50
5.2.2 Incident Light 51
5.2.3 Scattered Light 54
5.2.4 Mueller Matrix 59
5.2.5 Spectral Degree of Coherence 61
5.2.6 Water Droplets and Ice Crystals 62
5.3 DDA Simulation 63
5.4 Results 65
5.5 Conclusions and Discussions 75

6. EFFECTS OF INCOHERENCE ON PARTICLE CHARACTERIZATION USING DIGITAL HOLOGRAPHIC MICROSCOPY 77

6.1 Introduction 77
6.2 Theory 78
6.3 Numerical results 82
6.4 Conclusions 89

7. CONCLUSIONS 90

REFERENCES 92

APPENDIX A. THE COHERENCE LENGTH OF SUNLIGHT 99

LIST OF FIGURES

FIGURE Page

1.1 Left: the TEM images of cross-sections of *P. micans* (from [1]). Bars = 200 nm. Right: the Plywood model of Bouligand (from [1]). This figure is reprinted from Journal of Ultrastructure and Molecular Structure Research, **97**, 10-20, 1986, A. Gautier, L. Michel-Salamin, E. Tosi-Couture, A. W. McDowall and J. Dubo-chet, "Electron microscopy of the chromosomes of dinoflagellates in situ: confirmation of bouligand's liquid crystal hypothesis", Copyright 1986, with permission from Elsevier. 2

1.2 Left: the intensity distribution of a coherent Gaussian beam. Right: the intensity distribution of a partially coherent Gaussian beam simulated using the numerical method described in Chapter 5. 4

1.3 The angular intensity distribution of the scattered light by a sphere (from [2]). The sphere has radius $a = 4\lambda$ and refractive index $n = 1.5$. Here σ_μ denotes the spatial coherence length. This figure is reprinted from Phys Rev Lett, **104**, 173902, 2010, T. van Dijk, D. G. Fischer, T. D. Visser, and E. Wolf, " Effects of spatial coherence on the angular distribution of radiant intensity generated by scattering on a sphere", Copyright 2010, with permission from American Physical Society. 5

1.4 Fitting simulated hologram (right) to measured hologram (left) (from [3]). This figure is reprinted from Opt Express, **15**, 18275-82, 2007, S. H. Lee, Y. Roichman, G. R. Yi, S. H. Kim, S. M. Yang, A. van Blaaderen, P. van Oostrum, and D. G. Grier, "Characterizing and tracking single colloidal particles with video holographic microscopy", Copyright 2007, with permission from American Optical Society. 6

4.1 (a) Transmission electron microscopy of a longitudinal section of *K. brevis* taken from [4]. The bar is 1 μm. (b) A model of the nucleus, where the chromosomes are modeled by capsules of the same size that are randomly positioned and oriented within a fixed space without touching each other. (c) The TEM image of a separated nucleus of *K. brevis* taken from [5]. The bar here is 1 μm. (d) The TEM image of a nucleus of *P. micans* from [1]. The bar is 1 μm. 29

4.2 (a) The liquid crystal model of dinoflagellate chromosome, where different colors indicate different orientations of fibrils in each layer. The diameter of the chromosome is 1 μm (480 dipoles), and its length is 2 μm (960 dipoles). In each layer, there are up to 20 fibrils, and each fibril has a diameter of 21 nm (10 dipoles). A total of 8 turns are considered and the twist angle we used is 45°. (b) A simplified model of (a), where the color scheme has the same meaning. The parameters are: chromosome diameter and length are 0.5 μm (100 dipoles) and 1 μm (200 dipoles), respectively, up to 5 fibrils in each layer, fibril diameter 50 nm (10 dipoles), twist angle 45° and 2 turns. 31

4.3 The Mueller matrix elements calculated using model (Fig. 4.2. (a)), where the light propagates along the chromosome axis (z-direction). The wavelength takes value from 0.20, 0.25, 0.30, and 0.50 μm. The chromosome has diameter 1.0 μm, length 2.0 μm and pitch 0.25 μm. The refractive index used is $1.2 + 0.01i$, and the scattering plane is yz-plane. 34

4.4 The Mueller matrix elements calculated using model (Fig. 4.2. (a)) when the wavelength is 0.25 μm. The orientation of the chromosome is defined by Euler angles α, β and γ, with α and γ fixed to be 0, and β taking values 0°, 15°, 30°, 45°, and 60°. The chromosome has diameter 1.0 μm, length 2.0 μm and pitch 0.25 μm. The refractive index used is $1.2 + 0.01i$, and the scattering plane is yz-plane. 36

4.5 Same as Fig. 4.4, except that the wavelength is 0.50 μm. 37

4.6 Mueller matrix elements from a single chromosome calculated using model (Fig. 4.2. (a)) when the wavelength takes values 0.20 μm, 0.25 μm, 0.30 μm and 0.50 μm, and in all cases the orientation of the chromosomes is averaged. The chromosome has diameter 1.0 μm, length 2.0 μm and pitch 0.25 μm. The refractive index used is $1.2 + 0.01i$. 39

4.7 Mueller matrix elements from a fixed dinoflagellate calculated using the nucleus model (Fig. 4.1. (b)) and the simplified chromosome model (Fig. 4.2. (b)). The red line is the case when the twist angle is 45°, while the blue line is the one with random twist angle in each layer. In both cases, the light wavelength is 0.5 μm, which matches the pitch of the helical structure. The nucleus has diameter 4.0 μm. The chromosome has diameter 0.5 μm, length 1.0 μm and pitch 0.5 μm. The refractive index used is $1.2 + 0.01i$ and the scattering plane is yz-plane. 41

4.8 Mueller matrix elements from a fixed dinoflagellate calculated using the nucleus model (Fig. 4.1. (b)) and the simplified chromosome model (Fig. 4.2. (b)). Three different wavelengths are considered, 0.25, 0.50 and 1.0 μm. The nucleus has diameter 4.0 μm. The chromosome has diameter 0.5 μm, length 1.0 μm and pitch 0.5 μm. The refractive index used is $1.2 + 0.01i$ and the scattering plane is yz plane. 42

4.9 Mueller matrix elements from a single orientation averaged chromosome calculated using model (Fig. 4.2. (b)) when the wavelength is 0.3, 0.4, 0.5, 0.6, 0.7, 0.8, and 0.9 μm. The chromosome has diameter 0.5 μm, length 1.0 μm and pitch 0.5 μm. The refractive index used is $1.2 + 0.01i$. 44

4.10 Mueller matrix elements from a fixed dinoflagellate calculated using the nucleus model (Fig. 4.1. (b)) and the simplified chromosome model (Fig. 4.2. (b)). The red line is the exact solution using ADDA, while the blue line is the result that all chromosomes are treated independently (Born approximation). In both cases, the light wavelength is 0.5 μm, which matches the pitch of the helical structure. The nucleus has diameter 4.0 μm. The chromosome has diameter 0.5 μm, length 1.0 μm and pitch 0.5 μm. The refractive index used is $1.2 + 0.01i$ and the scattering plane is yz-plane. 45

5.1 The geometry of Mie scattering, where $\hat{\mathbf{u}}'$ is the incident direction, $\hat{\mathbf{u}}$ is the scattering direction, and Θ is the scattering angle. 55

5.2 Scattering of one plane wave component of the partially coherent beam, where $\hat{\mathbf{u}}'$ is the incident direction, $\hat{\mathbf{u}}$ is the scattering direction, and Θ is the scattering angle. i_1 is the angle between the meridian plane containing $\hat{\mathbf{u}}'$ and the scattering plane, and i_2 is the angle between the meridian plane containing $\hat{\mathbf{u}}$ and the scattering plane. 56

5.3 Mueller matrix elements for a sphere of radius $a = \lambda$ and refractive index $n = 1.5$. The coherence length σ_μ has values of λ, 4λ, and 10λ. 66

5.4 Comparison of Mueller matrix elements computed from DDA and Mie methods. Two cases, $\sigma_\mu = \lambda$ and 4λ are simulated. The remaining parameters are the same as Fig. 5.3. 67

5.5 Mueller matrix elements for a sphere in the backward direction ($180°$). The coherence length $\sigma_\mu = \lambda$ is from 0 to 10λ. The remaining parameters are the same as Fig. 5.3. 68

5.6 The spectral degree of coherence of the scattered field from a sphere. θ is the angle between scattering direction and the $+z$ direction. Four cases, including the coherent case are simulated. The parameters are the same as Fig. 5.3. 69

5.7 Mueller matrix elements for a water droplet of size parameter $x = 80$ and refractive index $n = 1.33$. The coherence length parameter σ_μ has values of 5, 10 and 100. 71

5.8 Mueller matrix elements for a hexagonal ice crystal with size parameter $kL = 2ka = 150$, where L is the height and a is the semi-width, and refractive index $n = 1.31$. The coherence length parameter $k\sigma_\mu$ has values of 5, 10 and 100. 72

5.9 Mueller matrix elements for a water droplet in the backward direction (180°). The coherence length parameter $k\sigma_\mu$ is from 0 to 100. The size parameter of the water droplet is $x = 80$ and the refractive index is $n = 1.33$. 73

5.10 Mueller matrix elements for a hexagonal ice crystal in the backward direction (180°). The coherence length parameter $k\sigma_\mu$ is from 0 to 100. The remaining parameters are the same as Fig. 5.8. 74

6.1 The radial profiles at various coherence lengths. The particle has radius $a = 1\ \mu m$, refractive index $n = 1.55$ and axial position $z_p = 20\ \mu m$. . . . 83

6.2 Holograms and their corresponding radial profiles. (a) $\sigma_\mu = 2\ \mu m$, (b)$\sigma_\mu = 1\ \mu m$, (c)$\sigma_\mu = 0.5\ \mu m$. The rest of the parameters are the same as Fig. 6.1. 84

6.3 Retrieved radii at different coherence lengths. Three cases are considered, a = 1, 2 and 4 μm. The particle has fixed refractive index $n_p = 1.55$ and axial position $z_p = 20\ \mu m$. 86

6.4 Retrieved refractive indices at different coherence lengths. Three cases are considered, n_p = 1.55, 1.80 and 2.00. The particle has fixed radius $a_p = 1$ μm and axial position $z_p = 40\ \mu m$. 87

6.5 Retrieved axial positions at different coherence lengths. Three cases are considered, z_p = 20, 40 and 60 μm. The particle has fixed refractive $n_p = 1.55$ and radius $a_p = 1.0\ \mu m$. 88

LIST OF TABLES

TABLE Page

6.1 Retrieved coherence lengths compared with correct values. The parameters are the same as Fig. 6.1. 85

1. INTRODUCTION

This thesis is dedicated to two largely overlooked topics in the study of light scatterings: the chiral structures of the scatterers and the incoherence of the incident light.

1.1 Chirality

Harmful algal blooms (HABs) have continuously been global issues, especially in North America due to the red tides in the Gulf of Maine and Florida, presenting environmental and economic risks to the human beings around the affected area [6, 7, 8]. The causative agents of HABs, mostly marine plankton dinoflagellates such as *Alexandrium fundyense* and *Karenia brevis*, have been extensively studied by biologists [9, 4, 5, 1, 10]. Highly ordered chromosomes inside the relatively oversized nuclei were observed (see Fig. 4.1 in Chapter 4), and patterns like bands and arches were also shown in transmission electron microscopy images (see Fig. 1.1). It was later demonstrated that these features in chromosomes could be perfectly explained using the plywood model proposed by Bouligand [9] (see Fig. 1.1). According to the model, the DNA molecules are arranged in such a way that they form fibrils lying on parallel parallels that are perpendicular to the chromosome's axis, and the fibrils rotate along the axis in a helical way. In the light scattering experiments conducted subsequently by Shapiro *et al.* using dinoflagellates [11, 12], large circular polarization effects were observed and the chromosomes are believed to be responsible. As a result of breaking mirror symmetry, chiral particles like the chromosomes of dinoflagellates have a particular property called circular intensity differential scattering (CIDS) (see Section 2.5), which characterizes the ability of a particle to scatter left and right circularly polarized light differently. Direct connection with the reduced Mueller matrix element S_{14}/S_{11} (Section 2.5) makes the measurement of CIDS accessible, ensuring straightforward quantification of the chirality of a particle.

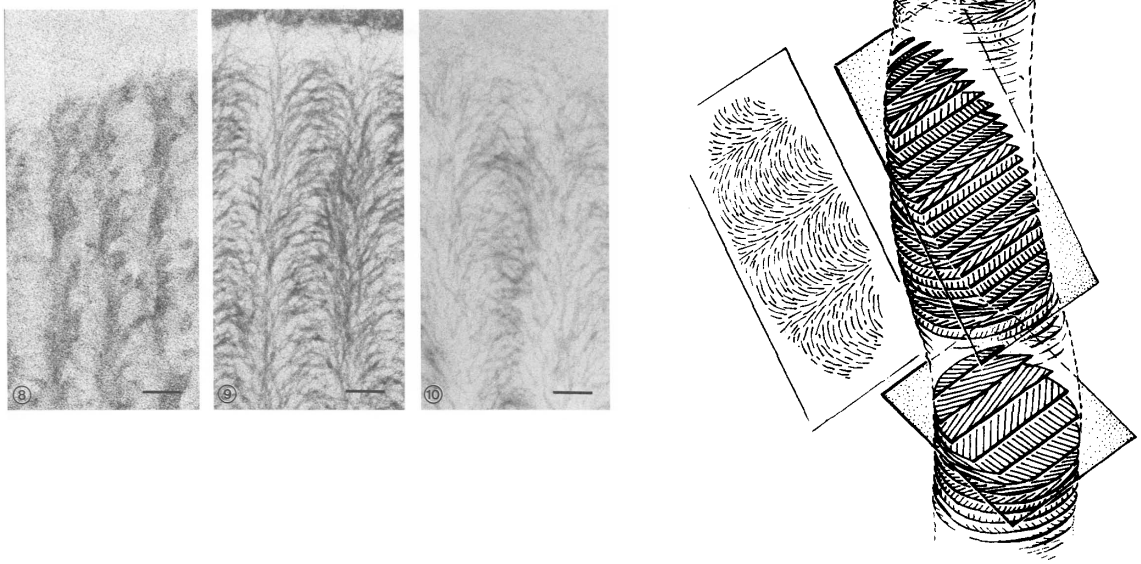

Figure 1.1: Left: the TEM images of cross-sections of *P. micans* (from [1]). Bars = 200 nm. Right: the Plywood model of Bouligand (from [1]). This figure is reprinted from Journal of Ultrastructure and Molecular Structure Research, **97**, 10-20, 1986, A. Gautier, L. Michel-Salamin, E. Tosi-Couture, A. W. McDowall and J. Dubo-chet, "Electron microscopy of the chromosomes of dinoflagellates in situ: confirmation of bouligand's liquid crystal hypothesis", Copyright 1986, with permission from Elsevier.

Despite considerable effort to model helical structures in biological particles [11, 12, 13, 14, 15, 16, 17, 18, 19], both analytically and numerically, the models used in previous works tended to be oversimplified, failing to achieve agreements with measurements. Instead of using a thin helix as was widely adopted previously, we attempt to model the chromosomes of dinoflagellates based on the Plywood model (see Fig. 4.2). Furthermore, by representing the nucleus as a collection of identical chromosomes that are randomly oriented and positioned, it also enables the study of interactions and correlations, which were overlooked in previous works. Therefore, through implementing a more realistic description of the dinoflagellate, we expect to gain more insight of its optical properties and make reliable predictions. In this dissertation, we will study the light scattering of both a single chromosome and a nucleus, in hopes of detecting and categorizing each specific specie of dinoflagellate (see Chapter 4).

1.2 Coherence

Numerous methods and techniques have been developed to study the problems of light scattering, such as Lorenz-Mie theory [20], the discrete dipole approximation (DDA) method [21, 22, 23], and the finite-different time-domain (FDTD) method [23]. However, these theories failed to consider the effects of the finite coherence length of incident light. The stochastic nature of the light source (such as a thermal source), and the randomness of the medium (such as a turbulent fluid) through which the light passes , would render any light beams partially coherent (see Fig. 1.2). On the basis of statistical theory, Wolf *et al.* have long established [24, 25, 26] the foundation of optical coherence theory, which becomes the language to describe light beams of arbitrary degree of coherence. Apart from some limited applications of this theory to light scattering by [27, 28], general investigation of light scattering using partially coherent light has not been conducted. Recent progress was made by van Dijk *et al.* [2] and Fischer *et al.* [29], who studied the effects of

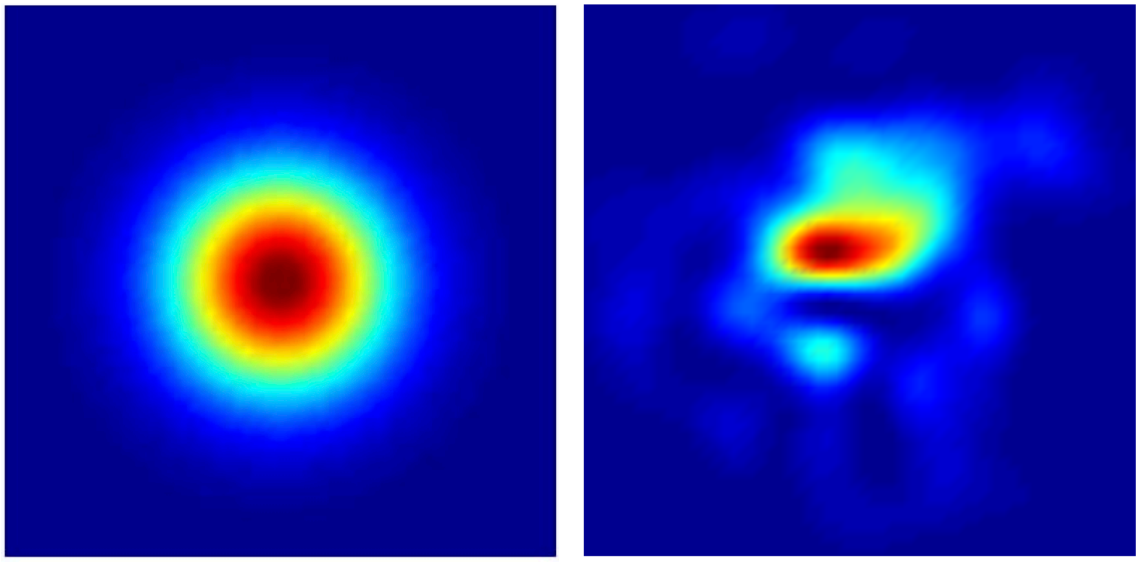

Figure 1.2: Left: the intensity distribution of a coherent Gaussian beam. Right: the intensity distribution of a partially coherent Gaussian beam simulated using the numerical method described in Chapter 5.

transverse coherence length on the angular distribution of light scattered by a sphere. They managed to show that the angular distribution of scattered light is smoothed out gradually when reducing the coherence length (see Fig. 1.3). A critical drawback of this work was that scalar a incident field was used, thus only the radiation intensity can be obtained. By a using vector field, we extended the Loerenz-Mie theory and the DDA method to include partially coherent incident fields, and compute all 16 Mueller matrix elements (see Chapter 5).

We then applied the developed formalism to the problem of particle characterization using digital holographic microscopy (DHM), a technique to obtain the parameters of a sphere by fitting the numerically simulated hologram to the experimentally measured hologram (see Fig. 1.4). Based on the Lorenz-Mie theory, the DHM has proved to be efficient and accurate to extract the parameters of a particle such as the radius, the refractive index, and the three-dimensional position [3, 30]. In this dissertation, we attempt to

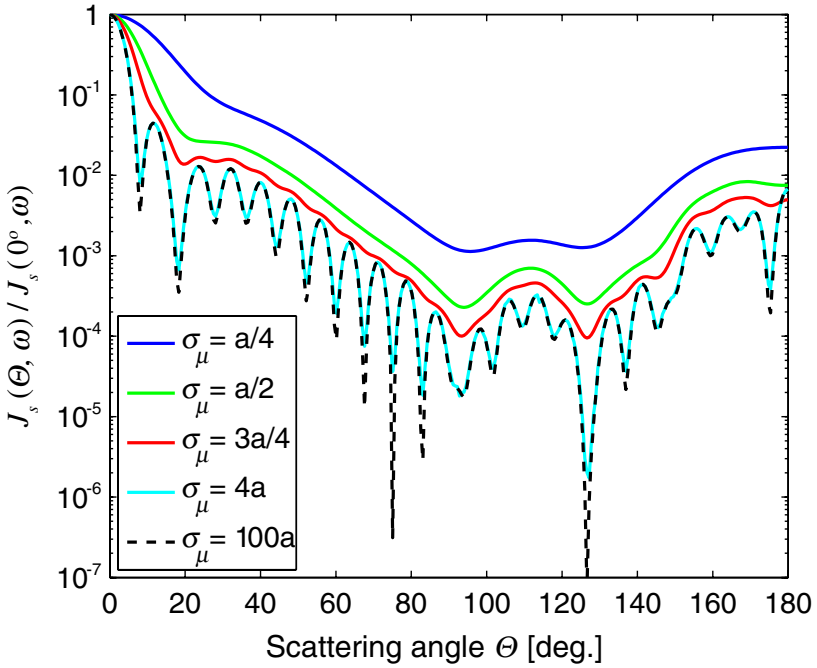

Figure 1.3: The angular intensity distribution of the scattered light by a sphere (from [2]). The sphere has radius $a = 4\lambda$ and refractive index $n = 1.5$. Here σ_μ denotes the spatial coherence length. This figure is reprinted from Phys Rev Lett, **104**, 173902, 2010, T. van Dijk, D. G. Fischer, T. D. Visser, and E. Wolf, " Effects of spatial coherence on the angular distribution of radiant intensity generated by scattering on a sphere", Copyright 2010, with permission from American Physical Society.

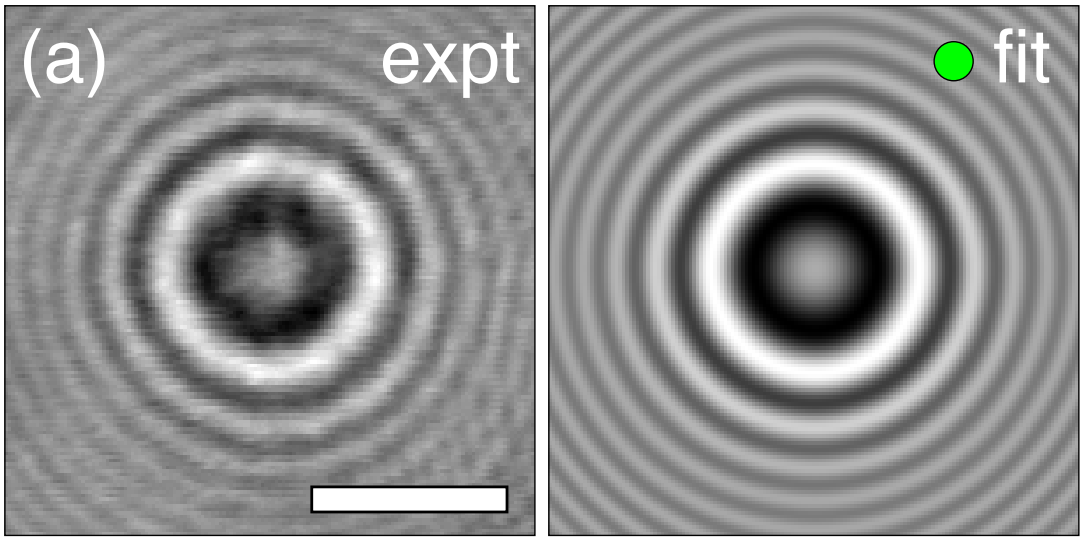

Figure 1.4: Fitting simulated hologram (right) to measured hologram (left) (from [3]). This figure is reprinted from Opt Express, **15**, 18275-82, 2007, S. H. Lee, Y. Roichman, G. R. Yi, S. H. Kim, S. M. Yang, A. van Blaaderen, P. van Oostrum, and D. G. Grier, "Characterizing and tracking single colloidal particles with video holographic microscopy", Copyright 2007, with permission from American Optical Society.

investigate the effects of incoherence on particle characterization using DHM by replacing the plane wave light beam with a partially coherent light beam (see Chapter 6). We also studied the minimum degree of coherence required for the light beam before this method breaks down.

2. FORMALISM

The primary purpose of this chapter is to establish the terminology and notations we are going to use to describe electromagnetic field and light scatterings. The formalism introduced here will become the basic language for future chapters. Here, we adopt the notaions used in van de Hulst [31], Bohren and Clothiaux [32] and Rybicki and Lightman [33].

2.1 Scalar Description of Light: Radiance and Irradiance

Since most radiation from natural sources is highly incoherent due to multiple scatterings, a scalar description of light is not only a major simplification but also can be a sufficiently accurate representation of theelectromagnetic field in most cases. Radiometry uses scalar quantities to characterize the energy distribution of the radiation field. One of the most important quantities is the *radiance* $L\left(\mathbf{r}, \hat{\mathbf{\Omega}}, \nu, t\right)$ that measures the radiation strength at position $\mathbf{r}$, direction $\hat{\mathbf{\Omega}}$, frequency ν and time t. Consider a detector with surface area A and normal direction $\hat{\mathbf{n}}$, that only collects radiation within solid angle $\Delta\Omega$ around direction $\hat{\mathbf{\Omega}}$ and only responds to radiation in the frequency interval $(\nu, \nu + \Delta\nu)$. Then during time interval Δt, the detector will receive radiation energy

$$\Delta E = L\left(\mathbf{r}, \hat{\mathbf{\Omega}}, \nu, t\right) \cos\theta A \Delta\Omega \Delta\nu \Delta t, \tag{2.1}$$

where θ is the angle between direction $\hat{\mathbf{n}}$ and $\hat{\mathbf{\Omega}}$. The radiance is an intrinsic quantity of the radiation field that is independent of the detector. It can be shown [33] that the radiance is invariant from the source to any points along any specific direction if no scattering or absorption occurs during the path.

Another important quantity is *irradiance* which is defined as the energy flux passing

through a unit area A with normal $\hat{\mathbf{n}}$. It can be expressed as an angular integral over a hemisphere

$$F = \int_{2\pi} L\left(\hat{\mathbf{\Omega}}\right) \cos\theta d\Omega, \tag{2.2}$$

where θ is the angle between solid angle $\hat{\mathbf{\Omega}}$ and surface normal $\hat{\mathbf{n}}$.

An interesting case is when the radiation field is isotropic, which means the radiance is independent of direction $\hat{\mathbf{\Omega}}$. Using Eq. (2.2), the irradiance or flux can be calculated

$$F = L \int_0^{2\pi} \int_0^{\pi/2} \cos\theta \sin\theta d\theta d\phi = \pi L. \tag{2.3}$$

2.2 Vector Description of Light: Stokes Vector

In the previous section, electromagnetic radiation is assumed to be incoherent and represented as scalar quantities. Due to the vector nature of the electromagnetic field, generally we have to consider the polarization of radiation. To conveniently describe a beam of light, we first define a plane of reference in such a way that the direction of propagation is on the plane of reference. Let $\hat{\mathbf{r}}$ be the unit vector perpendicular to the plane and $\hat{\mathbf{l}}$ be the unit vector perpendicular both to the plane and direction of propagation. The handedness of the system is chosen in the sense that $\hat{\mathbf{r}} \times \hat{\mathbf{l}}$ is along the direction of propagation. Since the electric field is transverse, it can be decomposed into two perpendicular components

$$\mathbf{E} = E_l \hat{\mathbf{l}} + E_r \hat{\mathbf{r}}, \tag{2.4}$$

It is more conventional to write it as a column vector

$$\mathbf{E} = \begin{pmatrix} E_l \\ E_r \end{pmatrix}. \tag{2.5}$$

Since it is difficult to measure the phase of the electric field, it is more practical to use the so-called Stokes vector $\mathbf{I} = (I, Q, U, V)^T$. Each component is defined below

$$I = \langle E_l^* E_l + E_r^* E_r \rangle, \tag{2.6}$$

$$Q = \langle E_l^* E_l - E_r^* E_r \rangle, \tag{2.7}$$

$$U = \langle E_l^* E_r + E_r^* E_l \rangle, \tag{2.8}$$

$$V = i\langle E_l^* E_r - E_r^* E_l \rangle, \tag{2.9}$$

where asterisk denotes the complex conjugate and $\langle \quad \rangle$ denotes time average. It can be shown that the sufficient and necessary condition that a 4-component vector $(I, Q, U, V)^T$ is a Stokes vector is

$$I \geq 0, \tag{2.10}$$

$$I^2 \geq Q^2 + U^2 + V^2. \tag{2.11}$$

Note that when the light beam is completely unpolarized, the Stokes vector is reduced to $\mathbf{I} = (I, 0, 0, 0)$. For a completely polarized beam, the inequality in Eq. (2.11) becomes an equality, i.e. $I^2 = Q^2 + U^2 + V^2$. To more generally characterize the state of polarization, we define the degree of polarization as

$$P = \frac{\sqrt{Q^2 + U^2 + V^2}}{I}, \tag{2.12}$$

which is bounded by $0 \leq P \leq 1$, with 0 being completely unpolarized and 1 being completely polarized. Based on Eq. (2.10), it is not difficult to notice that an arbitary light beam characterized by Stokes vector $\mathbf{I} = (I, Q, U, V)$ can be representated as a superposition of one completely unpolarized and one completely polarized beam [32], i.

e.

$$\begin{pmatrix} I \\ Q \\ U \\ V \end{pmatrix} = \begin{pmatrix} I_u \\ 0 \\ 0 \\ 0 \end{pmatrix} + \begin{pmatrix} I_p \\ Q \\ U \\ V \end{pmatrix}, \tag{2.13}$$

where

$$I_u = I - \sqrt{Q^2 + U^2 + V^2}, \tag{2.14}$$

$$I_p = \sqrt{Q^2 + U^2 + V^2}. \tag{2.15}$$

As we will constantly encounter in Chapter. 4, the rotation of the plane of reference introduces a corresponding transformation to the electric field. Suppose the plane of reference rotates around the direction of propagation by angle θ in the counterclockwise direction, then unit vectors $\hat{\mathbf{l}}$ and $\hat{\mathbf{r}}$ are rotated according to

$$\begin{pmatrix} \hat{\mathbf{l}}' \\ \hat{\mathbf{r}}' \end{pmatrix} = \begin{pmatrix} \cos\theta & \sin\theta \\ -\sin\theta & \cos\theta \end{pmatrix} \begin{pmatrix} \hat{\mathbf{l}} \\ \hat{\mathbf{r}} \end{pmatrix}. \tag{2.16}$$

Similarly, the electric field $(E_l, E_r)^T$ transforms as

$$\begin{pmatrix} E_l' \\ E_r' \end{pmatrix} = \begin{pmatrix} \cos\theta & -\sin\theta \\ \sin\theta & \cos\theta \end{pmatrix} \begin{pmatrix} E_l \\ E_r \end{pmatrix}. \tag{2.17}$$

Substituting Eq. (2.17) into Eq. (2.6 – 2.9), we obtain the transformation of Stokes vector

$$\mathbf{I}' = \mathbf{L}(\theta) \cdot \mathbf{I}, \tag{2.18}$$

where

$$\mathbf{L}(\theta) = \begin{pmatrix} 1 & 0 & 0 & 0 \\ 0 & \cos 2\theta & -\sin 2\theta & 0 \\ 0 & \sin 2\theta & \cos 2\theta & 0 \\ 0 & 0 & 0 & 1 \end{pmatrix}. \tag{2.19}$$

2.3 Single Particle Scattering: Amplitude Matrix and Mueller Matrix

Now we consider the scattering of a monochromatic plane wave by a single particle of arbitrary shape and composition. The incident beam propagating along the $+z$ direction is described by the wave function

$$\mathbf{E}^{(i)}(z,\omega) = \begin{pmatrix} E_l^{(i)} \\ E_r^{(i)} \end{pmatrix} e^{ikz}. \tag{2.20}$$

The scattered field in the far-field zone can be written as

$$\mathbf{E}^{(s)}(\mathbf{r},\omega) = \frac{\exp\left(ik(r-z)\right)}{-ikr}\mathbf{S}\cdot\mathbf{E}^{(i)}(z,\omega) \tag{2.21}$$

where

$$\mathbf{S} = \begin{pmatrix} S_2 & S_3 \\ S_4 & S_1 \end{pmatrix} \tag{2.22}$$

is the *scattering amplitude matrix* and S_i (i = 1, 2, 3, 4) are four complex amplitude functions. It is worth noting that the scattering amplitude matrix $\mathbf{S} = \mathbf{S}(k,\hat{\mathbf{r}})$ is a function of the wave number k and the scattering direction $\hat{\mathbf{r}} = \mathbf{r}/r$. We then compute the Stokes vector for the scattered field by substituting Eq. (2.21) into Eq. (2.6 – 2.9). The result reads

$$\mathbf{I}^{(s)} = \frac{1}{k^2r^2}\mathbf{M}\cdot\mathbf{I}^{(i)}, \tag{2.23}$$

where the 4×4 matrix $\mathbf{M}$ is called *Mueller matrix* that connects the incident Stokes vector and the scattered Stokes vector. All 16 Mueller matrix elements $\mathbf{M}_{ij}$ can be obtained explicitly in terms of the scattering amplitude matrix $\mathbf{S}$ [34]:

$$\mathbf{M}_{11} = \left(|S_1|^2 + |S_2|^2 + |S_3|^2 + |S_4|^2\right)/2, \tag{2.24}$$

$$\mathbf{M}_{12} = \left(|S_2|^2 - |S_1|^2 + |S_4|^2 - |S_3|^2\right)/2, \tag{2.25}$$

$$\mathbf{M}_{13} = \mathrm{Re}\left(S_2 S_3^* + S_1 S_4^*\right), \tag{2.26}$$

$$\mathbf{M}_{14} = \mathrm{Im}\left(S_2 S_3^* - S_1 S_4^*\right), \tag{2.27}$$

$$\mathbf{M}_{21} = \left(|S_2|^2 - |S_1|^2 + |S_3|^2 - |S_4|^2\right)/2, \tag{2.28}$$

$$\mathbf{M}_{22} = \left(|S_1|^2 + |S_2|^2 - |S_3|^2 - |S_4|^2\right)/2, \tag{2.29}$$

$$\mathbf{M}_{23} = \mathrm{Re}\left(S_2 S_3^* - S_1 S_4^*\right), \tag{2.30}$$

$$\mathbf{M}_{24} = \mathrm{Im}\left(S_2 S_3^* + S_1 S_4^*\right), \tag{2.31}$$

$$\mathbf{M}_{31} = \mathrm{Re}\left(S_2 S_4^* + S_1 S_3^*\right), \tag{2.32}$$

$$\mathbf{M}_{32} = \mathrm{Re}\left(S_2 S_4^* - S_1 S_3^*\right), \tag{2.33}$$

$$\mathbf{M}_{33} = \mathrm{Re}\left(S_1 S_2^* + S_3 S_4^*\right), \tag{2.34}$$

$$\mathbf{M}_{34} = \mathrm{Im}\left(S_2 S_1^* + S_4 S_3^*\right), \tag{2.35}$$

$$\mathbf{M}_{41} = \mathrm{Im}\left(S_4 S_2^* + S_1 S_3^*\right), \tag{2.36}$$

$$\mathbf{M}_{42} = \mathrm{Im}\left(S_4 S_2^* - S_1 S_3^*\right), \tag{2.37}$$

$$\mathbf{M}_{43} = \mathrm{Im}\left(S_1 S_2^* - S_3 S_4^*\right), \tag{2.38}$$

$$\mathbf{M}_{44} = \mathrm{Re}\left(S_1 S_2^* - S_3 S_4^*\right). \tag{2.39}$$

Since every light beam can be represented by a Stokes vector, and the Mueller matrix is the one that transforms the incident Stokes vector to the scattered Stokes vector, the Mueller matrix fully characterizes the optical properties of a particle for the elastic scattering.

2.4 Properties of Mueller Matrices

In the previous section, the scattered field is assumed to be a spherical wave, which is not aways true. When the incident field passes through a polarizer or retarder, the scattered field will remain a plane wave. Therefore, the most general formula for electric field transformation becomes

$$\mathbf{E}' = \mathbf{J} \cdot \mathbf{E}, \tag{2.40}$$

where $\mathbf{J}$ is usually called the *Jones matrix*. Consequently, the Stokes vector transformation can be written as

$$\mathbf{I}' = \mathbf{M} \cdot \mathbf{I}, \tag{2.41}$$

where the Mueller matrix $\mathbf{M}$ is defined by matrix J. It can be shown that the Mueller matrix $\mathbf{M}$ is related to the Jones matrix $\mathbf{J}$ by the following transformation [35]

$$\mathbf{M} = \mathbf{U} \left(\mathbf{J} \otimes \mathbf{J}^* \right) \mathbf{U}^{-1}, \tag{2.42}$$

where "$\otimes$" denotes the outer product of marices and the matrix $\mathbf{U}$ is given by

$$\mathbf{U} = \frac{1}{\sqrt{2}} \begin{pmatrix} 1 & 0 & 0 & 1 \\ 1 & 0 & 0 & -1 \\ 0 & 1 & 1 & 0 \\ 0 & i & -i & 0 \end{pmatrix} = \left(\mathbf{U}^{-1} \right)^{\dagger}. \tag{2.43}$$

The electric field transformation equation Eq. (2.40) implies that both the incident field and the scattered field are completely polarized, and for the most general cases this kind of equation does not exist. However, the transformation of Stokes vector in Eq. (2.41) is always well defined. Thus, there are two kinds of Mueller matrices: those can be derived

from a Jones and those can not. Anderson and Barakat proved [35] that the sufficient and necessary condition for a Mueller matrix $\mathbf{M}$ to be derivable from a Jones matrix is the matrix $\mathbf{F} = \mathbf{U}^{-1}\mathbf{M}\mathbf{U}$ can be factorized in the form

$$\mathbf{F} = \mathbf{J} \otimes \mathbf{J}^*, \tag{2.44}$$

where $\mathbf{J}$ is a 4×4 matrix. Since there are 7 independent elements (plus one irrelevant common phase factor) in the Jones matrix , there should exist 9 equalities between the 16 Mueller matrix elements [36]. One of the most interesting equalities is listed below [37, 38]

$$\mathrm{Tr}\left(\mathbf{M}\mathbf{M}^T\right) = \sum_{i,j=1}^{4} \mathbf{M}_{ij}^2 = 4\mathbf{M}_{11}^2. \tag{2.45}$$

For the Mueller matrices that are not related to Jones matrices, all 16 Mueller matrix elements are independent. However, due to the requirement that every realistic Stokes vector must satisfy Eq. (2.10) and (2.11), the physically admissible Mueller matrices have one constraint: for every Stokes $\mathbf{I}$ satisfying Eq. (2.10) and (2.11), the transformed Stokes vector $\mathbf{I}' = \mathbf{M} \cdot \mathbf{I}$ also satisfies Eq. (2.10) and (2.11) [35]. This leads to a series of inequalities satisfied by the Mueller matrix elements. Two of the most useful ones are [39]

$$\sum_{i,j=1}^{4} \mathbf{M}_{ij}^2 \leq 4\mathbf{M}_{11}^2, \tag{2.46}$$

$$|\mathbf{M}_{ij}| \leq \mathbf{M}_{11}. \tag{2.47}$$

These two inequalities can be used as criteria to test the correctness of experimental measurements and numerical simulations.

2.5 Mirror Symmetry and Chirality

In this section, we survey the effects of chirality on light scattering which is the topic of Chapter 4. Suppose the scattering amplitude matrix of a particle is $\mathbf{S}$, which means the transformation of electric field goes as

$$\begin{pmatrix} E_l' \\ E_r' \end{pmatrix} = \begin{pmatrix} S_2 & S_3 \\ S_4 & S_1 \end{pmatrix} \begin{pmatrix} E_l \\ E_r \end{pmatrix}. \tag{2.48}$$

Now consider a particle that is the mirror image of the aforementioned particle with respect to the scattering plane. It is easy to see it is basically the same scattering problem except that the perpendicular coordinate basis changes sign:

$$\hat{\mathbf{r}} \to -\hat{\mathbf{r}}, \tag{2.49}$$

which implies that $E_r \to -E_r$. To make Eq. (2.48) invariant under such manipulation, we obtain

$$\begin{pmatrix} E_l' \\ -E_r' \end{pmatrix} = \begin{pmatrix} S_2 & -S_3 \\ -S_4 & S_1 \end{pmatrix} \begin{pmatrix} E_l \\ -E_r \end{pmatrix}. \tag{2.50}$$

Thus the scattering amplitude matrix of the mirror particle is given by [31]

$$\mathbf{S}' = \begin{pmatrix} S_2 & -S_3 \\ -S_4 & S_1 \end{pmatrix}. \tag{2.51}$$

According to Eq. (2.24 – 2.39), the Mueller matrix for the mirror particle becomes

$$\begin{pmatrix} \mathbf{M}_{11} & \mathbf{M}_{12} & \mathbf{M}_{13} & \mathbf{M}_{14} \\ \mathbf{M}_{12} & \mathbf{M}_{22} & \mathbf{M}_{23} & \mathbf{M}_{24} \\ -\mathbf{M}_{13} & -\mathbf{M}_{23} & \mathbf{M}_{33} & \mathbf{M}_{34} \\ \mathbf{M}_{14} & \mathbf{M}_{24} & -\mathbf{M}_{34} & \mathbf{M}_{44} \end{pmatrix}, \tag{2.52}$$

where $\mathbf{M}_{ij}$ are the Mueller matrix elements of the original particle. We now consider a collection of particles and their mirror particles. If the numbers of particles and mirror particles are equal, then the off-diagonal Mueller matrix elements will cancel out. This yields the Mueller matrix for the whole system

$$\begin{pmatrix} \mathbf{M}_{11} & \mathbf{M}_{12} & 0 & 0 \\ \mathbf{M}_{21} & \mathbf{M}_{22} & 0 & 0 \\ 0 & 0 & \mathbf{M}_{33} & \mathbf{M}_{34} \\ 0 & 0 & \mathbf{M}_{43} & \mathbf{M}_{44} \end{pmatrix}. \tag{2.53}$$

If we also assume that the particles are orientation averaged, the above Mueller matrix can further simplified to

$$\begin{pmatrix} \mathbf{M}_{11} & \mathbf{M}_{12} & 0 & 0 \\ \mathbf{M}_{12} & \mathbf{M}_{22} & 0 & 0 \\ 0 & 0 & \mathbf{M}_{33} & \mathbf{M}_{34} \\ 0 & 0 & -\mathbf{M}_{34} & \mathbf{M}_{44} \end{pmatrix}. \tag{2.54}$$

We now apply the theory to a collection of randomly oriented particles with handedness. Since the mirror image of a left-handed particle is a right-handed, the Mueller matrix will have off-diagonal elements unless the system has equal amounts of both handed particles. Thus, the off-diagonal Mueller elements become a measure of chirality of a system.

Particularly, $\mathbf{M}_{14}/\mathbf{M}_{11}$ is closely related to the experimentally measurable quantity: the so called circular intensity differential scattering (CIDS) [15], which measures the ability to scatter left and right circularly polarized light differently. This can be demonstrated by considering a randomly oriented particle or a collection of particles represented by the following Mueller matrix

$$\begin{pmatrix} \mathbf{M}_{11} & \mathbf{M}_{12} & \mathbf{M}_{13} & \mathbf{M}_{14} \\ \mathbf{M}_{12} & \mathbf{M}_{22} & \mathbf{M}_{23} & \mathbf{M}_{24} \\ -\mathbf{M}_{13} & -\mathbf{M}_{23} & \mathbf{M}_{33} & \mathbf{M}_{34} \\ \mathbf{M}_{14} & \mathbf{M}_{24} & -\mathbf{M}_{34} & \mathbf{M}_{44} \end{pmatrix}. \tag{2.55}$$

The particle is then illuminated by both right and left circularly polarized light beams of the same intensity. The Stokes vectors of those two beams are given by

$$\begin{pmatrix} 1 \\ 0 \\ 0 \\ 1 \end{pmatrix}, \quad \begin{pmatrix} 1 \\ 0 \\ 0 \\ -1 \end{pmatrix}, \tag{2.56}$$

respectively. Then the measured intensities I_R and I_L for those two cases are given below

$$I_R = \mathbf{M}_{11} + \mathbf{M}_{14}, \tag{2.57}$$

$$I_L = \mathbf{M}_{11} - \mathbf{M}_{14}. \tag{2.58}$$

From Eq. (2.57) and (2.58) one can easily derive that

$$\frac{\mathbf{M}_{14}}{\mathbf{M}_{11}} = \frac{I_R - I_L}{I_R + I_L}. \tag{2.59}$$

The above equation indicates that the chirality of a particle is directly related to how different it scatters right and left circularly polarized light.

3. NUMERICAL METHODS

As we discussed in the previous chapter, the Mueller matrix captures the optical properties of a particle for the elastic scattering of electromagnetic beams. For the single scattering problem, the Mueller matrix is usually derived from the scattering amplitude matrix, which can be computed by solving the Maxwell equations. There are several effective methods available to achieve this, analytically or numerically, depending on the size and composition of the particle. In Chapter 4, the Discrete Dipole Approximation (DDA) method will be used to study the complex structure of the dinoflagelate nucleus. In Chapters 5 and 6, most of particles investigated are homogenous spheres and the Lorenz-Mie theory will be applied. In Chapter 5, the DDA method is also modified to include partially coherent light beams. Here we give a brief survey of the numerical methods that will be used in this dissertation.

3.1 Lorenz-Mie Theory

An analytical solution is available for the problem of light scattering by a homogenous dielectric sphere of arbitrary size and refractive index. Due to the highly symmetric shape of a sphere, the Maxwell equations can be solved exactly using the spherical coordinates. Given the particle size, the refractive index of the sphere and the wavelength of the incident light, the electromagnetic field at every location in space can be obtained. In this section, the basic mathematics of the Lorenz-Mie theory will be provided [34].

It can be shown that in a homogenous medium, the time harmonic Maxwell equations are reduced to two Helmholtz equations

$$\nabla^2\mathbf{E} + k^2\mathbf{E} = 0, \quad \nabla^2\mathbf{H} + k^2\mathbf{H} = 0, \tag{3.1}$$

where k is the wavenumber in that medium. The solutions of the above equations can be written in terms of the so-called *vector harmonic s* $\mathbf{M}$ and $\mathbf{N}$, which can be constructed from a scalar function ψ:

$$\mathbf{M} = \nabla \times (\mathbf{r}\psi), \tag{3.2}$$

$$\mathbf{N} = \frac{1}{k}\nabla \times \mathbf{M}. \tag{3.3}$$

Here the scalar function ψ also satisfies the Helmholtz equation

$$\nabla^2\psi + k^2\psi = 0. \tag{3.4}$$

The above equation can be solved in spherical coordinates through separation of varaibles:

$$\psi_{ml}(r, \theta, \phi) = e^{im\phi} P_l^m(\cos\theta)\, z_l(kr), \tag{3.5}$$

where P_l^m is the associated Legendre function and z_l is any spherical Bessel function. For each ψ_{ml}, there is a pair of vector harmonics

$$\mathbf{M}_{ml} = \nabla \times (\mathbf{r}\psi_{ml}), \tag{3.6}$$

$$\mathbf{N}_{ml} = \frac{1}{k}\nabla \times \mathbf{M}_{ml}. \tag{3.7}$$

Then the electric field can be expressed as a series in terms of $\mathbf{M}_{ml}$ and $\mathbf{N}_{ml}$

$$\mathbf{E} = \sum_{l=1}^{\infty} \sum_{m=-l}^{l} \left(a_{ml}\mathbf{M}_{ml} + b_{ml}\mathbf{N}_{ml}\right). \tag{3.8}$$

Now consider a linearly polarized incident field $\mathbf{E}^{\text{inc}} = e^{ikz}\hat{\mathbf{x}}$, where $\hat{\mathbf{x}}$ is a unit vector in

the $+x$ direction. The incident field can be written in terms of vector hormonics:

$$\mathbf{E}^{(\text{inc})} = \sum_{l=1}^{\infty} \sum_{m=-l}^{l} \left(a_{ml}^{(\text{inc})} \mathbf{M}_{ml}^{(1)} + b_{ml}^{(\text{inc})} \mathbf{N}_{ml}^{(1)} \right), \tag{3.9}$$

where the superscript "(1)" means that the above vector harmonics are derived from spherical Bessel function of the first kind j_l. It can shown that only $m = \pm 1$ componets exist for above expansion and the exact values of the coefficients $a_{ml}^{(\text{inc})}$ and $b_{ml}^{(\text{inc})}$ can be found in [34].

When the aforementioned plane wave is scattered by a sphere of radius a and refractive index m, the electric field inside the sphere $\mathbf{E}^{(i)}$ and scattered field outside the sphere $\mathbf{E}^{(s)}$ can be expressed in a similar manner

$$\mathbf{E}^{(i)} = \sum_{l=1}^{\infty} \sum_{m=-l}^{l} \left(a_{ml}^{(i)} \mathbf{M}_{ml}^{(1)} + b_{ml}^{(i)} \mathbf{N}_{ml}^{(1)} \right), \tag{3.10}$$

$$\mathbf{E}^{(s)} = \sum_{l=1}^{\infty} \sum_{m=-l}^{l} \left(a_{ml}^{(s)} \mathbf{M}_{ml}^{(3)} + b_{ml}^{(s)} \mathbf{N}_{ml}^{(3)} \right), \tag{3.11}$$

where the superscript "(3)" denotes that the vector harmonics are derived from spherical Bessel function of the third kind $h_l^{(1)}$. The corresponding magnetic field in each region can be computed from the equation

$$\mathbf{H} = \frac{c}{ik} \nabla \times \mathbf{E}. \tag{3.12}$$

Given the boundary condition that the tangential components of $\mathbf{E}$ and $\mathbf{H}$ must be continuous across the boundary, the expansions coefficients $\mathbf{A}_{ml}^{(i)}$, $b_{ml}^{(i)}$, $\mathbf{A}_{ml}^{(s)}$ and $b_{ml}^{(s)}$ can be solved from the following equations

$$\left(E_\theta^{(\text{inc})} + E_\theta^{(s)} \right) \Big|_{r=a} = E_\theta^{(i)} \Big|_{r=a}, \quad \left(E_\phi^{(\text{inc})} + E_\phi^{(s)} \right) \Big|_{r=a} = E_\phi^{(i)} \Big|_{r=a}, \tag{3.13}$$

$$\left(H_\theta^{(\text{inc})} + H_\theta^{(s)} \right) \Big|_{r=a} = H_\theta^{(i)} \Big|_{r=a}, \quad \left(H_\phi^{(\text{inc})} + H_\phi^{(s)} \right) \Big|_{r=a} = H_\phi^{(i)} \Big|_{r=a}, \tag{3.14}$$

where we used the fact that in spherical coordinates $\mathbf{E} = (E_r, E_\theta, E_\phi)$ and $\mathbf{H} = (H_r, H_\theta, H_\phi)$. With the internal field and scattered field known, we can write down the electric field in the whole space

$$\mathbf{E}^{(1)} = \mathbf{E}^{(i)}, \quad r \leq a, \tag{3.15}$$

$$\mathbf{E}^{(2)} = \mathbf{E}^{(\text{inc})} + \mathbf{E}^{(s)}, \quad r > a. \tag{3.16}$$

It should be noted that all vectors computations so far are done in spherical coordinates. As will be shown in Chapter (6), the hologram is more convenient to calculate in Cartesian coordinates. This can be converted through a transformation

$$\begin{pmatrix} E_x \\ E_y \\ E_z \end{pmatrix} = \begin{pmatrix} \sin\theta\cos\phi & \cos\theta\cos\phi & -\sin\phi \\ \sin\theta\sin\phi & \cos\theta\sin\phi & \cos\phi \\ \cos\theta & -\sin\theta & 0 \end{pmatrix} \begin{pmatrix} E_r \\ E_\theta \\ E_\phi \end{pmatrix}. \tag{3.17}$$

Although we are able to get the exact field at any location, in most cases only the scattered field in the far-field zone will be relevant. Using the assumption $kr \gg 1$ and asymptotic expression of $h_l^{(1)}$, scattering amplitude matrix can be obtained [34]

$$\mathbf{S}(\theta) = \begin{pmatrix} S_2(\theta) & 0 \\ 0 & S_1(\theta) \end{pmatrix}, \tag{3.18}$$

where

$$S_1(\theta) = \sum_n \frac{2n+1}{n(n+1)} \left(a_n \pi_n + b_n \tau_n\right), \tag{3.19}$$

$$S_2(\theta) = \sum_n \frac{2n+1}{n(n+1)} \left(a_n \tau_n + b_n \pi_n\right). \tag{3.20}$$

The definition of a_n, b_n, π_n and τ_n can be found in [31]. The Mueller matrix then follows

$$\mathbf{M} = \begin{pmatrix} \frac{1}{2}\left(|S_2|^2 + |S_1|^2\right) & \frac{1}{2}\left(|S_2|^2 - |S_1|^2\right) & 0 & 0 \\ \frac{1}{2}\left(|S_2|^2 - |S_1|^2\right) & \frac{1}{2}\left(|S_2|^2 + |S_1|^2\right) & 0 & 0 \\ 0 & 0 & \frac{1}{2}\left(S_2^* S_1 + S_1^* S_2\right) & \frac{i}{2}\left(S_2^* S_1 - S_1^* S_2\right) \\ 0 & 0 & -\frac{i}{2}\left(S_2^* S_1 - S_1^* S_2\right) & \frac{1}{2}\left(S_2^* S_1 + S_1^* S_2\right) \end{pmatrix} \tag{3.21}$$

For numerical evaluation, we chose the Mie code based on the IDL code used by Grier *et al.* [3].

3.2 Discrete Dipole Approximation Method

The Lorenz-Mie theory is obviously limited to homogenous spheres. For particles of arbitrary shapes and dielectric functions, alternative techniques are demanded and the discrete dipole approximation (DDA) is a suitable choice that meets such requirements. Inspired by the observation that the dielectric properties of a macroscopic particle originate from the polarizability of each atom, Purcell and Pennypacker [40] proposed the numerical method by approximating the particle with a collection of polarizable dipoles. Each dipole not only responds to the incident light, but also interacts with other dipoles through dipole-dipole coupling. This method was then improved and refined by Draine *et al.* [22], and Yurkin *et al.* [23]. Here we briefly review the fundamentals of the DDA methods.

Suppose a particle is represented by N dipoles on a cubic lattice with spacing d, and the location of each dipole is denoted by $\mathbf{r}_j$ $(j = 1, ..., N)$. The polarizability α_j of dipole at location $\mathbf{r}_j$ is connected with the dielectric function of the particle through the Clausius-Mossotti relation

$$\alpha_j = \frac{3d^3}{4\pi}\frac{\epsilon_j - 1}{\epsilon_j + 2}. \tag{3.22}$$

The electric field $\mathbf{E}_j$ at location $\mathbf{r}_j$ is contributed both by the incident wave $\mathbf{E}_j^{(\text{inc})} =$

$\mathbf{E}_0 \exp(i\mathbf{k}\cdot\mathbf{r}_j)$, and the radiations from other dipoles with dipole moments $\mathbf{P}_k$ ($k \neq j$), which in turn are induced by the local electric field $\mathbf{E}_k$. Therefore, we have the following self-consistent equations [22]:

$$\mathbf{E}_j = \mathbf{E}_j^{(\text{inc})} - \sum_{k\neq j} \mathbf{A}_{jk}\cdot\mathbf{P}_k, \tag{3.23}$$

$$\mathbf{P}_j = \alpha_j \mathbf{E}_j. \tag{3.24}$$

Here $\mathbf{A}_{jk}$ is a 3×3 matrix defined by [22]

$$\mathbf{A}_{jk} = \frac{\exp(ikr_{jk})}{r_{jk}}\left[k^2(\hat{\mathbf{r}}_{jk}\hat{\mathbf{r}}_{jk} - \mathbf{1}_3) + \frac{ikr_{jk}-1}{r_{jk}^2}(3\hat{\mathbf{r}}_{jk}\hat{\mathbf{r}}_{jk} - \mathbf{1}_3)\right], \quad j\neq k, \tag{3.25}$$

where $r_{jk} = |\mathbf{r}_j - \mathbf{r}_k|$, $\hat{\mathbf{r}}_{jk} = (\mathbf{r}_j - \mathbf{r}_k)/r_{jk}$ and $\mathbf{1}_3$ denotes the 3×3 identity matrix.

After eliminating $\mathbf{E}_j$, Eq. (3.23) and (3.24) can be put in a compact form

$$\sum_{k=1}^{N} \mathbf{A}_{jk}\cdot\mathbf{P}_k = \mathbf{E}_j^{(\text{inc})}, \tag{3.26}$$

where $\mathbf{A}_{jj} = \alpha_j^{-1}$ [22]. The polarization $\mathbf{P}_j$ can be obtained by numerically solving the above linear algebraic equation. Once $\mathbf{P}_j$ is known, the scattered field can be written as

$$\mathbf{E}^{(s)}(\mathbf{r}) = \frac{k^2\exp(ikr)}{r}\sum_{j=1}^{N}\exp(-ik\hat{\mathbf{n}}\cdot\mathbf{r}_j)(\hat{\mathbf{n}}\hat{\mathbf{n}} - \mathbf{1}_3)\cdot\mathbf{P}_j, \tag{3.27}$$

where unit vector $\hat{\mathbf{n}} = \mathbf{r}/r$ indicates the scattering direction. By considering two cases of incident fields with orthogonal polarization directions, the scattering amplitude matrix S can be obtained. In Chapter 6, the incident field in Eq. (3.26) will be modified in order to study partially coherent light sources. For numerical simulation, we use the DDSCAT software package developed by Draine *et al.* [22].

4. DETECTION OF DINOFLAGELLATES BY THE LIGHT SCATTERING PROPERTIES OF THE CHIRAL STRUCTURE OF THEIR CHROMOSOMES*

One of the most prominent properties of dinoflagellates is their large sized and highly chromosome-laden nucleus, which contains dozens of cylindrically shaped chromosomes. With such high chromatic concentration, these chromosomes condense into ordered helical structures and were acclaimed to be responsible for the large circular polarization effects observed in the light scattering from dinoflagellates. In previous research, a thin helix model of a chromosome was used to compare the Discrete Dipole Approximation (DDA) and the analytical Born approximation calculations. However, for such a simplified model only modest qualitative agreements with experimental measurements were achieved. Moreover, only one chromosome in one nucleus was simulated, overlooking the effects of interactions between chromosomes. In this work, we adopt the helical plywood liquid crystal model with a capsule shape, in which parallel fibrils lie in planes perpendicular to the helix axis and the orientations of these fibrils twist at a constant angle between two neighboring layers. The ADDA code is applied to calculate the 16 Mueller matrix elements of light scattering from a single chromosome and from the nucleus, which is composed of a collection of randomly positioned and randomly orientated chromosomes. Special attention is paid to the $\mathbf{S}_{14}$ Mueller matrix element, which describes the ability of differentiating left and right circularly polarized light. Our results show that large $\mathbf{S}_{14}$ back scattering signals from the dinoflagellate nucleus results from the underlying helical structures of its chromosomes. These signals are sensitive to the light wavelength and pitch of the chromatic helix, the latter of which is species specific. Therefore, detecting

*This chapter is reprinted from Journal of Quantitative Spectroscopy & Radiative Transfer, **130**, 24-33, 2014, J. P. Liu and G. W. Kattawar, "Detection of dinoflagellates by the light scattering properties of the chiral structure of their chromosomes", Copyright 2014, with permission from Elsevier.

back scatterings $\mathbf{S}_{14}$ signal could be a promising method to monitor dinoflagellates such as *K. brevis*, the causal agent of the Florida red tide.

4.1 Introduction

Algal bloom, particularly harmful algal blooms (HABs), is becoming an increasingly global issue, imposing huge economic and health threats on human beings around the aquatic environments when blooms take place [6, 7, 8]. Notable ones in North America are blooms in the Gulf of Maine and Florida red tide, caused by *Alexandrium fundyense* and *Karenia brevis* (formerly known as *Gymnodinium breve* and *Ptychodiscus brevis*), both of which are dinoflagellates. One of the key features of dinoflagellates is their more ordered chromosomes compared with other genera. Previous transmission electron microscopy (TEM) observations showed bands, arches and crenulation in chromosomes of *Prococentrum micans* and *K. brevis* [4, 5, 1]. It was later confirmed [1, 10] that the chromatic materials inside the nucleus of *P. micans* condensed into ordered helical liquid crystals, a hypothesis proposed by Bouligand in 1968 [9]. Electron microscopy images of dinoflagellate chromosomes in situ showed that the double-stranded DNA modules coil into parallel fibrils pointing perpendicular to the chromosomes main axis and rotate along the main axis. This cholesteric structure was considered to be responsible for the observed large circular polarization effect in the light scattering from dinoflagellates [11, 12]. The circular intensity differentially scattering (CIDS), which describes the ability to differentially scatter left and right circularly polarized light, is encoded in the $\mathbf{S}_{14}$ Mueller matrix element. Due to lack of mirror symmetry with respect to the scattering plane, a non-vanishing $\mathbf{S}_{14}$ signal is expected from light scattering of helical structures [31]. They reported that both dinoflagellates with helically structured chromosomes (*P. micans* and *C. cohnii*) and those without (*G. polyedra*) could produce $\mathbf{S}_{14}$ signals, but those with helical structures produce larger $\mathbf{S}_{14}$ than those without. It was also shown by Shapiro et al. that *C. cohnii*

gives smaller $\mathbf{S}_{14}$ signals when the chromosomes structures were destroyed [12]. All these results led Shapiro et al. to conclude that the helical structures of chromosomes are ultimately responsible for the highest $\mathbf{S}_{14}$ signals, while smaller signals could be attributed to the cylindrically shaped chromosomes in oblique orientations.

Paralleling those experimental explorations were theoretical endeavors carried out by C. Bustamante et.al, who managed to model typical helical structures in biology using a thin helical wire with uniaxial polarizability, and analytically formulated the CIDS (essentially $\mathbf{S}_{14}$ Mueller matrix element) to the first Born approximation [13]. This formalism was then applied to calculate the CIDS of membranes from the bacterium *Spirillum serpens* and qualitative agreement was obtained when compared with experimental measurements using X-rays [14]. Further generalizations of this method include extension to general polarizability, scatterings of randomly orientated biological particles and scatterings of an arbitrary collection of particles with scalar polarizability (or refractive index) [15, 16, 41]. Some conclusions made by Bustamante et.al are worthwhile noting: (1) CIDS or $\mathbf{S}_{14}$ was shown to be more sensitive to the shape and internal chiral structures of scatterers than $\mathbf{S}_{11}$ [13], (2) CIDS could exist for scatterers consisting of a group of particles with a spherically symmetric refractive index [41], (3) CIDS has its largest value when the wavelength matches the pitch (chiral parameter) of the helical structure [41].

Following these works, Singham et al. [17] developed the coupled dipole approximation method to calculate the CIDS from a one dimensional helical crystal modeled by a thin helix. It proved to be a convenient numerical tool to study the CIDS from helical scatterers from both oriented and orientation averaged cases. The results showed that CIDS weakly depends on the length of helix so long as it is much larger than the wavelength, while the thickness of the helix is of significant importance. Since only the $\mathbf{S}_{14}$ Mueller matrix element had been calculated using both the first Born approximation and coupled dipole approximation method, Shapiro et al. [18, 19] complemented previous works by

calculating all 16 Mueller matrix elements utilizing both methods, and good agreement between those two methods was obtained when applied to helices. However, the coupled dipole approximation was confirmed to be more useful when compared with experimental measurements of Muller matrix elements of *Eledone cirrhosa*, even though only a few qualitative features of $\mathbf{S}_{11}$, $\mathbf{S}_{12}$ and $\mathbf{S}_{14}$ were consistent.

To sum up, all previous theoretical studies of biological helical structures used similar thin helix wire models. While it is a simple and abstract model that characterizes the universal chiral structures of microbiological particles, it lacks some specific features that are unique to each case. For instance, the chromosomes of dinoflagellates have rich fibril patterns which appeared in TEM micrographs, and the thicknesses and distances between these fibrils have observable impact on the birefringence of the chromosomes. Therefore, it is understandable that only modest qualitative agreement could be achieved between numerical simulations and experimental measurements. Moreover, usually only one single helix was considered in the calculations, totally obscuring the interactions between two helical structures, which is not sufficient in the case of light scattering from the nucleus of *K. brevis* where dozens of cylindrically shaped chromosomes are packed into one nucleus. Thus we expect a more realistic model could achieve the goal of better quantitative agreements with experiments and making reliable, observable predictions.

4.2 Models and Methods

Here we present our models for both a single cell of a dinoflagellate and its chromosomes based on Bouligands liquid crystal model [9]. The Amsterdam Discrete Dipole Approximation (ADDA) code [23] is used to calculate all 16 Mueller matrix elements.

4.2.1 Model of a Cell

We focus on dinoflagellates *P. micans* and *K. brevis* in the following study because of their ordered chromosome structures and the relevance of *K. brevis* to the infamous Florida

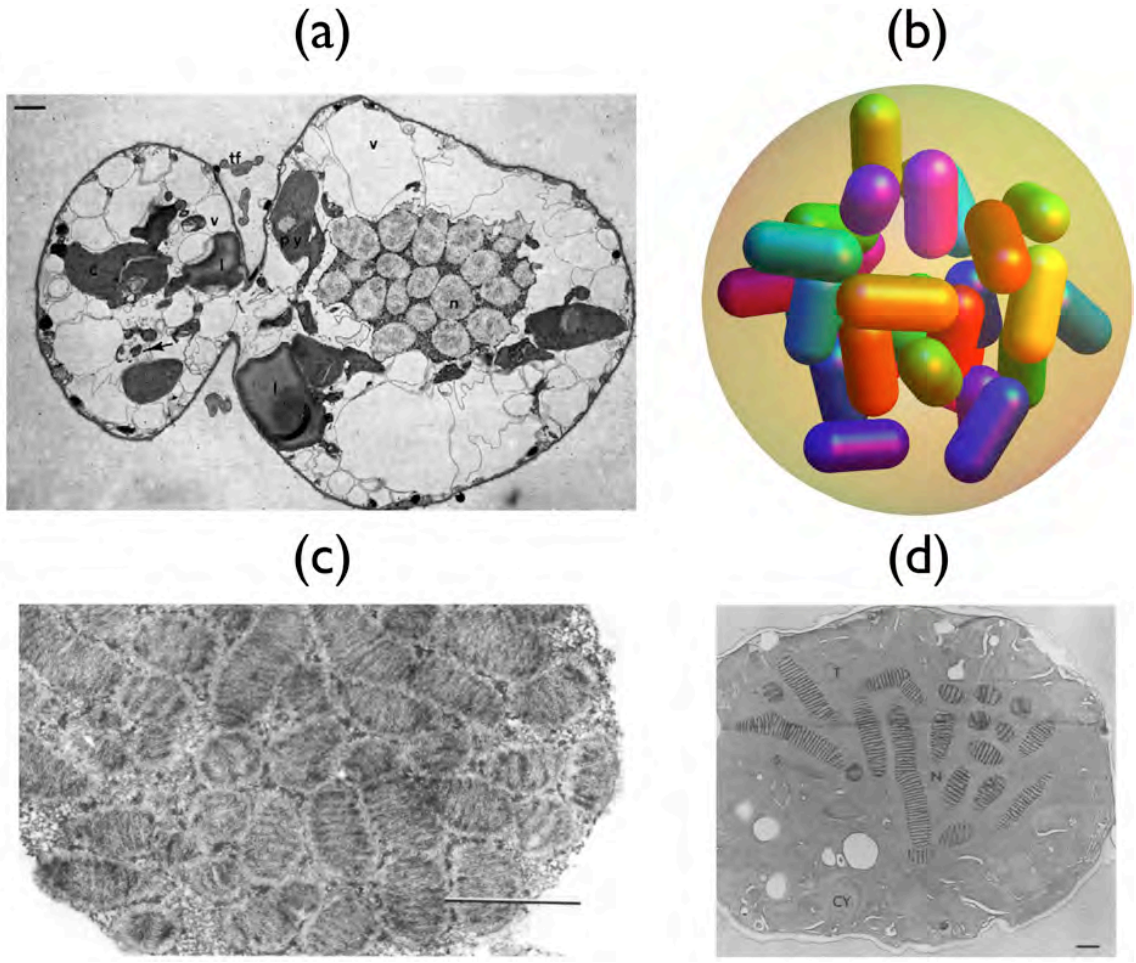

Figure 4.1: (a) Transmission electron microscopy of a longitudinal section of *K. brevis* taken from [4]. The bar is 1 μm. (b) A model of the nucleus, where the chromosomes are modeled by capsules of the same size that are randomly positioned and oriented within a fixed space without touching each other. (c) The TEM image of a separated nucleus of *K. brevis* taken from [5]. The bar here is 1 μm. (d) The TEM image of a nucleus of *P. micans* from [1]. The bar is 1 μm.

red tide. The *K. brevis* has a complex celular structure (Fig. 4.1), which is composed of two regions, epicone (left part of Fig. 4.1. (a)) and hypocone (right part of Fig. 4.1. (a)) connected by the narrow theca ridge, covered by a cell covering (theca) made of four membranes [4]. The diameter of the cell is about 20-40 μm, and the nucleus measures about 6-9 μm, locating at the hypocone [4]. Apart from those, there are also dozens of irregular choloplasts scattered around in both epicone and hypocone. For the time being, we only consider the effect of the nucleus. The reasons for such simplification are: (1) it is difficult to model the whole cell due to the complexity of cellular structure of dinoflagellates, which is beyond our computational power to simulate at the present time, (2) all previous research lead to the conclusion that the nucleus and underlying chromosome structure are the key players in explaining the observed large circular polarization effect. In our simplified model, the nucleus is a collection of randomly positioned and randomly oriented capsules confined in a finite space. We also make sure that no capsules intersect each other when generating the dipoles. The internal helical structure will be discussed in the next subsection of chromosome model (Fig. 4.2. (b)). Due to limitation of computational time and memory available, a smaller nucleus with diameter 4.0 μm and up to 20 chromosomes in one nucleus are used in our calculations (Fig. 4.1. (b)). The parameters of each chromosome are: diameter 0.5 μm (100 dipoles), height 1.0 μm (200 dipoles). Since no direct measurement of the refractive index can be found in literature to our knowledge and our model works for general refractive index, we choose the value $1.2 + 0.01i$ with respect to ocean water without loss of generality. In all calculations below, the light wavelengths are measured in ocean water.

4.2.2 Model of a Chromosome

As was discussed in the introduction section, the chromosomes of *P. micans* have been studied extensively [1, 10], and the well confirmed model is the Bouligands cholesteric

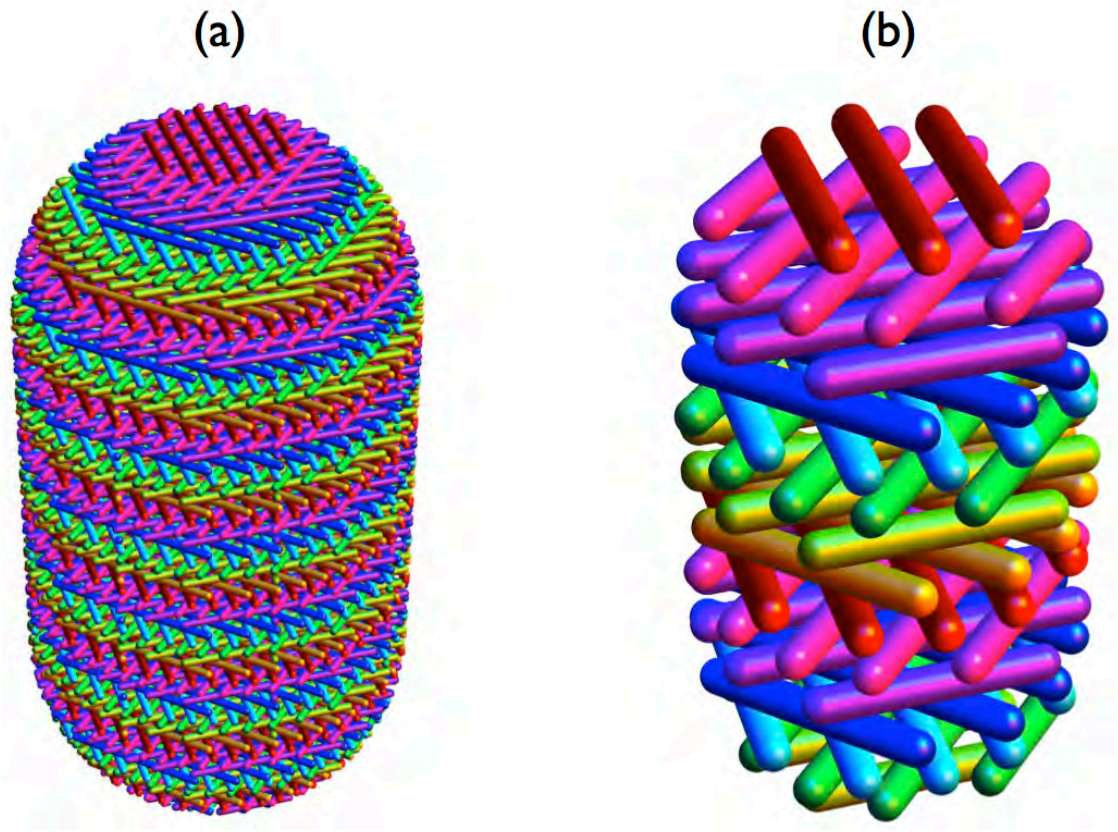

Figure 4.2: (a) The liquid crystal model of dinoflagellate chromosome, where different colors indicate different orientations of fibrils in each layer. The diameter of the chromosome is 1 μm (480 dipoles), and its length is 2 μm (960 dipoles). In each layer, there are up to 20 fibrils, and each fibril has a diameter of 21 nm (10 dipoles). A total of 8 turns are considered and the twist angle we used is 45°. (b) A simplified model of (a), where the color scheme has the same meaning. The parameters are: chromosome diameter and length are 0.5 μm (100 dipoles) and 1 μm (200 dipoles), respectively, up to 5 fibrils in each layer, fibril diameter 50 nm (10 dipoles), twist angle 45° and 2 turns.

liquid crystal model [9]. As shown in Fig. 4.2, the chromosome has ordered helical structure composed of layers perpendicular to the chromosome axis, with thin fibrils lying in parallel in each layer and rotating along the axis. For *P. micans*, the measured diameter of the chromosome is about 1 μm, and the length varies from several μm to 20 μm (Fig. 4.1. (d)). Another key parameter is the pitch of helix, or the length along the axis of the chromosome over which the fibrils finish one periodic rotation. The mean value is about 250 nm, which is almost twice as large as that of *K. brevis* as can be seen in Fig. 4.1. The fibrils are shown to be about several nanometers in diameter, which is so small that these fine structures cannot be detected in usual scatterings of visible or even ultraviolet light. Therefore, only much larger scale structures should be considered. In our model, each fibril has at least 10 dipoles, which is about 21 nm in diameter for a chromosome with diameter 1.0 μm (Fig. 4.2. (a)). With that being settled, the number of layers in one pitch has an upper limit to guarantee that two layers do not touch other. 8 layers are used in our model, which corresponds to 45° of twist angle between two layers. Finally, the length of P.micans chromosome is chosen to be 2 μm, with an aspect ratio of 2 and about 8 turns of helical periodicities in total, a choice that will be justified below (see Fig. 4.4).

The chromosome structure of *K. brevis* could not be found in such detail as that of *P. micans* in the literature, nevertheless the TEM image (Fig. 4.1. (c)) of separated *K. brevis* nucleus clearly shares the same band feature as that of *P. micans* (Fig. 4.1. (d)), which is a strong indication that the liquid crystal model is also applicable to *K. brevis* [9]. Under this assumption, the chromosomes of *K. brevis* could also be described by the model proposed in Fig. 4.2. (a). A factor of 1/2 is multiplied on all extensive parameters such as length and diameters due to the smaller size. Bearing in mind that a total number of 480 $\times$ 480 $\times$ 960 dipoles are used to model a single chromosome, it is almost computationally impossible to model a full sized nucleus with 20 randomly oriented chromosomes inside, which means 20 times more dipoles are required. A compromised solution is a simplified

model with less layers of fibrils, and with larger pitch in order to maintain the same length of chromosome. Therefore, when calculating the scatterings of a collection of chromosomes, the model Fig. 4.2. (b), where fewer numbers of dipoles ($100 \times 100 \times 200$) and fewer numbers of turns of the helix (2) are used to facilitate the simulations of 20 chromosomes at once, will be used. However, one issue follows, i.e. the pitch is altered from the experimental value, which means the model Fig. 4.2. (b) does not serve as a faithful representation of the actual nucleus and one can only expect qualitative predictions.

4.3 Results of Single Chromosome Scattering

4.3.1 Light propagating along the chromosome axis

This case is of special interest because CIDS from a helix was believed to have its largest value when light propagates along the helical axis, a result by Bustamante et al. [13] that will be confirmed in the next subsection. We specifically investigated the wavelength dependence of the normalized $\mathbf{S}_{14}$ Mueller matrix element by varying the wavelength of the scattered light from 200 nm to 500 nm. The results given in Fig. 4.3 show that $\mathbf{S}_{14}$ strongly depends on the wavelength of the incident light, with nearly vanishing values obtained when the wavelength is larger than the pitch, while significant signals appears if the wavelength is about the same order of the pitch. In particular, the largest $\mathbf{S}_{14}$ backscattering appears when the wavelength exactly matches the pitch, in which case it is in the ultraviolet region, a result that is well known [13, 41]. It is worth noting that Mueller matrix elements $\mathbf{S}_{22}$, $\mathbf{S}_{33}$, and $\mathbf{S}_{44}$ show similar behavior as $\mathbf{S}_{14}$, with large backscattering peaks appearing when the wavelength is the same as pitch.

We further considered the situation when the number of turns (or the number of helical periodicities) is changed from 8 to 12 in order to justify our choice of 8 turns of the helix and the aspect ratio. No critical differences were observed between all Muller matrix elements calculated, although the forward scattering intensity increases reasonably as the

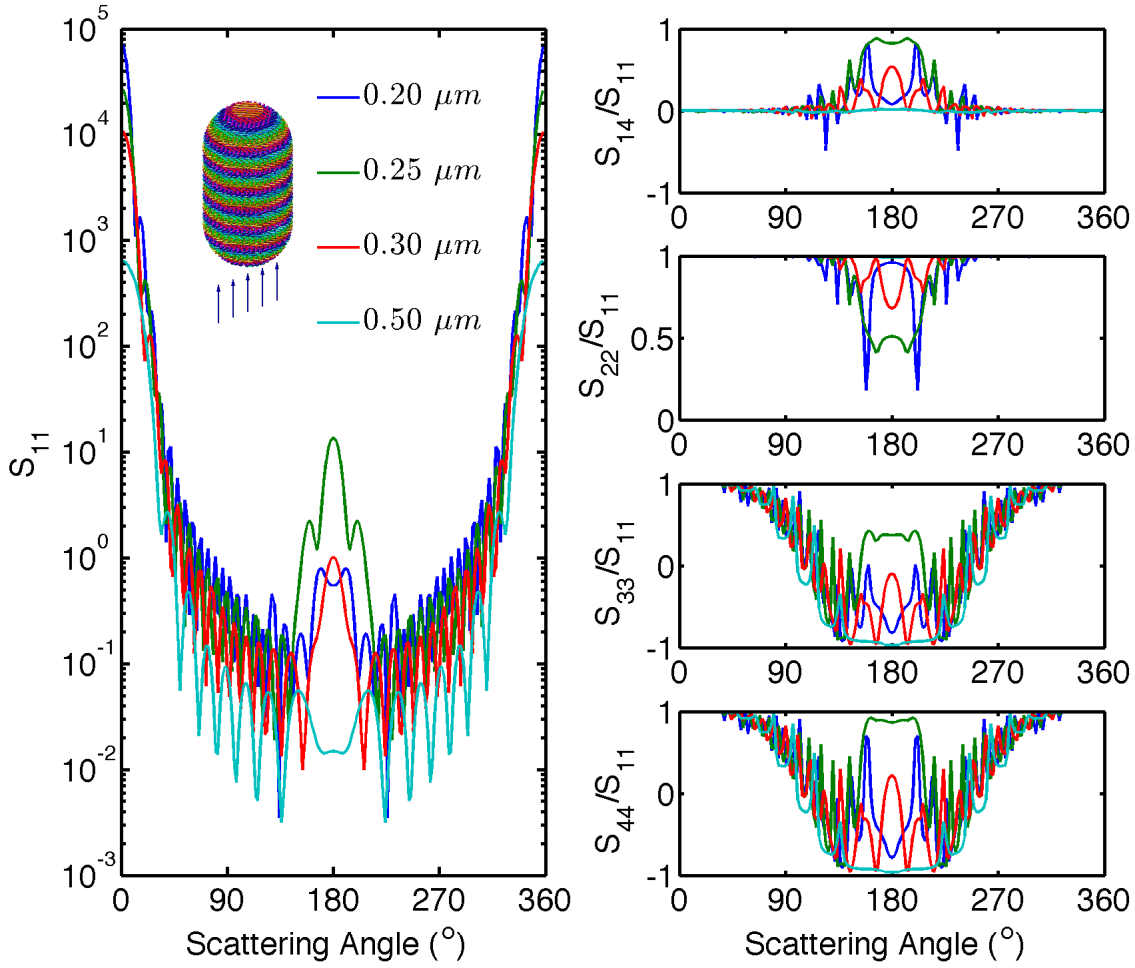

Figure 4.3: The Mueller matrix elements calculated using model (Fig. 4.2. (a)), where the light propagates along the chromosome axis (z-direction). The wavelength takes value from 0.20, 0.25, 0.30, and 0.50 μm. The chromosome has diameter 1.0 μm, length 2.0 μm and pitch 0.25 μm. The refractive index used is $1.2 + 0.01i$, and the scattering plane is yz-plane.

length of the chromosome increases. Therefore, conclusions made from chromosomes of aspect ratio 2 are applicable to larger aspect ratio chromosomes (about 10) that are generally found in real cases.

4.3.2 Light scattering from oriented chromosomes

We also calculated the Mueller matrix from scattering of oriented chromosomes, where the incident light and the axis of the chromosomes form an angle of 0° to 90°. Two wavelengths are considered: 0.25 μm and 0.50 μm. With a pitch of 0.25 μm, the chromosome produces a large backscattering signal only when the light propagates roughly along its axis (when the inclination angle is smaller than 30°) and the wavelength matches its pitch (see Fig. 4.4 and Fig. 4.5). Therefore, it is reasonable to conclude that when large $\mathbf{S}_{14}$ signals show up from scattering from a collection of randomly orientated chromosomes, it is highly plausible that one or two chromosomes are aligned approximately along the direction of the light. With that being said, $\mathbf{S}_{14}$ as large as 0.8 could be evidence of the existence of underlying helical structures, a conjecture subject to further examination in the preceding sections. The result (Fig. 4.5) also indicates weak orientation dependence of backscattering when the incident wavelength is much larger than the pitch.

4.3.3 Light scattering from orientation averaged chromosomes

Another interesting question to ask is whether we can still get strong backscattering $\mathbf{S}_{14}$ signals when the orientation of chromosomes is averaged. In Fig. 4.6 the Mueller matrix elements are calculated for wavelengths from 0.20 μm to 0.50 μm. At a wavelength of 0.25 μm, which is the same as the pitch, we find large backscattering signals from Mueller matrix elements $\mathbf{S}_{14}$, $\mathbf{S}_{41}$, $\mathbf{S}_{22}$, $\mathbf{S}_{33}$, and $\mathbf{S}_{44}$, and the angular dependence of these matrix elements deviate markedly from Rayleigh scattering when the scattering angle is larger than 135°. In particular, $\mathbf{S}_{14}$ can have values as large as 0.70, which is comparable to the largest value obtained when the chromosome is fixed and the light propagates along the

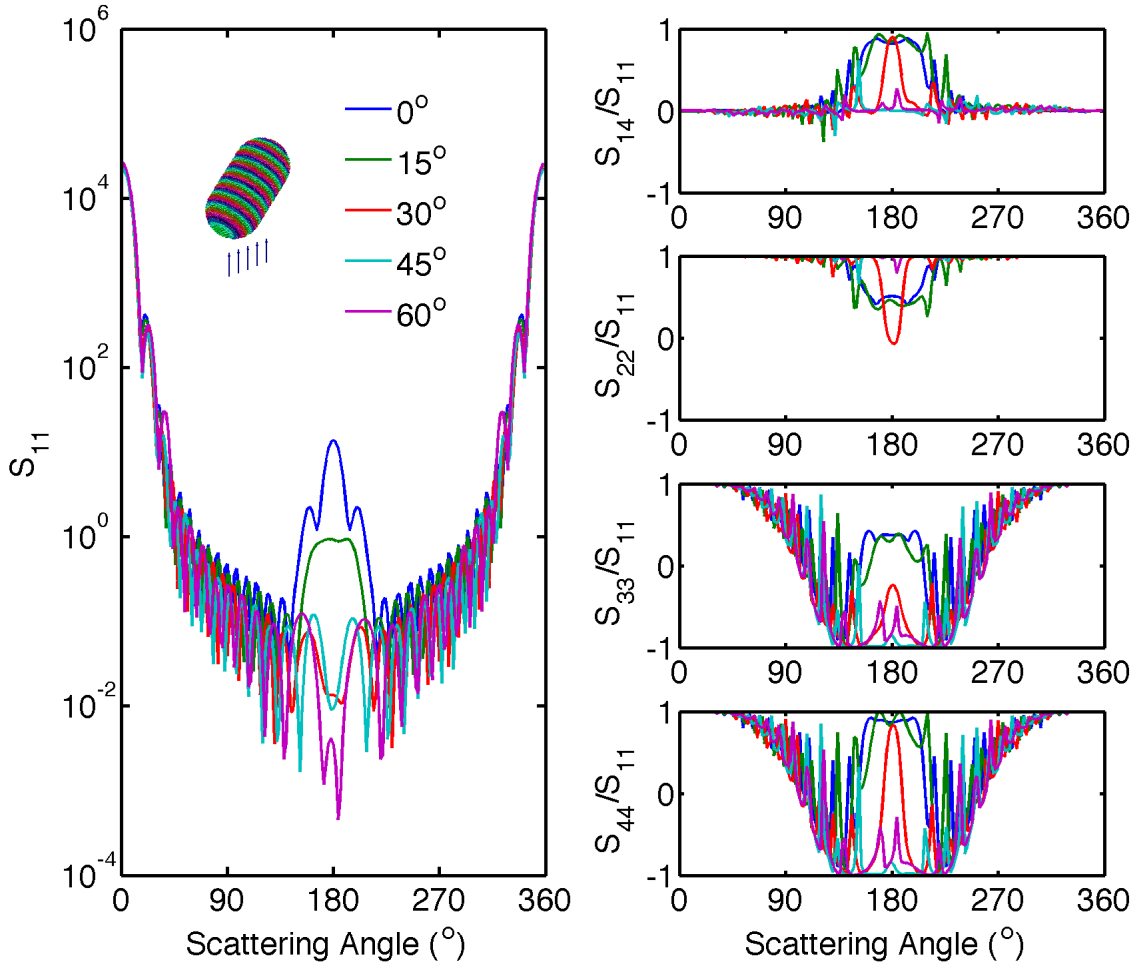

Figure 4.4: The Mueller matrix elements calculated using model (Fig. 4.2. (a)) when the wavelength is 0.25 μm. The orientation of the chromosome is defined by Euler angles α, β and γ, with α and γ fixed to be 0, and β taking values $0°$, $15°$, $30°$, $45°$, and $60°$. The chromosome has diameter 1.0 μm, length 2.0 μm and pitch 0.25 μm. The refractive index used is $1.2 + 0.01i$, and the scattering plane is yz-plane.

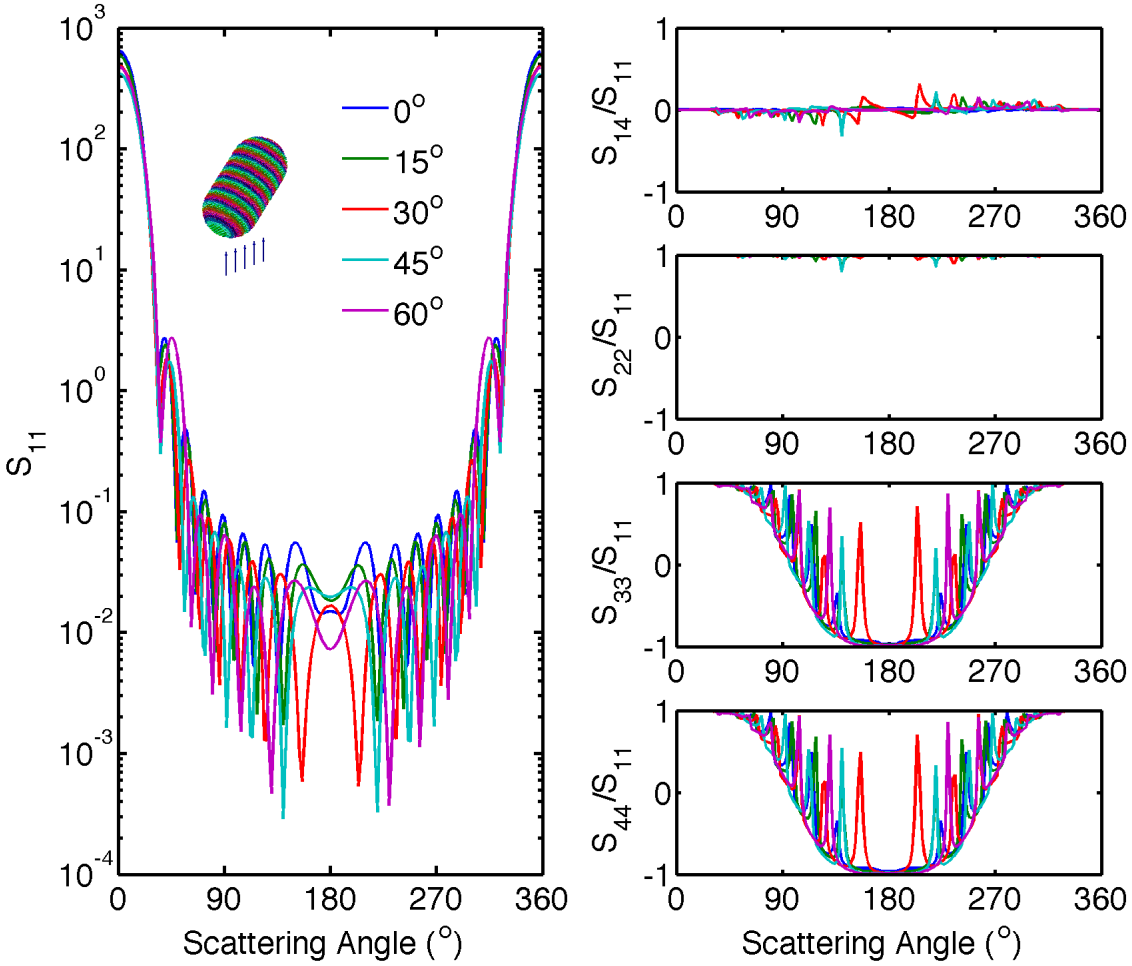

Figure 4.5: Same as Fig. 4.4, except that the wavelength is 0.50 μm.

axis (Fig. 4.3. (a)). This can be explained as follows. The normalized $\mathbf{S}_{14}$ is defined as

$$\mathbf{S}_{14}(\theta) = \frac{\int \mathbf{M}_{14}(\alpha, \beta, \gamma, \theta) d\Omega}{\int \mathbf{M}_{11}(\alpha, \beta, \gamma, \theta) d\Omega}, \tag{4.1}$$

where $\mathbf{M}_{11}$ and $\mathbf{M}_{14}$ are Muller matrix elements before normalization, and α, β, γ are Euler angles. Remember that $\mathbf{M}_{14}$ is non-vanishing only when the scattering angle θ is close to 180°, and that Mueller matrix elements weakly depend on Euler angles α and γ. Let us focus on the case when the scattering angle is 180° and we have

$$\mathbf{S}_{14}(180^\circ) = \frac{\int \mathbf{M}_{14}(\beta, 180^\circ) \sin\beta d\beta}{\int \mathbf{M}_{11}(\beta, 180^\circ) \sin\beta d\beta}. \tag{4.2}$$

Also notice in Fig. 4.4, $\mathbf{M}_{11}$ at small β (less than 15°) is several orders larger than $\mathbf{M}_{11}$ at large β. Thus the denominator can be approximated by $\mathbf{M}_{11}(0, 180^\circ) \sin\beta_0 \Delta\beta$, where β_0 and $\Delta\beta$ are some small angles. The same argument works for the numerator and similar result can be obtained: $\mathbf{M}_{14}(0, 180^\circ) \sin\beta_0 \Delta\beta$. Therefore, we get

$$\mathbf{S}_{14}(180^\circ) \approx \frac{\mathbf{M}_{14}(0, 180^\circ)}{\mathbf{M}_{11}(0, 180^\circ)}, \tag{4.3}$$

where the right hand side is $\mathbf{S}_{14}$ when the chromosome is fixed. This is a rather rough estimation, but it gives some sense why $\mathbf{S}_{14}$ remains so large even after orientation averaging. The implication of this result is that large backscattering $\mathbf{S}_{14}$ (and possibly $\mathbf{S}_{22}$, $\mathbf{S}_{44}$) signals may be detected from a solution of dinoflagellates.

However, as the wavelength approaches 0.50 μm, almost all 16 Mueller matrix elements approach the Rayleigh-Gans limit, with vanishing right upper block matrix elements. This is conceivable because 0.50 μm is much larger than the helical parameter (0.25 μm here), and the chromosome restore the mirror symmetry with respect to the scattering plane at the scale of wavelength, in the sense that the light wave can no longer feel

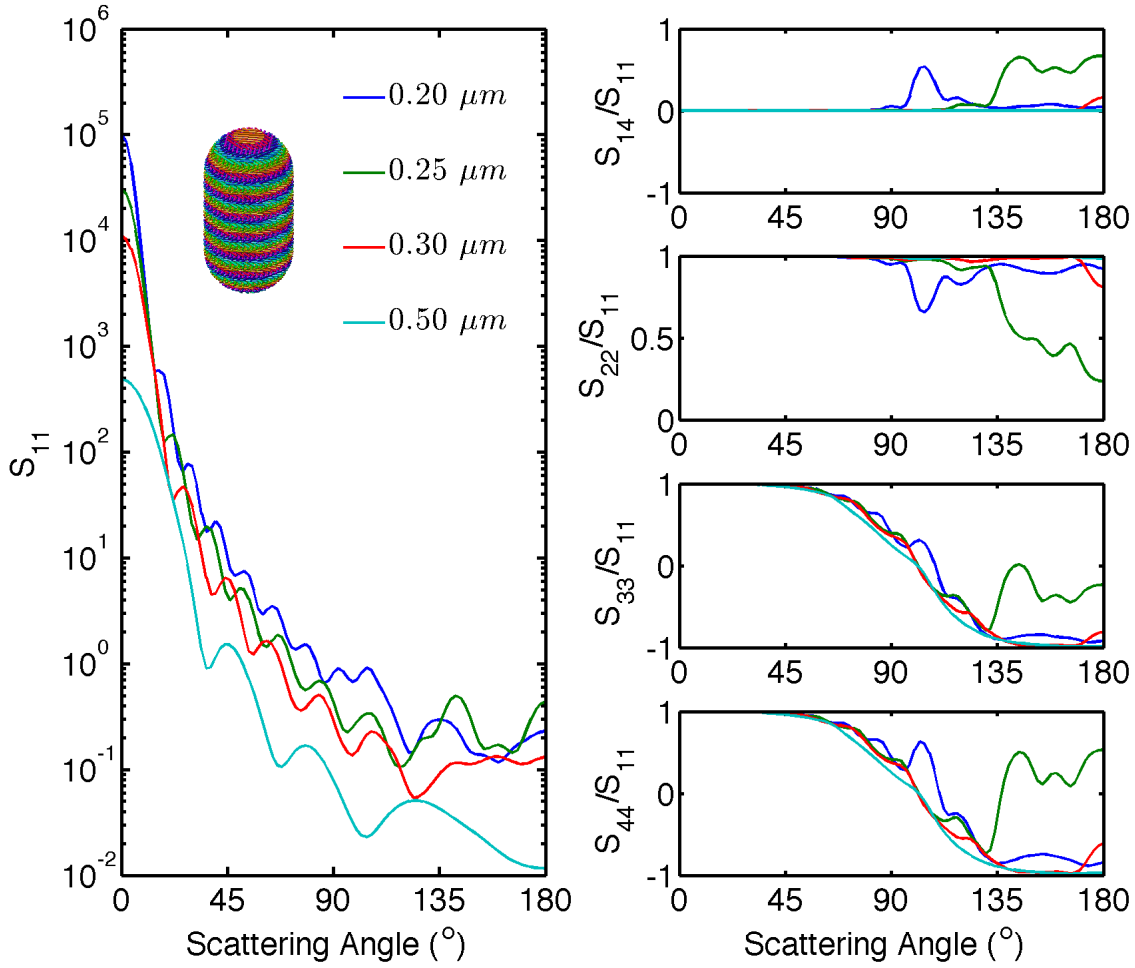

Figure 4.6: Mueller matrix elements from a single chromosome calculated using model (Fig. 4.2. (a)) when the wavelength takes values 0.20 μm, 0.25 μm, 0.30 μm and 0.50 μm, and in all cases the orientation of the chromosomes is averaged. The chromosome has diameter 1.0 μm, length 2.0 μm and pitch 0.25 μm. The refractive index used is $1.2 + 0.01i$.

the influence of the chirality of the chromosome structure.

4.4 Results of Nucleus Scattering

4.4.1 Light Scattering from a Single Immobilized Dinoflagellate

As was discussed in the second section, a simplified chromosome model will be used when attempting to simulate a full sized *K. brevis* nucleus with dozens of chromosomes inside. Even though the result is qualitative, it still gives insight on what to expect from full scale simulations. In Fig. 4.7 and Fig. 4.8, we calculated the Mueller matrix elements from an immobilized nucleus of *K. brevis*. To appreciate how the helical structure of chromosomes affect back scattering, we compare the results of two cases: one with constant twist angle between two layers and the other with random twist angle, which means one has ordered liquid crystal structure while the other does not. Therefore two nuclei share the same shape when looking at the positions and orientations of all 20 chromosomes, while the underlying chromosome structures are totally different. Fig. 4.7 shows that even though the Mueller matrix elements have almost the same forward scattering (or small angle scattering) patterns, which is mainly determined by the size and shape of chromosomes, the back scatterings for two cases differ dramatically, with the random twist case showing negligible $\mathbf{S}_{14}$, $\mathbf{S}_{22}$, $\mathbf{S}_{33}$ and $\mathbf{S}_{44}$ signals around 180° scattering angle, and the constant twist case showing high backward scattering peaks. It is worth noting that $\mathbf{S}_{11}$ is much less sensitive to the internal structure of chromosomes than $\mathbf{S}_{14}$ is. With these results at hand, we can thereby conclude that the largest back scattering $\mathbf{S}_{14}$ signal is contributed by the internal helical structure, while the rest by the shape.

The same calculation was also performed in Fig. 4.8 but with varying wavelength. The chromosomes in our fictional nucleus have pitch 0.5 μm, and the Mueller matrix elements produce prominent backscattering signals when the wavelength is about the same order as the pitch. This result is totally in accordance with previous results of a single chromosome,

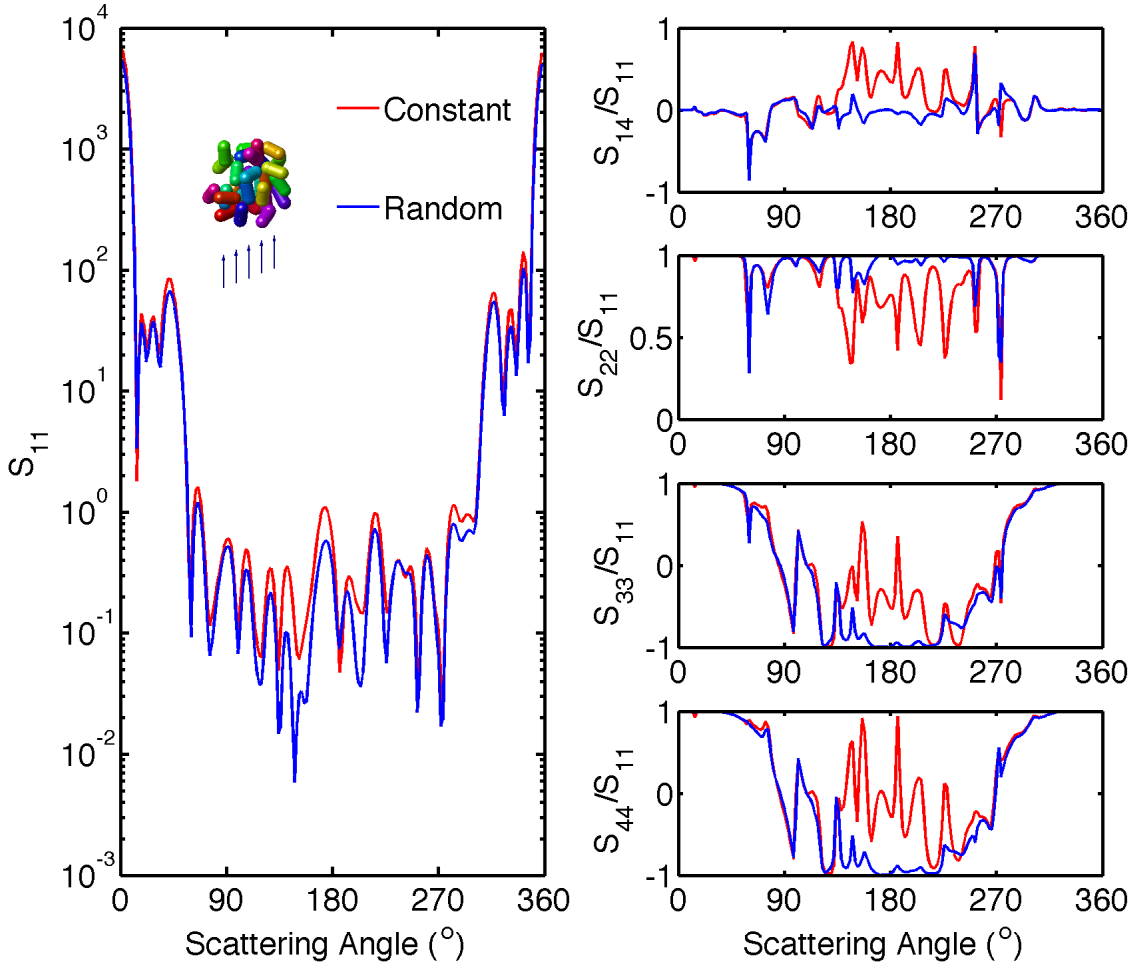

Figure 4.7: Mueller matrix elements from a fixed dinoflagellate calculated using the nucleus model (Fig. 4.1. (b)) and the simplified chromosome model (Fig. 4.2. (b)). The red line is the case when the twist angle is $45°$, while the blue line is the one with random twist angle in each layer. In both cases, the light wavelength is 0.5 μm, which matches the pitch of the helical structure. The nucleus has diameter 4.0 μm. The chromosome has diameter 0.5 μm, length 1.0 μm and pitch 0.5 μm. The refractive index used is $1.2 + 0.01i$ and the scattering plane is yz-plane.

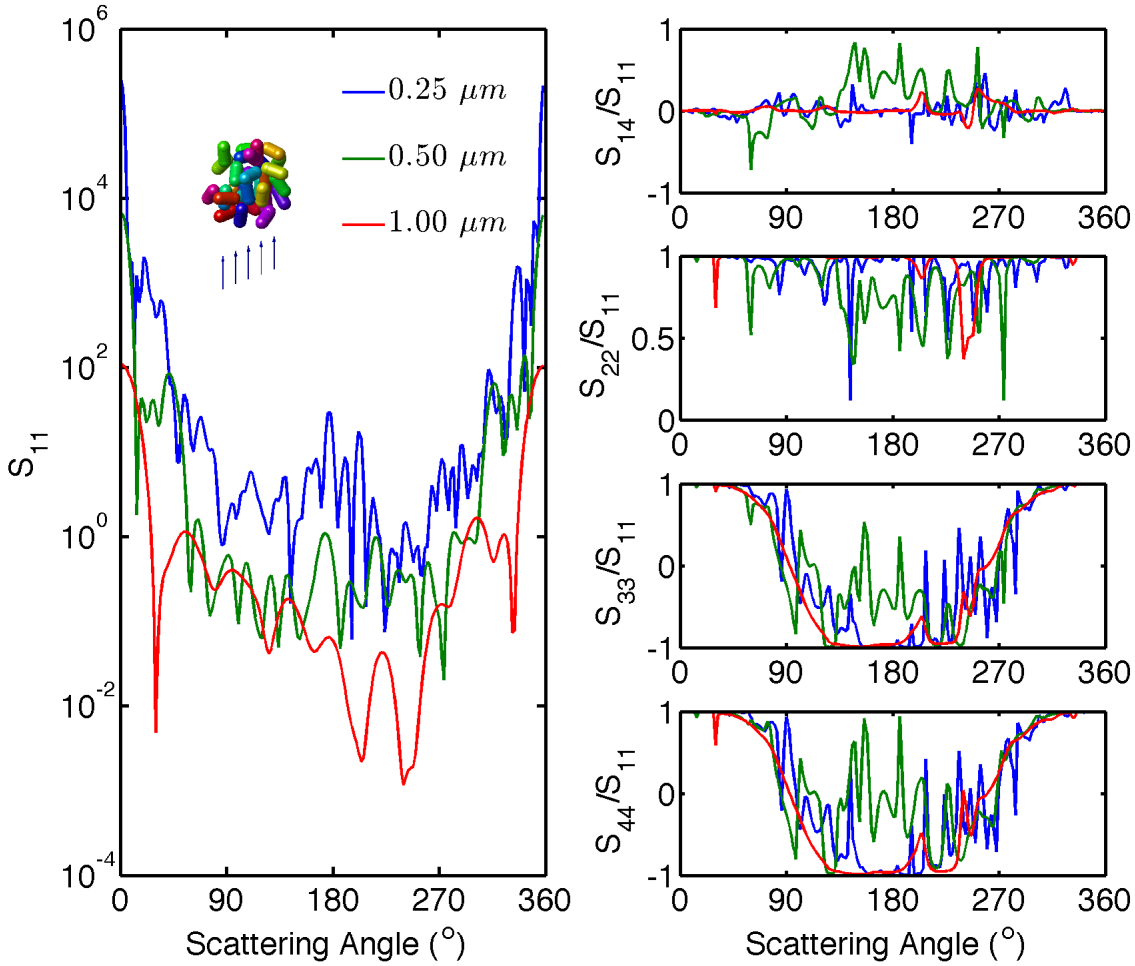

Figure 4.8: Mueller matrix elements from a fixed dinoflagellate calculated using the nucleus model (Fig. 4.1. (b)) and the simplified chromosome model (Fig. 4.2. (b)). Three different wavelengths are considered, 0.25, 0.50 and 1.0 μm. The nucleus has diameter 4.0 μm. The chromosome has diameter 0.5 μm, length 1.0 μm and pitch 0.5 μm. The refractive index used is $1.2 + 0.01i$ and the scattering plane is yz plane.

because there are always chromosomes in the nucleus lying roughly along the incident light and thus producing large $\mathbf{S}_{14}$ signals.

4.4.2 Light Scattering from a Suspension of Dinoflagellates

In order to simulate light scattering from a suspension of dinoflagellates, one needs to average the orientation of one single nucleus. For the time being, it is beyond our computational power due to the large number of dipoles and CPU hours required. Nevertheless, the Mueller matrix from an orientation averaged single chromosome should bear some resemblance to the Mueller matrix from a suspension of dinoflagellates. This approximation could even be accurate when chromosomes in the nucleus are far away from each other. In Fig. 4.9 we calculated the Mueller matrix elements from an orientations averaged chromosome based on the model in Fig. 4.2. (b) at various wavelengths. At each wavelength, a high positive lobe exists for $\mathbf{S}_{14}$ and its positions changes continuously from 45° to 180° as wavelength varies from 0.3 μm to 1.0 μm. The peak increases as wavelength increases from 0.3 μm, peaking around 0.1 at wavelength 0.7 μm, and decreases quickly to zero as wavelength further increases.

The largest backscattering signal of $\mathbf{S}_{14}$ is produced when the wavelength is about 0.8 μm, with a value of only 0.07 around 180° scattering angle, which is significantly smaller compared with the fixed nucleus case. But we can still safely say non-vanishing back scattering $\mathbf{S}_{14}$ signals from a suspension still persist. Note the differences between Fig. 4.6 and Fig. 4.9, where the distinct results stem from the fact that the model in Fig. 4.2. (b) is a highly simplified version of model in Fig. 4.2. (a) with much fewer layers and fibrils being used, and the sizes (0.5 μm and 1.0 μm diameters) and the diameter to pitch ratios (4 and 1, respectively) are also different.

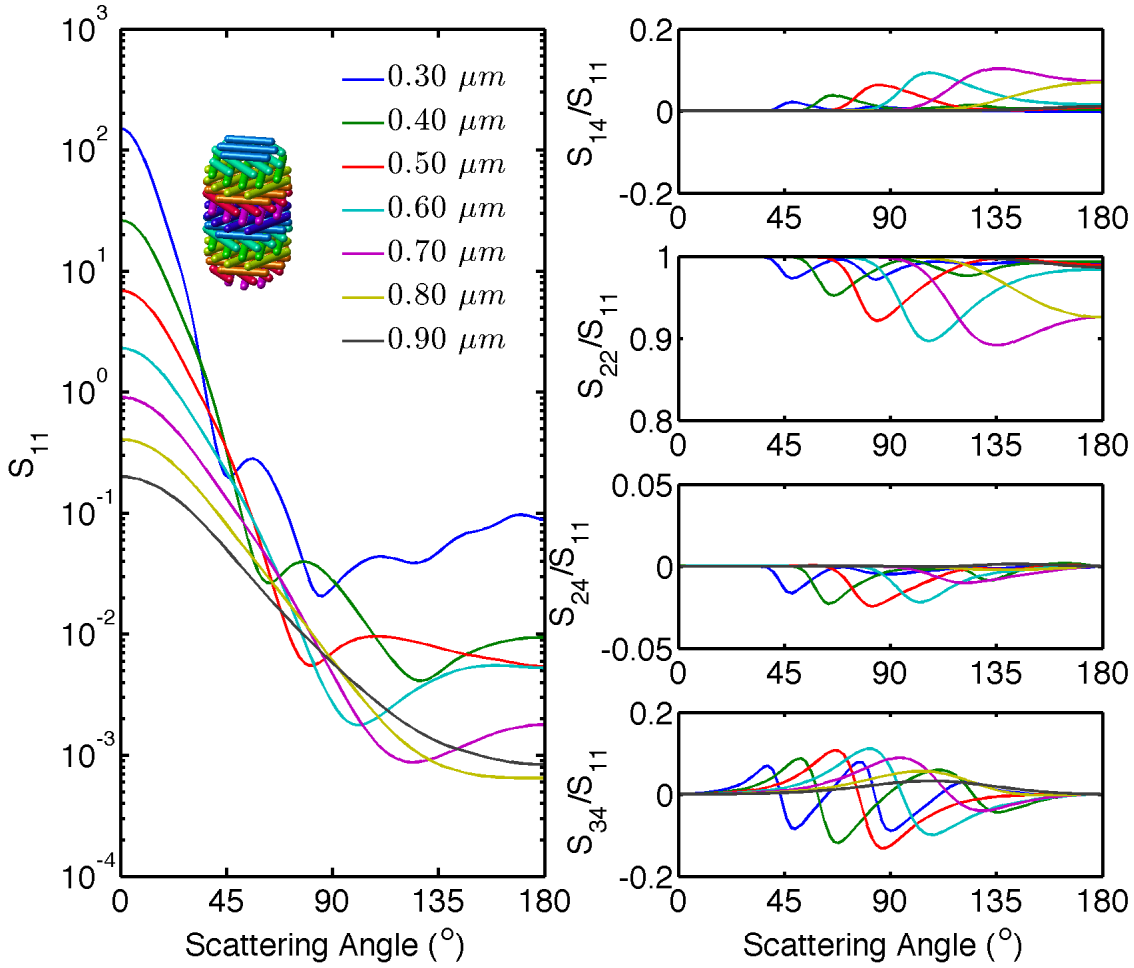

Figure 4.9: Mueller matrix elements from a single orientation averaged chromosome calculated using model (Fig. 4.2. (b)) when the wavelength is 0.3, 0.4, 0.5, 0.6, 0.7, 0.8, and 0.9 μm. The chromosome has diameter 0.5 μm, length 1.0 μm and pitch 0.5 μm. The refractive index used is $1.2 + 0.01i$.

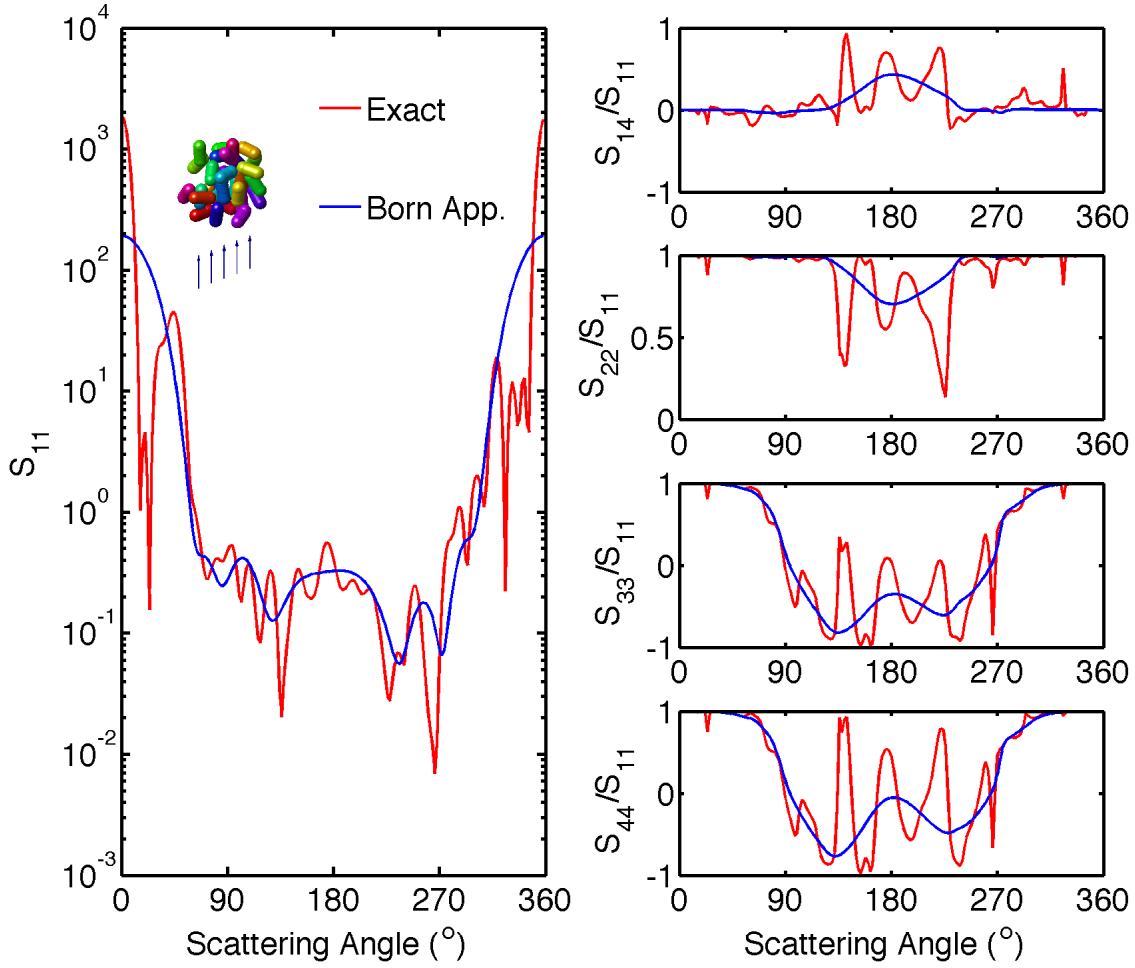

Figure 4.10: Mueller matrix elements from a fixed dinoflagellate calculated using the nucleus model (Fig. 4.1. (b)) and the simplified chromosome model (Fig. 4.2. (b)). The red line is the exact solution using ADDA, while the blue line is the result that all chromosomes are treated independently (Born approximation). In both cases, the light wavelength is 0.5 μm, which matches the pitch of the helical structure. The nucleus has diameter 4.0 μm. The chromosome has diameter 0.5 μm, length 1.0 μm and pitch 0.5 μm. The refractive index used is $1.2 + 0.01i$ and the scattering plane is yz-plane.

4.4.3 Effects of Coherence and Interactions

As we can see from Fig. 4.1, the nucleus of *K. brevis* is highly packed with chromosomes, which means the effects of interaction between chromosomes cannot be neglected and it is worthwhile to separate the effect of the intrinsic chirality of chromosomes and the effect of coherence and interactions. We approached it by calculating the Muller matrix elements as if each chromosome is independent, i.e. the Born approximation. A total of 10 random chromosomes are considered in one nucleus and the result is shown in Fig. 4.10, which is compared with the DDA exact solution. The result shows that significant non-vanishing $\mathbf{S}_{14}$ signals even in the Born approximation order, while those large high peaks can only result from the interactions and coherence effects.

4.5 Conclusions

We have developed a method to study light scattering from a dinoflagellate nucleus based on the liquid crystal model of chromosomes and using the ADDA code. The advantage of the liquid crystal model over the thin helix wire model used previously is its ability to account for more fine details of the chromosome structure, such as DNA fibrils. Our method is able to calculate all 16 Mueller matrix elements of light scattering from a single chromosome, an immobilized dinoflagellate nucleus and a suspension of dinoflagellate nuclei. The results of a single chromosome obtained agree with previous conclusions made by Shapiro et al. and Bustamante Shapiro et al. (see introduction section). For the scattering of a dinoflagellate nucleus, which has never been calculated before, our simulation shows that large backscattering can be obtained if the light wavelength matches the chiral parameter (pitch) of the chromosome. We further show that the largest peaks of $\mathbf{S}_{14}$ are contributed by the helical structures of chromosomes inside the nucleus.

Therefore our method provides a plausible way to detect red tide, whose causal agent is dinoflagellates, by measuring back scattering Mueller matrix elements such as $\mathbf{S}_{14}$ that are

more sensitive to internal helical structures of chromosomes than to the shapes of cellular structures. In order to produce large signals, the wavelength of incident light used should be close to the pitch of chromosomes (about 250 nm for *P. micans* and 120 nm for *K. brevis*), which means the best probing light is in the ultraviolet region.

5. SCATTERING OF PARTIALLY COHERENT ELECTROMAGNETIC BEAMS BY WATER DROPLETS AND ICE CRYSTALS*

The conventional Lorenz-Mie theory is generalized for a case when the light source is partially spatially coherent. The influence of the degree of coherence of the incident field on the generalized Mueller matrix and the spectral degree of coherence of the scattered light is analytically studied by using the vector field instead of the scalar field to extend previous results on the angular intensity distribution. The results are compared with the Mueller matrix obtained from the Discrete Dipole Approximation (DDA) method, which is an average over an ensemble of stochastic incident beams. Special attention is paid to the Mueller matrix elements in the backward direction, and the results show some Mueller matrix elements, such as $\mathbf{P}_{22}$, depend monotonically on the coherence length of the incident beam. Therefore, detecting back scattering Mueller matrix elements may be a promising method to measure the degree of coherence. The new formalism is applied to cases of large spherical droplets in water clouds and hexagonal ice crystals in cirrus clouds. The corona and glory phenomena due to spheres and halos associated with hexagonal ice crystals are found to disappear if the incident light tends to be highly incoherent.

5.1 Introduction

In the conventional theories of light scattering, such as Lorenz-Mie theory [20], Discrete Dipole Approximation (DDA) [21, 23], and Finite-Difference Time-Domain (FDTD) method [42], the incident light is generally assumed to be fully coherent in both space and time. However, the assumption is not always justified. In reality, light acquires some degree of incoherence due to light source fluctuations or to interactions with random media

*This chapter is reprinted from Journal of Quantitative Spectroscopy & Radiative Transfer, **134**, 74-84, 2014, J. P. Liu, L. Bi, P. Yang, and G. W. Kattawar, "Scattering of partially coherent electromagnetic beams by water droplets and ice crystals", Copyright 2014, with permission from Elsevier.

such as a turbulent atmosphere. Although the general framework of optical coherence theory has long been well established [24, 25, 26], scarcely any attention has been paid to the effect of coherence on light scattering by deterministic media. The influence of spatial coherence on scattering by a particle was partially investigated by Cabaret *et al.* [27] and Greffe [28]. The extinction cross section of rotationally invariant scatterers was found not to depend on the transverse (or spatial) coherence length, but the extinction cross section of anisotropic scatterers did depend on the state of coherence of the illuminating field. Further research on the topic was conducted by van Dijk [2] and Fischer [29], who studied the effects of spatial coherence on the angular distribution of radiant intensity scattered by a sphere. By using the angular spectrum representation of a random field [24] and half wave expansion of the scattering amplitude, the intensity of a scattered field was analytically obtained. The angular distribution of radiant intensity depends strongly on the degree of coherence, but the extinguished power does not. Sukhov [43] numerically studied the effect of spatial coherence by a random medium on the properties of scattered fields, and the DDA method was used to demonstrate that the statistical properties of the scattered light from an inhomogeneous medium were altered due to coherence effects.

Previous theories have been limited to the study of the scattered field intensity, which does not fully describe a scatterer with respect to light scattering. A common generalization is to study the Mueller matrix, which relates the Stokes vector of the incident beam to the Stokes vector of the scattered beam. For a large class of light beams such as the so-called Gaussian Schell-model beam, the Mueller matrix for a sphere is derived analytically by extending the Lorenz-Mie theory. We developed a DDA code [21] by modifying the source field to incorporate incoherence, and the Mueller matrix was obtained by averaging over an ensemble of stochastic incident fields. In addition, we investigated the spectral degree of coherence of the scattered light. As applications of the formalism developed, we performed the computation of light scattering by water droplets and hexagonal ice crystals,

which are the major scatterers inside atmospheric clouds. The coherence effects of spherical water droplets were studied by modifying the Lorenz-Mie theory. With the Invariant Imbedding T-matrix method (see [44] and references cited therein), we were able to study the coherence effects on halos of large hexagonal ice crystals.

5.2 Scattering of Partially Coherent Light by a Sphere

We consider the scattering of electromagnetic beams of an arbitrary state of spatial coherence by a homogenous sphere on the basis of a generalization of previous results in [2, 29]. Note that the procedure is quite similar to that used by Lahiri and Wolf [45], where the refraction and reflection of partially coherent electromagnetic beams were considered.

5.2.1 Theory of Coherence

We use some of the important results from the coherence theory of electromagnetic beams [26]. The stochastic nature of incoherent monochromatic light is represented by an ensemble of random fields $\{\mathbf{E}(\mathbf{r},\omega)\}$, where ω is the frequency, and for each realization, the field component is transverse to the direction of propagation. By choosing a plane of reference, each random field can be expressed as

$$\begin{pmatrix} E_l(\mathbf{r},\omega) \\ E_r(\mathbf{r},\omega) \end{pmatrix}, \tag{5.1}$$

where subscripts "r" and "l" denote the perpendicular and parallel components, respectively.

Following the same formalism used by Wolf [26], the second-order correlation properties of the stochastic field are fully characterized by the cross-spectral density matrix

(CSDM) defined by

$$\begin{aligned}\mathbf{W}(\mathbf{r}_1,\mathbf{r}_2,\omega) &= \langle \mathbf{E}^*(\mathbf{r}_1,\omega)\cdot\mathbf{E}^T(\mathbf{r}_2,\omega)\rangle \\ &= \begin{pmatrix} \langle E_l^*(\mathbf{r}_1,\omega)E_l(\mathbf{r}_2,\omega)\rangle & \langle E_l^*(\mathbf{r}_1,\omega)E_r(\mathbf{r}_2,\omega)\rangle \\ \langle E_r^*(\mathbf{r}_1,\omega)E_l(\mathbf{r}_2,\omega)\rangle & \langle E_r^*(\mathbf{r}_1,\omega)E_r(\mathbf{r}_2,\omega)\rangle \end{pmatrix},\end{aligned} \tag{5.2}$$

where superscript " $*$ " denotes the complex conjugate, "T" denotes the transpose of a matrix and $\langle \quad \rangle$ means the ensemble average. From the CSDM, the spectral density can be derived at point $\mathbf{r}$ and at frequency ω

$$S(\mathbf{r},\omega) = \mathrm{Tr}\mathbf{W}(\mathbf{r},\mathbf{r},\omega), \tag{5.3}$$

which can be interpreted as a contribution to the intensity at point $\mathbf{r}$ from the field component of frequency ω. The spatial degree of coherence of the random field is defined by [26]

$$\eta(\mathbf{r}_1,\mathbf{r}_2,\omega) = \frac{\mathrm{Tr}\mathbf{W}(\mathbf{r}_1,\mathbf{r}_2,\omega)}{\sqrt{S(\mathbf{r}_1,\omega)}\sqrt{S(\mathbf{r}_2,\omega)}}, \tag{5.4}$$

which unifies both polarization and coherence. Note that $0 \leq |\eta(\mathbf{r}_1,\mathbf{r}_2,\omega)| \leq 1$, with 0 representing complete incoherence and 1 representing complete coherence.

5.2.2 Incident Light

Incoherent beams can be represented by an ensemble of random fields and are realized using the angular spectrum representation [24]. A partially coherent beam propagating in the $+z$ direction can be expressed as

$$\mathbf{E}^{(i)}(\mathbf{r},\omega) = \int_{|\mathbf{u}'_\perp|\leq 1} \mathbf{e}^{(i)}(\mathbf{u}'_\perp,\omega)\exp(ik\hat{\mathbf{u}}'\cdot\mathbf{r})d^2\mathbf{u}'_\perp, \tag{5.5}$$

where the coefficient $\mathbf{e}^{(i)}(\mathbf{u}'_\perp, \omega)$ is a two-component random vector defined by

$$\mathbf{e}^{(i)}(\mathbf{u}'_\perp, \omega) = \begin{pmatrix} e_l^{(i)}(\mathbf{u}'_\perp, \omega) \\ e_r^{(i)}(\mathbf{u}'_\perp, \omega) \end{pmatrix}, \tag{5.6}$$

$k = \omega/c$ is the wavenumber, $\hat{\mathbf{u}}'$ is the direction of propagation of each plane wave component, $\mathbf{u}'_\perp = (u'_x, u'_y)$ is the projection of $\hat{\mathbf{u}}'$ onto the $z = 0$ plane, and the unit vector $\hat{\mathbf{u}}'$ points into the $z > 0$ half space, i.e. $u'_z = \sqrt{1 - |\mathbf{u}'_\perp|^2}$. The scattering plane is chosen as the reference plane.

The incident field is uniquely defined by the source at the $z = 0$ plane, which is characterized by the CSDM

$$\mathbf{W}^{(i)}(\boldsymbol{\rho}_1, \boldsymbol{\rho}_2, \omega) = \langle \mathbf{E}^{(i)*}(\boldsymbol{\rho}_1, \omega) \cdot \mathbf{E}^{(i)T}(\boldsymbol{\rho}_2, \omega) \rangle, \tag{5.7}$$

where $\boldsymbol{\rho}_1$ and $\boldsymbol{\rho}_2$ are 2D vectors in the $z = 0$ plane. Using Eq. (5.5), we have

$$\mathbf{W}^{(i)}(\boldsymbol{\rho}_1, \boldsymbol{\rho}_2, \omega) = \int d^2\mathbf{u}'_\perp d^2\mathbf{u}''_\perp \tilde{\mathbf{W}}^{(i)}(\mathbf{u}'_\perp, \mathbf{u}''_\perp, \omega) \exp\left(-ik\left(\mathbf{u}'_\perp \cdot \boldsymbol{\rho}_1 - \mathbf{u}''_\perp \cdot \boldsymbol{\rho}_2\right)\right), \tag{5.8}$$

where the angular correlation matrix $\tilde{\mathbf{W}}^{(i)}(\mathbf{u}'_\perp, \mathbf{u}''_\perp, \omega) = \langle \mathbf{e}^{(i)*}(\mathbf{u}'_\perp) \cdot \mathbf{e}^{(i)T}(\mathbf{u}''_\perp) \rangle$ is defined as a four-dimensional Fourier transformation of the CSDM at the $z = 0$ plane, i.e.

$$\tilde{\mathbf{W}}^{(i)}(\mathbf{u}'_\perp, \mathbf{u}''_\perp, \omega) = \left(\frac{k}{2\pi}\right)^2 \int d^2\boldsymbol{\rho}_1 d^2\boldsymbol{\rho}_2 \mathbf{W}^{(i)}(\boldsymbol{\rho}_1, \boldsymbol{\rho}_2, \omega) \exp\left(ik\left(\mathbf{u}'_\perp \cdot \boldsymbol{\rho}_1 - \mathbf{u}''_\perp \cdot \boldsymbol{\rho}_2\right)\right). \tag{5.9}$$

We consider a widely used class of partially coherent beams, the so-called Gaussian Schell-model beams, which have the following CSDM elements

$$\mathbf{W}_{lm}^{(i)}(\boldsymbol{\rho}_1, \boldsymbol{\rho}_2, \omega) = a_l a_m b_{lm} \exp\left(-\frac{\boldsymbol{\rho}_1^2 + \boldsymbol{\rho}_2^2}{4\sigma_S^2}\right) \exp\left(-\frac{(\boldsymbol{\rho}_1 - \boldsymbol{\rho}_2)^2}{2\sigma_\mu^2}\right), \tag{5.10}$$

where $l, m = 1, 2$. The independently chosen parameter σ_S can be interpreted as the width of the beam, and σ_μ as the coherence length. The remaining parameters in Eq. (A.9) have the following constraints [26]

$$\begin{aligned} b_{ij} &= 1 \quad \text{when} \quad i = j, && (5.11)\\ |b_{ij}| &\leq 1 \quad \text{when} \quad i \neq j, && (5.12)\\ b_{ij} &= b^*_{ji}, && (5.13)\\ a_i &\geq 0. && (5.14) \end{aligned}$$

By substituting Eq. (A.9) into Eq. (5.9) and performing the four dimensional integration, one can obtain the angular correlation matrix [2]

$$\begin{aligned} &\tilde{\mathbf{W}}^{(i)}(\mathbf{u}'_\perp, \mathbf{u}''_\perp, \omega) \\ &= a_l a_m b_{lm} \left(\frac{k^2 \sigma_\mu \sigma_{\text{eff}}}{2\pi} \right)^2 \exp\left\{ -\frac{k^2}{2} \left[(\mathbf{u}'_\perp - \mathbf{u}''_\perp)^2 \sigma_S^2 + (\mathbf{u}'_\perp + \mathbf{u}''_\perp)^2 \frac{\sigma_{\text{eff}}^2}{4} \right] \right\}, \end{aligned} \tag{5.15}$$

where σ_{eff} is defined through

$$\frac{1}{\sigma_{\text{eff}}^2} = \frac{1}{\sigma_\mu^2} + \frac{1}{4\sigma_S^2}. \tag{5.16}$$

In order to obtain the Mueller matrix, knowledge of the Stokes vector of the incident beam is required. According to the definition, the Stokes vector is closely related to the 2×2 polarization matrix [26]

$$\begin{aligned} \mathbf{W}(\mathbf{r}, \mathbf{r}, \omega) &= \langle \mathbf{E}^*(\mathbf{r}, \omega) \cdot \mathbf{E}^T(\mathbf{r}, \omega) \rangle \\ &= \begin{pmatrix} \langle E_l^*(\mathbf{r}, \omega) E_l(\mathbf{r}, \omega) \rangle & \langle E_l^*(\mathbf{r}, \omega) E_r(\mathbf{r}, \omega) \rangle \\ \langle E_r^*(\mathbf{r}, \omega) E_l(\mathbf{r}, \omega) \rangle & \langle E_r^*(\mathbf{r}, \omega) E_r(\mathbf{r}, \omega) \rangle \end{pmatrix}. \end{aligned} \tag{5.17}$$

From Eq. (5.17), we can get the incident Stokes vector $\mathbf{I}^{(i)}(\mathbf{r},\omega)$ at point $\mathbf{r}$

$$\mathbf{I}^{(i)}(\mathbf{r},\omega)=\begin{pmatrix}\mathbf{W}_{ll}^{(i)}(\mathbf{r},\mathbf{r},\omega)+\mathbf{W}_{rr}^{(i)}(\mathbf{r},\mathbf{r},\omega)\\ \mathbf{W}_{ll}^{(i)}(\mathbf{r},\mathbf{r},\omega)-\mathbf{W}_{rr}^{(i)}(\mathbf{r},\mathbf{r},\omega)\\ \mathbf{W}_{rl}^{(i)}(\mathbf{r},\mathbf{r},\omega)+\mathbf{W}_{lr}^{(i)}(\mathbf{r},\mathbf{r},\omega)\\ i\left(\mathbf{W}_{rl}^{(i)}(\mathbf{r},\mathbf{r},\omega)-\mathbf{W}_{lr}^{(i)}(\mathbf{r},\mathbf{r},\omega)\right)\end{pmatrix}. \tag{5.18}$$

However, such a Stokes vector is spatially dependent and would make the Mueller matrix ill defined. One solution is to define the Stokes vector of the incident beam at the $z=0$ plane and let the width of the beam go to infinity. From Eq. (A.9), we immediately have the Gaussian Schell-model beam

$$\mathbf{W}_{lm}^{(i)}(\boldsymbol{\rho},\boldsymbol{\rho},\omega)=a_l a_m b_{lm}, \tag{5.19}$$

which is a constant 2×2 matrix. Analogously, the angular correlation matrix in the same limit can written as

$$\tilde{\mathbf{W}}_{lm}^{(i)}(\mathbf{u}'_{\perp},\mathbf{u}''_{\perp},\omega)=a_l a_m b_{lm}\frac{k^2\sigma_\mu^2}{2\pi}\exp\left\{-\frac{1}{2}k^2\sigma_\mu^2|\mathbf{u}'_{\perp}|^2\right\}\delta^2\left(\mathbf{u}'_{\perp}-\mathbf{u}''_{\perp}\right). \tag{5.20}$$

Thus, under this condition, we can generalize the Mueller matrix to the case of incoherent beam scattering.

5.2.3 Scattered Light

In the previous section, the incident field amplitude is defined with reference to the main scattering plane, which is defined with respect to the whole incoherent beam. However, for each plane wave component of the incident beam, the scattering plane is different from the main scattering plane because the wave vector is different from that of the incident beam. Therefore, each plane wave component must experience a series of coordinate

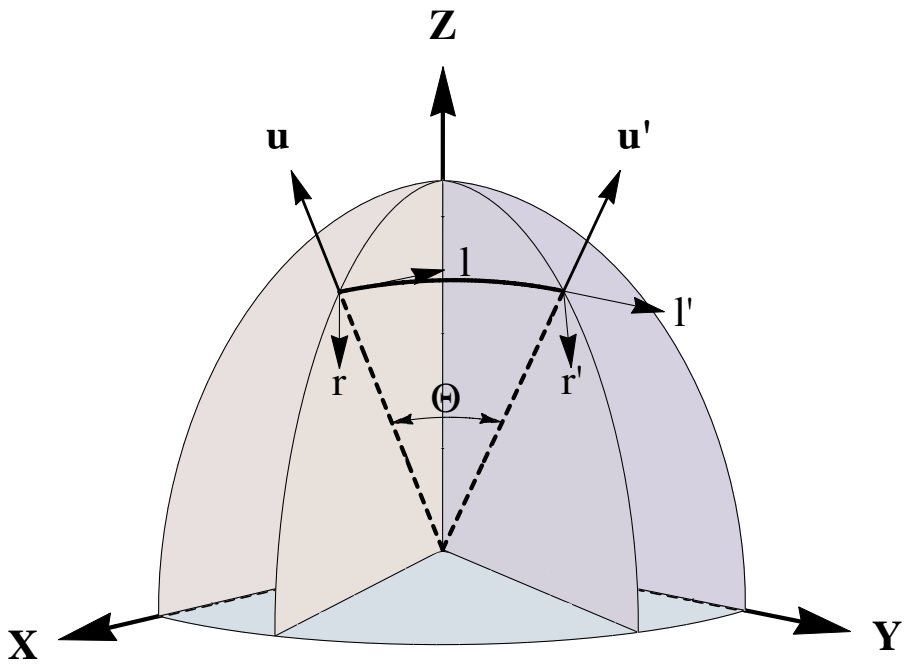

Figure 5.1: The geometry of Mie scattering, where $\hat{\mathbf{u}}'$ is the incident direction, $\hat{\mathbf{u}}$ is the scattering direction, and Θ is the scattering angle.

rotations in order to be placed in the fixed scattering plane.

Due to the rotational symmetry of homogenous spheres and the incident beam about the axis, the scattering direction can be chosen to be

$$\hat{\mathbf{u}} = (\sin\theta, 0, \cos\theta), \tag{5.21}$$

which implies the main scattering plane coincides with the meridian plane that contains vector $\hat{\mathbf{u}}$ (see Fig. 5.2). Now consider the plane wave component $\mathbf{e}^{(i)}(\mathbf{u}'_{\perp}, \omega)\exp(ik\hat{\mathbf{u}}' \cdot \mathbf{r})$, where the amplitude is defined with reference to the meridian plane of $\hat{\mathbf{u}}$. First, we transform the reference plane to the meridian plane of $\hat{\mathbf{u}}'$, which can be done through a

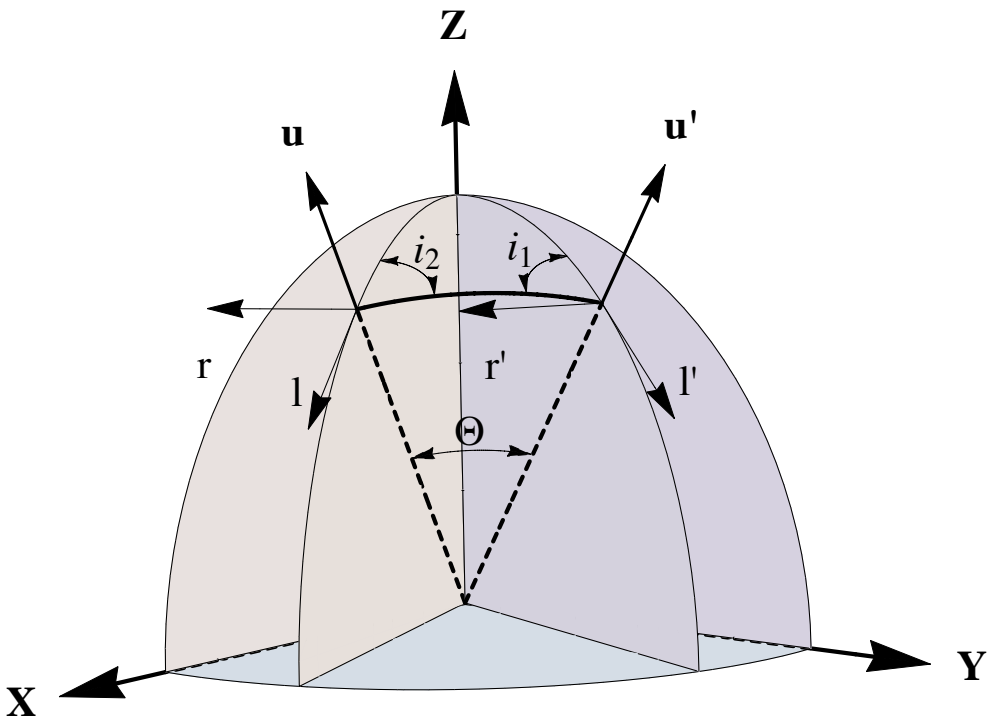

Figure 5.2: Scattering of one plane wave component of the partially coherent beam, where $\hat{\mathbf{u}}'$ is the incident direction, $\hat{\mathbf{u}}$ is the scattering direction, and Θ is the scattering angle. i_1 is the angle between the meridian plane containing $\hat{\mathbf{u}}'$ and the scattering plane, and i_2 is the angle between the meridian plane containing $\hat{\mathbf{u}}$ and the scattering plane.

rotation about the z axis, i.e.

$$\begin{pmatrix} e_l^{(i)} \\ e_r^{(i)} \end{pmatrix} \rightarrow \begin{pmatrix} \cos\phi' & -\sin\phi' \\ \sin\phi' & \cos\phi' \end{pmatrix} \begin{pmatrix} e_l^{(i)} \\ e_r^{(i)} \end{pmatrix}, \tag{5.22}$$

or in a more compact form $e^{(i)} \rightarrow \mathbf{R}(\phi')e^{(i)}$, where the fact is used that the unit vector $\hat{\mathbf{u}}'$ has a spherical coordinate (θ', ϕ'). Second, we consider the scattering of a plane wave from direction $\hat{\mathbf{u}}'$ into direction $\hat{\mathbf{u}}$. Since in the Lorenz-Mie scattering the change of amplitude is defined with respect to the scattering plane, the incident field amplitude has to be transformed from the meridian plane to scattering plane by a counterclockwise rotation about vector $\hat{\mathbf{u}}'$ with an angle i_1 (see Fig. 5.2), which is the angle between the meridian plane of $\hat{\mathbf{u}}'$ and the scattering plane spanned by vectors $\hat{\mathbf{u}}'$ and $\hat{\mathbf{u}}$. Thus, the amplitude of the incident field can be written as

$$\mathbf{R}(i_1)\mathbf{R}(\phi')\mathbf{e}^{(i)}. \tag{5.23}$$

By applying the results of the Lorenz-Mie theory, we obtain the scattered field in the scattering plane of $\hat{\mathbf{u}}'$ and $\hat{\mathbf{u}}$

$$\mathbf{S}(\Theta)\mathbf{R}(i_1)\mathbf{R}(\phi')\mathbf{e}^{(i)}, \tag{5.24}$$

where Θ is the angle between $\hat{\mathbf{u}}'$ and $\hat{\mathbf{u}}$, and $\mathbf{S}(\Theta)$ is the scattering amplitude matrix of Lorenz-Mie scattering, which is given by [31]

$$\mathbf{S}(\Theta) = \begin{pmatrix} S_2(\Theta) & 0 \\ 0 & S_1(\Theta) \end{pmatrix} \tag{5.25}$$

Third, the scattered field has to be expressed with respect to the main scattering plane, and is obtained by a clockwise rotation about vector $\hat{\mathbf{u}}$ with an angle $\pi - i_2$, where i_2 is the

angle between the scattering plane spanned by vector $\hat{\mathbf{u}}'$ and $\hat{\mathbf{u}}$. The resulting scattered field reads

$$\mathbf{R}^{-1}(\pi - i_2)\mathbf{S}(\Theta)\mathbf{R}(i_1)\mathbf{R}(\phi')\mathbf{e}^{(i)}, \tag{5.26}$$

which is equivalent to

$$-\mathbf{R}(i_2)\mathbf{S}(\Theta)\mathbf{R}(i_1)\mathbf{R}(\phi')\mathbf{e}^{(i)} \tag{5.27}$$

after using the relation $\mathbf{R}^{-1}(\pi - i_2) = -\mathbf{R}(i_2)$.

Note that the above argument only works when $\phi' < \pi$ or $(\hat{\mathbf{u}} \times \hat{\mathbf{u}}') \cdot \hat{z} > 0$. When $(\hat{\mathbf{u}} \times \hat{\mathbf{u}}') \cdot \hat{z} < 0$, the scattered field in the main scattering plane is given by

$$\mathbf{R}^{-1}(i_2)\mathbf{S}(\Theta)\mathbf{R}(\pi - i_1)\mathbf{R}(\phi')\mathbf{e}^{(i)} = -\mathbf{R}(-i_2)\mathbf{S}(\Theta)\mathbf{R}(-i_1)\mathbf{R}(\phi')\mathbf{e}^{(i)}, \tag{5.28}$$

which is essentially the same as Eq. (5.27) except that the signs of $\sin i_1$ and $\sin i_2$ are reversed. Therefore, after obtaining $\cos i_1$ and $\cos i_2$ from spherical trigonometry, namely

$$\cos i_1 = \frac{\cos\theta - \cos\theta' \cos\Theta}{\sin\theta' \sin\Theta}, \tag{5.29}$$

$$\cos i_2 = \frac{\cos\theta' - \cos\theta \cos\Theta}{\sin\theta \sin\Theta}, \tag{5.30}$$

$\sin i_1$ and $\sin i_2$ are given by

$$\sin i_1 = \frac{(\hat{\mathbf{u}} \times \hat{\mathbf{u}}') \cdot \hat{z}}{|(\hat{\mathbf{u}} \times \hat{\mathbf{u}}') \cdot \hat{z}|} \sqrt{1 - \cos^2 i_1}, \tag{5.31}$$

$$\sin i_2 = \frac{(\hat{\mathbf{u}} \times \hat{\mathbf{u}}') \cdot \hat{z}}{|(\hat{\mathbf{u}} \times \hat{\mathbf{u}}') \cdot \hat{z}|} \sqrt{1 - \cos^2 i_2}, \tag{5.32}$$

where $\cos\Theta = \hat{\mathbf{u}}' \cdot \hat{\mathbf{u}}$.

We obtain the total scattered field referenced to the main scattering plane

$$\mathbf{E}^{(s)}\left(r\hat{\mathbf{u}},\omega\right)=\frac{\exp(ikr)}{ikr}\int\mathbf{A}\left(\hat{\mathbf{u}},\hat{\mathbf{u}}'\right)\cdot\mathbf{e}^{(i)}\left(\hat{\mathbf{u}}'_{\perp},\omega\right)d^{2}\mathbf{u}'_{\perp}, \tag{5.33}$$

where the 2×2 matrix $\mathbf{A}(\hat{\mathbf{u}},\hat{\mathbf{u}}')$ is defined by

$$\mathbf{A}\left(\hat{\mathbf{u}},\hat{\mathbf{u}}'\right)=-\mathbf{R}(i_2)\mathbf{S}(\Theta)\mathbf{R}(i_1)\mathbf{R}(\phi'). \tag{5.34}$$

5.2.4 Mueller Matrix

Once the scattered field is obtained, we can calculate the CSDM

$$\begin{aligned}\mathbf{W}^{(s)}(r_1\hat{\mathbf{u}}_1,r_2\hat{\mathbf{u}}_2,\omega)=\frac{\exp(-ik(r_1-r_2))}{k^2r_1r_2}\int d^2\hat{\mathbf{u}}'_{\perp}d^2\hat{\mathbf{u}}''_{\perp}\mathbf{A}^{*}(\hat{\mathbf{u}}_1,\hat{\mathbf{u}}')\\ \cdot\tilde{\mathbf{W}}^{(i)}\left(\hat{\mathbf{u}}'_{\perp},\hat{\mathbf{u}}''_{\perp},\omega\right)\cdot\mathbf{A}^{T}\left(\hat{\mathbf{u}}_2,\hat{\mathbf{u}}''\right),\end{aligned} \tag{5.35}$$

with the definition of the angular correlation matrix of the incident field given by

$$\tilde{\mathbf{W}}^{(i)}\left(\hat{\mathbf{u}}'_{\perp},\hat{\mathbf{u}}''_{\perp},\omega\right)=\left\langle\mathbf{e}^{(i)*}\left(\hat{\mathbf{u}}'_{\perp},\omega\right)\cdot\mathbf{e}^{(i)T}\left(\hat{\mathbf{u}}''_{\perp},\omega\right)\right\rangle. \tag{5.36}$$

Taking the limit that the width of the Gaussian Schell-model beam goes to infinity, which implies that Eq. (5.20) holds, we obtain

$$\begin{aligned}\mathbf{W}^{(s)}(r_1\hat{\mathbf{u}}_1,r_2\hat{\mathbf{u}}_2,\omega) &= \frac{\exp(-ik(r_1-r_2))}{k^2r_1r_2}\frac{k^2\sigma_\mu^2}{2\pi}\int d^2\hat{\mathbf{u}}'_{\perp}\mathbf{A}^{*}(\hat{\mathbf{u}}_1,\hat{\mathbf{u}}')\cdot\mathbf{W}^{(i)}(z=0)\\ &\quad\cdot\mathbf{A}^{T}\left(\hat{\mathbf{u}}_2,\hat{\mathbf{u}}'\right)\times\exp\left\{-\frac{1}{2}k^2\sigma_\mu^2\left|\hat{\mathbf{u}}'_{\perp}\right|^2\right\},\end{aligned} \tag{5.37}$$

where $\mathbf{W}^{(i)}(z=0)$ is the polarization matrix of the incident beam defined at the $z=0$ plane. From Eq. (5.38), we have the polarization matrix at point $r\hat{\mathbf{u}}$

$$\begin{aligned}\mathbf{W}^{(s)}(r\hat{\mathbf{u}}_1, r\hat{\mathbf{u}}_2, \omega) &= \frac{1}{k^2r^2}\frac{k^2\sigma_\mu^2}{2\pi}\int d^2\hat{\mathbf{u}}'_\perp \mathbf{A}^*(\hat{\mathbf{u}}, \hat{\mathbf{u}}') \cdot \mathbf{W}^{(i)}(z=0) \cdot \mathbf{A}^T(\hat{\mathbf{u}}, \hat{\mathbf{u}}') \\ &\quad \times \exp\left\{-\frac{1}{2}k^2\sigma_\mu^2 \left|\hat{\mathbf{u}}'_\perp\right|^2\right\}. \end{aligned} \tag{5.38}$$

Using the relation between the Stokes vector and the polarization matrix (Eq. (5.18)), and the definition of the Mueller matrix

$$\mathbf{I}^{(s)}(\hat{\mathbf{u}}) = \frac{1}{k^2r^2}\mathbf{P}(\hat{\mathbf{u}}) \cdot \mathbf{I}^{(i)}(\hat{z}), \tag{5.39}$$

we get the 4×4 Mueller matrix $\mathbf{P}(\hat{\mathbf{u}})$, given by

$$\mathbf{P}(\hat{\mathbf{u}}) = \frac{k^2\sigma_\mu^2}{2\pi}\int d^2\hat{\mathbf{u}}'_\perp \exp\left\{-\frac{1}{2}k^2\sigma_\mu^2 \left|\hat{\mathbf{u}}'_\perp\right|^2\right\} \mathbf{M}(\hat{\mathbf{u}}, \hat{\mathbf{u}}'). \tag{5.40}$$

Here, the 4×4 matrix $\mathbf{M}(\hat{\mathbf{u}}, \hat{\mathbf{u}}')$ is the Mueller matrix defined from the effective amplitude matrix $\mathbf{A}(\hat{\mathbf{u}}, \hat{\mathbf{u}}')$. Some selected matrix elements of $\mathbf{M}(\hat{\mathbf{u}}, \hat{\mathbf{u}}')$ are listed below

$$\mathbf{M}_{11} = \left(|A_1|^2 + |A_2|^2 + |A_3|^2 + |A_4|^2\right)/2, \tag{5.41a}$$
$$\mathbf{M}_{12} = \left(|A_2|^2 - |A_1|^2 + |A_4|^2 - |A_2|^2\right)/2, \tag{5.41b}$$
$$\mathbf{M}_{22} = \left(|A_1|^2 + |A_2|^2 - |A_3|^2 - |A_4|^2\right)/2, \tag{5.41c}$$
$$\mathbf{M}_{33} = \mathrm{Re}\left(A_1A_2^* + A_3A_4^*\right), \tag{5.41d}$$
$$\mathbf{M}_{43} = \mathrm{Im}\left(A_1A_2^* - A_3A_4^*\right), \tag{5.41e}$$
$$\mathbf{M}_{44} = \mathrm{Re}\left(A_1A_2^* - A_3A_4^*\right), \tag{5.41f}$$

where $A_1 = \mathbf{A}_{22}$, $A_2 = \mathbf{A}_{11}$, $A_3 = \mathbf{A}_{12}$, and $A_4 = \mathbf{A}_{21}$. Substituting Eq. (5.34) into Eq. (5.41), we find the relation between the matrix and the Mueller matrix of a sphere in the fully coherent case $\mathbf{P}^{(0)}$

$$\mathbf{M}_{11} = \mathbf{P}_{11}^{(0)}, \tag{5.42a}$$
$$\mathbf{M}_{12} = \mathbf{P}_{11}^{(0)} \cos\left(2\left(i_1 + \phi'\right)\right), \tag{5.42b}$$
$$\mathbf{M}_{22} = \mathbf{P}_{11}^{(0)} \cos 2i_2 \cos\left(2\left(i_1 + \phi'\right)\right) - \mathbf{P}_{33}^{(0)} \sin 2i_2 \sin\left(2\left(i_1 + \phi'\right)\right), \tag{5.42c}$$
$$\mathbf{M}_{33} = -\mathbf{P}_{11}^{(0)} \sin 2i_2 \sin\left(2\left(i_1 + \phi'\right)\right) + \mathbf{P}_{33}^{(0)} \cos 2i_2 \cos\left(2\left(i_1 + \phi'\right)\right), \tag{5.42d}$$
$$\mathbf{M}_{43} = \mathbf{P}_{43}^{(0)} \cos\left(2\left(i_1 + \phi'\right)\right), \tag{5.42e}$$
$$\mathbf{M}_{44} = \mathbf{P}_{44}^{(0)}. \tag{5.42f}$$

Together with Eq. (5.40), we can calculate the Mueller matrix of a sphere when the incident light has an arbitrary degree of coherence.

5.2.5 Spectral Degree of Coherence

Once the CSDM is obtained, we can study the spectral degree of coherence of the scattered field. According to the definition in Eq. (A.4), the degree of coherence $\eta^{(s)}(r_1\hat{\mathbf{u}}_1, r_2\hat{\mathbf{u}}_2, \omega)$ between two directions in the far field zone can be written as

$$\eta^{(s)}(r_1\hat{\mathbf{u}}_1, r_2\hat{\mathbf{u}}_2, \omega) = \frac{\mathrm{Tr}\mathbf{W}^{(s)}(r_1\hat{\mathbf{u}}_1, r_2\hat{\mathbf{u}}_2, \omega)}{\sqrt{S^{(s)}(r_1\hat{\mathbf{u}}_1, \omega)}\sqrt{S^{(s)}(r_1\hat{\mathbf{u}}_2, \omega)}}. \tag{5.43}$$

We consider a special case where the incident beam is completely unpolarized, i.e. the CSDM at $z = 0$ takes the form

$$\mathbf{W}_{lm}^{(i)}(z = 0) = I\delta_{lm}, \quad l, m = 1, 2. \tag{5.44}$$

Therefore, the CSDM of the scattered field is given by

$$\begin{aligned}\mathbf{W}^{(s)}(r_1\hat{\mathbf{u}}_1, r_2\hat{\mathbf{u}}_2, \omega) = I\frac{\exp(-ik(r_1 - r_2))}{k^2 r_1 r_2}\frac{k^2\sigma_\mu^2}{2\pi}\int d^2\hat{\mathbf{u}}'_\perp \mathbf{A}^*(\hat{\mathbf{u}}_1, \hat{\mathbf{u}}') \\ \cdot \mathbf{A}^T(\hat{\mathbf{u}}_2, \hat{\mathbf{u}}') \times \exp\left\{-\frac{1}{2}k^2\sigma_\mu^2\left|\hat{\mathbf{u}}'_\perp\right|^2\right\},\end{aligned} \tag{5.45}$$

from which one can obtain the spectral density at point $r\hat{\mathbf{u}}$ by

$$S^{(s)}(r\hat{\mathbf{u}}, \omega) = I\frac{2}{k^2 r^2}\frac{k^2\sigma_\mu^2}{2\pi}\int d^2\hat{\mathbf{u}}'_\perp \mathbf{P}_{11}^{(0)}\left(\hat{\mathbf{u}}\cdot\hat{\mathbf{u}}'\right)\exp\left\{-\frac{1}{2}k^2\sigma_\mu^2\left|\hat{\mathbf{u}}'_\perp\right|^2\right\}. \tag{5.46}$$

Here $\mathbf{P}_{11}^{(0)}$ has the same meaning as in the previous section, and the numerical results of the spectral degree of coherence will be presented in section 5.4.

5.2.6 Water Droplets and Ice Crystals

We apply the developed formalism to randomly oriented ice crystals. In general, the scattering amplitude matrix in Eq. (5.25) is no longer diagonal but is given by

$$\mathbf{S} = \begin{pmatrix} S_2 & S_3 \\ S_4 & S_1 \end{pmatrix} \tag{5.47}$$

Following the same procedure as in section 5.2.4, one can derive similar results to Eq. (5.40) and (5.42), with Eq. (5.42) modified to be

$$\mathbf{M}_{11} = \mathbf{P}_{11}^{(0)}, \tag{5.48a}$$

$$\mathbf{M}_{12} = \mathbf{P}_{11}^{(0)} \cos\left(2\left(i_1 + \phi'\right)\right) + \mathbf{P}_{13}^{(0)} \sin\left(2\left(i_1 + \phi'\right)\right), \tag{5.48b}$$

$$\begin{aligned} \mathbf{M}_{22} = &\left(\mathbf{P}_{11}^{(0)} \cos 2i_2 - \mathbf{P}_{32}^{(0)} \sin 2i_2\right) \cos\left(2\left(i_1 + \phi'\right)\right) \\ &- \left(\mathbf{P}_{33}^{(0)} \sin 2i_2 + \mathbf{P}_{23}^{(0)} \cos 2i_2\right) \sin\left(2\left(i_1 + \phi'\right)\right), \end{aligned} \tag{5.48c}$$

$$\begin{aligned} \mathbf{M}_{33} = &-\left(\mathbf{P}_{22}^{(0)} \sin 2i_2 + \mathbf{P}_{32}^{(0)} \cos 2i_2\right) \sin\left(2\left(i_1 + \phi'\right)\right) \\ &+ \left(\mathbf{P}_{33}^{(0)} \cos 2i_2 + \mathbf{P}_{23}^{(0)} \sin 2i_2\right) \cos\left(2\left(i_1 + \phi'\right)\right), \end{aligned} \tag{5.48d}$$

$$\mathbf{M}_{43} = \mathbf{P}_{43}^{(0)} \cos\left(2\left(i_1 + \phi'\right)\right) - \mathbf{P}_{42}^{(0)} \sin\left(2\left(i_1 + \phi'\right)\right), \tag{5.48e}$$

$$\mathbf{M}_{44} = \mathbf{P}_{44}^{(0)}. \tag{5.48f}$$

After orientation averaging, $\mathbf{P}^{(0)}$ becomes block-diagonal, which means the Mueller matrix elements $\mathbf{P}_{13}^{(0)}$, $\mathbf{P}_{23}^{(0)}$, $\mathbf{P}_{32}^{(0)}$, and $\mathbf{P}_{42}^{(0)}$ in the previous equation vanish. Therefore, we get the same formalism as for the sphere, except that $\mathbf{P}^{(0)}$ is the orientation averaged Mueller matrix in the fully coherent case.

As an application, we studied the coherence effects on light scattering by spherical water droplets and hexagonal ice crystals. Here, the coherent Mueller matrix for an ice

crystal was obtained by using the invariant imbedding T-matrix method [44]. The numerical results are presented in section 5.4.

5.3 DDA Simulation

We present a general numerical method to calculate the Mueller matrix of a particle of arbitrary shape and refractive index when the incident light is partially coherent. To link the numerical simulations to the analytical results in the previous section, we limit the incident beam to the Gaussian Schell-model beam with infinite width. Thus, the only free parameter of the incident beam is the coherence length. Moreover, the incident field can have an arbitrary polarization state because the Mueller matrix is independent of the CSDM at the source plane ($z = 0$). In the simulation, we choose to linearly polarize the incident field. After simplification, the electric field is essentially reduced to a scalar random field, and the second-order correlation matrix is reduced to a scalar function. The first step of the problem is to generate a 2D source that satisfies the required correlation function, and once the source is known, the field at any point in space can be obtained by propagating the source using the Green's function [26].

Several numerical methods are available, such as the random pulse method [46], random phase screens method [47], and shift-invariant filter method [48], but we use a more straightforward general method. As an example, let us consider the second-order correlation function on the $z = 0$ plane

$$\Gamma(\boldsymbol{\rho}_1, \boldsymbol{\rho}_2, \tau) = \langle U^*(\boldsymbol{\rho}_2, t+\tau) U(\boldsymbol{\rho}_1, t) \rangle = A(\boldsymbol{\rho}_1) A(\boldsymbol{\rho}_2) \mu(\boldsymbol{\rho}_2 - \boldsymbol{\rho}_1) \eta(\tau), \tag{5.49}$$

where $A(\boldsymbol{\rho})$ is the spatial profile, $\mu(\boldsymbol{\rho}_2 - \boldsymbol{\rho}_1)$ is the spatial degree of coherence, and $\eta(\tau)$ is the temporal degree of coherence. The goal is to express the random field $U(\boldsymbol{\rho}, t)$ as a

superposition of some random variables that have predefined correlation functions, i.e.

$$U(\boldsymbol{\rho},t)=A(\boldsymbol{\rho})\sum_{\mathbf{k}}\sum_{\omega}h_{\mu}(\mathbf{k})h_{\eta}(\omega)e^{i\mathbf{k}\cdot\boldsymbol{\rho}}e^{-i\omega t}I(k_x)I(k_y)I(\omega), \tag{5.50}$$

where $I(k_x)$, $I(k_y)$, and $I(\omega)$ are complex random numbers with correlation functions

$$\langle I^*(k_x)I^*(k_y)I^*(\omega)I(k_x')I(k_y')I(\omega')\rangle=\delta_{k_xk_x'}\delta_{k_yk_y'}\delta_{\omega\omega'}. \tag{5.51}$$

From Eq. (5.49), (5.50), and (5.51), one can obtain

$$\Gamma(\boldsymbol{\rho}_1,\boldsymbol{\rho}_2,\tau)=A(\boldsymbol{\rho}_1)A(\boldsymbol{\rho}_2)\sum_{\mathbf{k}}|h_{\mu}(\mathbf{k})|^2\,e^{i\mathbf{k}\cdot(\boldsymbol{\rho}_2-\boldsymbol{\rho}_1)}\sum_{\omega}|h_{\eta}(\omega)|^2\,e^{-i\omega t}, \tag{5.52}$$

which implies that

$$\sum_{\mathbf{k}}|h_{\mu}(\mathbf{k})|^2\,e^{i\mathbf{k}\cdot(\boldsymbol{\rho}_2-\boldsymbol{\rho}_1)}=\mu(\boldsymbol{\rho}_2-\boldsymbol{\rho}_1), \tag{5.53}$$

$$\sum_{\omega}|h_{\mu}(\omega)|^2\,e^{-i\omega\tau}=\eta(\tau). \tag{5.54}$$

Thus, the coefficients $h_{\mu}(\mathbf{k})$ and $h_{\eta}(\omega)$ in the random field $U(\boldsymbol{\rho},t)$ can be obtained by solving the above two equations.

For the monochromatic case, the correlation function is given by

$$\Gamma(\boldsymbol{\rho}_1,\boldsymbol{\rho}_2)=\exp\left(-\frac{(\boldsymbol{\rho}_1-\boldsymbol{\rho}_2)^2}{2\sigma_{\mu}^2}\right)=\mu(\boldsymbol{\rho}_1-\boldsymbol{\rho}_2). \tag{5.55}$$

and the random field is written as

$$U(\boldsymbol{\rho})=\sum_{\mathbf{k}}h_{\mu}(\mathbf{k})e^{i\mathbf{k}\cdot\boldsymbol{\rho}}I(k_x)I(k_y). \tag{5.56}$$

The coefficient $h_\mu(\mathbf{k})$ in Eq. (5.50) can be easily solved from Eq. (5.53). In the actual DDA simulation, the incident field $\mathbf{E}^{(i)}(\boldsymbol{\rho}, z, \omega)$ can be obtained directly from the above results, i.e.

$$\mathbf{E}^{(i)}(\boldsymbol{\rho}, z, \omega) = \sum_{|\mathbf{k}_\perp| \le k} h_\mu(\mathbf{k}_\perp) I(k_x) I(k_y) \exp\left(i \left(\mathbf{k}_\perp \cdot \boldsymbol{\rho} + \sqrt{k^2 - |\mathbf{k}_\perp|^2} z \right) \right) \mathbf{e}^{(i)}, \tag{5.57}$$

where $\mathbf{e}^{(i)}$ is a unit vector denoting the polarization of the incident field. For a specific realization of the random field, one can get the scattering amplitude matrix and corresponding Mueller matrix in the direction . After averaging over the ensemble of the incident fields, one can get the Mueller matrix for a sphere. Numeric results are discussed in the section 5.4.

5.4 Results

We applied the analytical formalism to calculate the Mueller matrix of a sphere when the incident light is partially coherent. The results are shown in Fig. 5.3. The sphere has a refractive index of $n = 1.5$ and a radius of $a = \lambda$, where λ is the wavelength of the incident light. The coherence length σ_μ has values from λ to 10λ. Note that P_{11} is essentially the intensity reported in [2, 29] based on a scalar incident field and similar conclusions were reached. One of the most important conclusions is that the phase function tends to be more isotropic as the incident field becomes less coherent and gradually approaches the coherent case as the coherence length increases. Other Mueller matrix elements also become more isotropic as coherence deteriorates. Moreover, the reduced Mueller matrix elements P_{22}/P_{11}, P_{33}/P_{11}, and P_{44}/P_{11} in the backward direction are much more sensitive to the coherence length than those in the forward direction, and can be explained by the fact that interference in the forward direction is more robust to random phases than that in the backward direction.

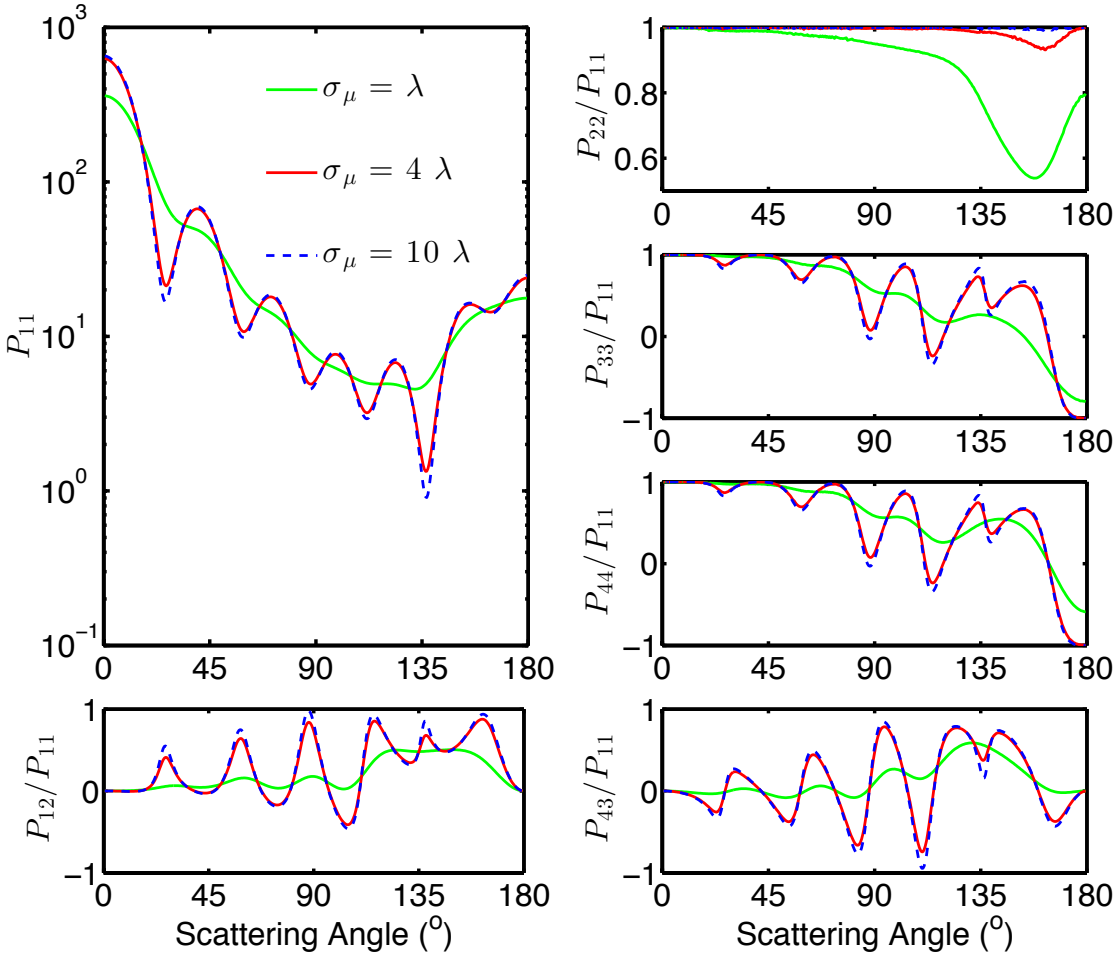

Figure 5.3: Mueller matrix elements for a sphere of radius $a = \lambda$ and refractive index $n = 1.5$. The coherence length σ_μ has values of λ, 4λ, and 10λ.

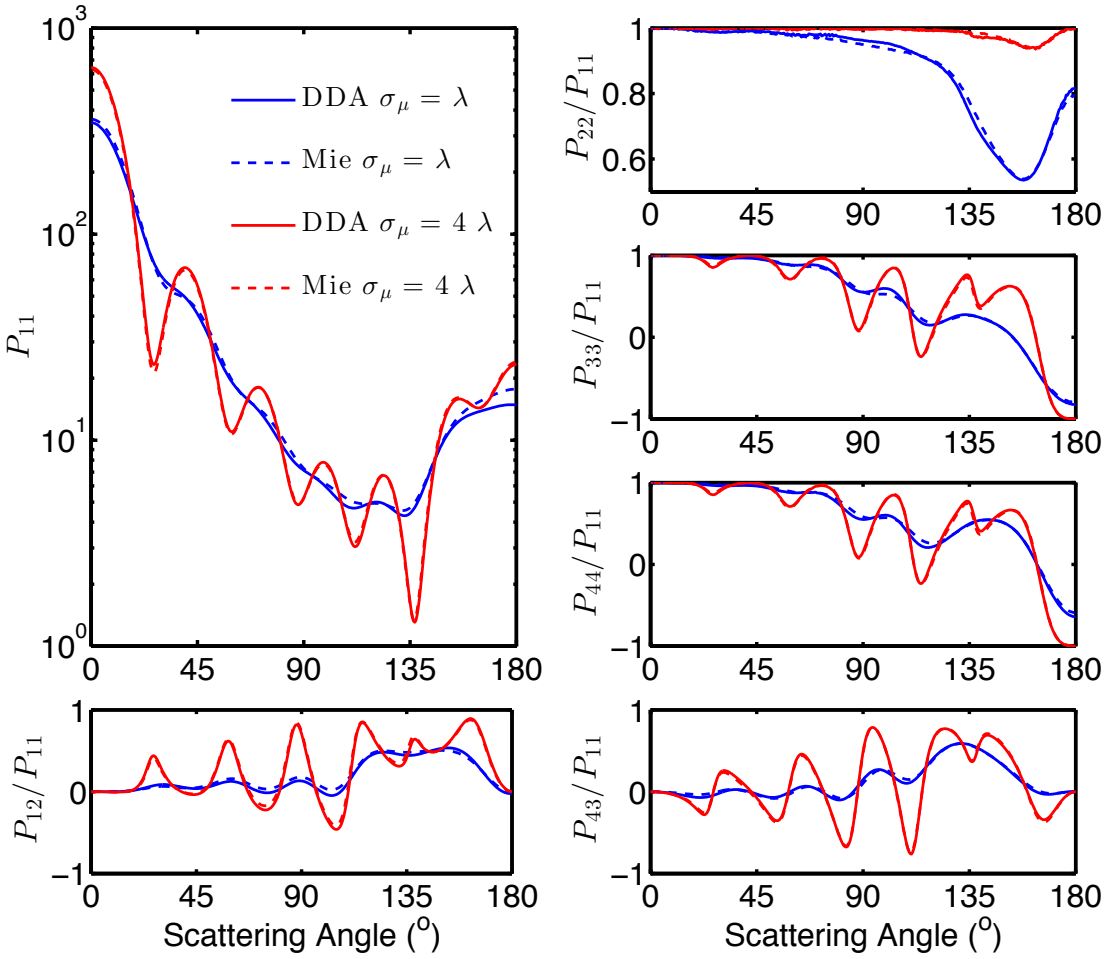

Figure 5.4: Comparison of Mueller matrix elements computed from DDA and Mie methods. Two cases, $\sigma_\mu = \lambda$ and 4λ are simulated. The remaining parameters are the same as Fig. 5.3.

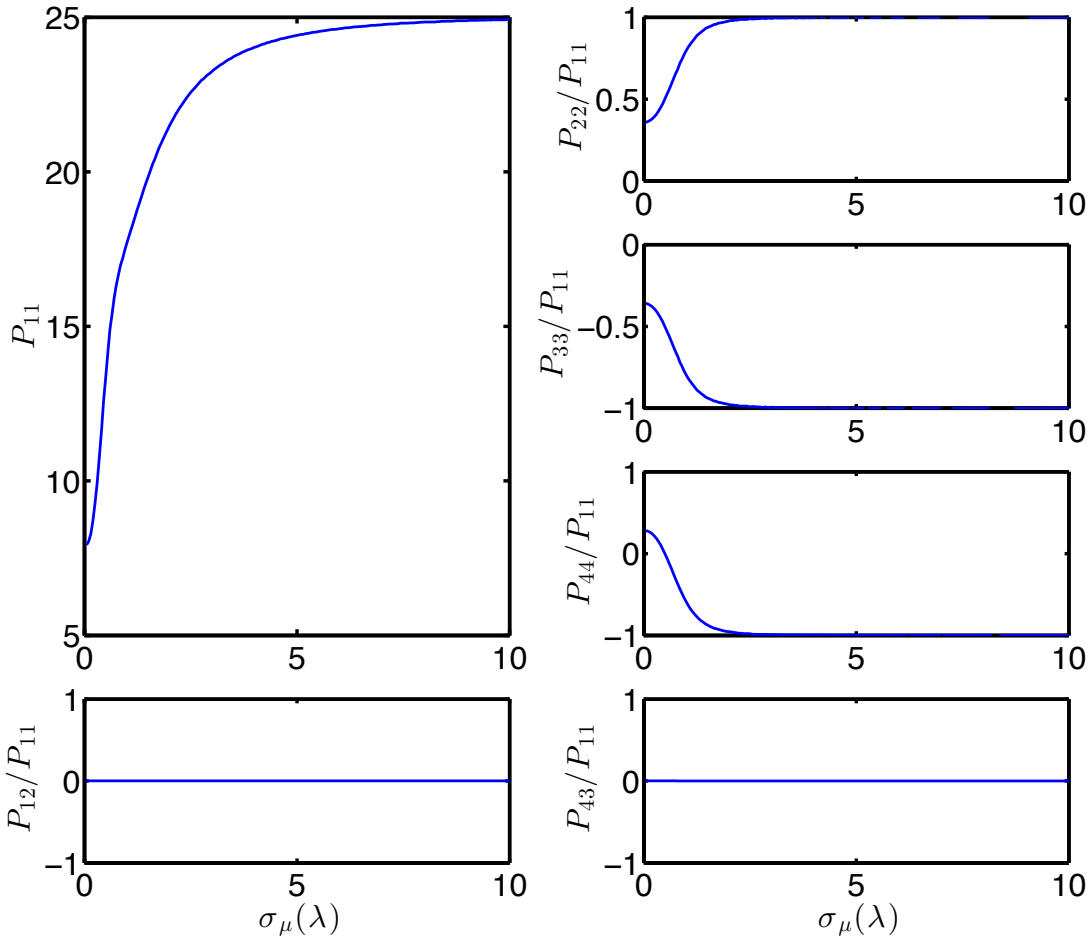

Figure 5.5: Mueller matrix elements for a sphere in the backward direction ($180°$). The coherence length $\sigma_\mu = \lambda$ is from 0 to 10λ. The remaining parameters are the same as Fig. 5.3.

To validate the formalism we derived, we compared the analytical results with DDA simulations. The comparisons of Mueller matrix elements are shown in Fig. 5.4. The sphere has the same parameters as before and two cases, $\sigma_\mu = \lambda$ and 4λ, are computed. In the DDA simulations, 160 plane wave components are used to construct the incident field, a total of 1000 ensemble averages are taken, and the inter-dipole spacing used is $d \sim \lambda/20$. The results show that DDA simulations agree very well with the analytical formalism.

We investigated the Mueller matrix elements in the backward direction ($180°$ degree

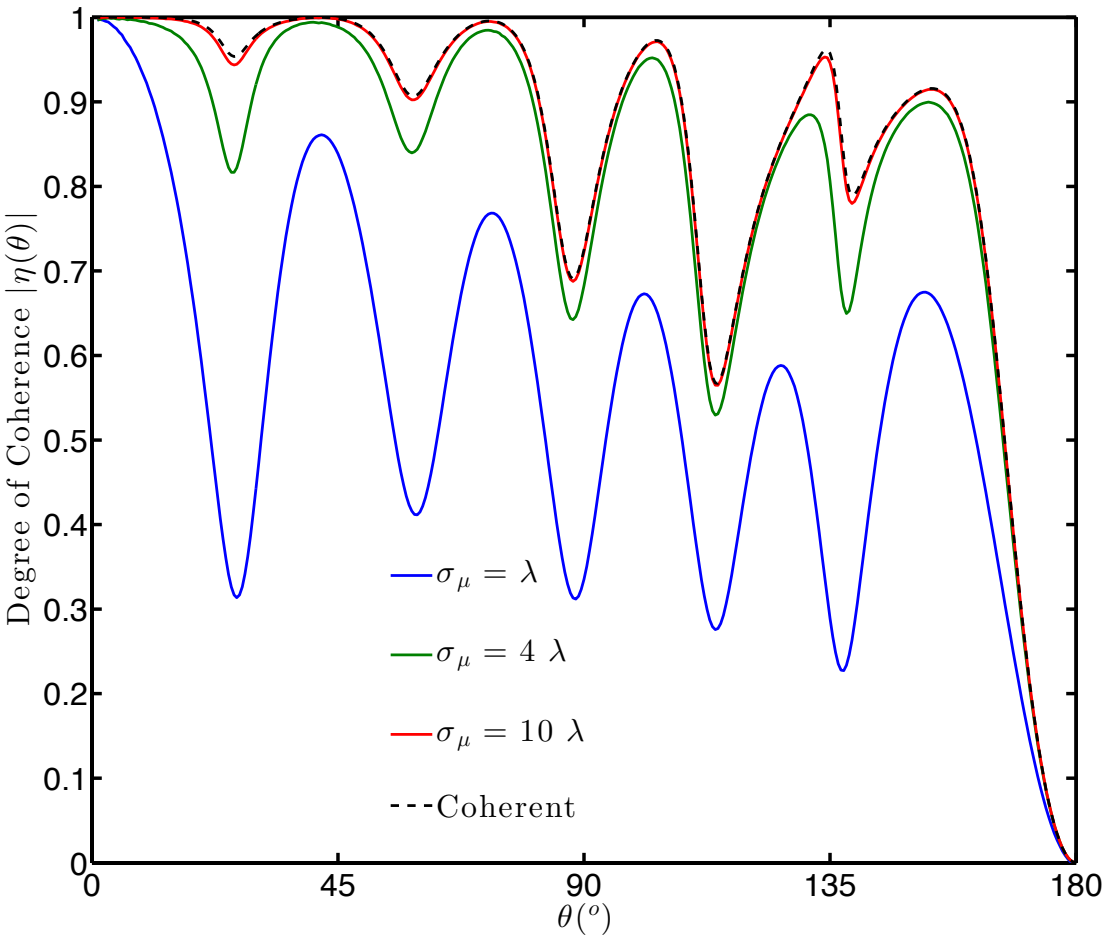

Figure 5.6: The spectral degree of coherence of the scattered field from a sphere. θ is the angle between scattering direction and the $+z$ direction. Four cases, including the coherent case are simulated. The parameters are the same as Fig. 5.3.

scattering). The sphere has the same parameters as before, and the coherence length is chosen from 0 to 10λ. As can be seen from Fig. 5.5, for Mueller matrix elements P_{12}/P_{11} and P_{43}/P_{11}, no significant dependence on coherence length is observed. In comparison, other Mueller matrix elements all change monotonically and gradually plateau as the coherence length increases. Evidently, all approach the coherent values when the coherence length reaches a large enough value.

In addition, we computed the spectral degree of coherence of the scattered field. The

results are shown in Fig. 5.6, where the sphere has the same parameters as previously and the coherence length is chosen from λ to 10λ. Here, the spectral degree of coherence is defined as the correlation between two directions, the $+z$ and the polar angle θ. We find that at any angle, the normal of the degree of coherence always decreases as the incident light becomes less coherent. Note that $|\eta|$ is not always unity even when the coherence length approaches infinity due to the completely unpolarized special form of the incident beam. A simple calculation gives the degree of coherence when the coherence length is infinitely large

$$|\eta(\theta_1,\theta_2)| = \frac{|S_2^*(\theta_1)S_2(\theta_2) + S_1^*(\theta_1)S_1(\theta_2)|}{\sqrt{|S_1(\theta_1)|^2 + |S_2(\theta_1)|^2}\sqrt{|S_1(\theta_2)|^2 + |S_2(\theta_2)|^2}}, \tag{5.58}$$

where S_1 and S_2 are defined in Eq. (5.25). It can be shown that Eq. (5.58) is not always equal to unity.

As applications of the formalism developed, we computed the Mueller matrix elements for water droplets and hexagonal ice crystals that are the constituents of atmospheric clouds. The results for a water droplet are shown in Fig. 5.7. The water droplet has a size parameter $x = 80$ and a refractive index $n = 1.33$. The coherence length parameter $k\sigma_\mu$ has values from 5 to 100. Apart from similar conclusions to the case of a small sphere, we found that both the corona and glory phenomena will be eliminated as the incident field becomes incoherent. Since both are consequences of interference, which can be extinguished by the introduction of incoherence, the elimination is reasonable. The results for the hexagonal ice crystal are shown in Fig. 5.8. The ice crystal has a size parameter $kL = 2ka = 150$, where L is the height and a is the semi-width, and a refractive index $n = 1.31$. The coherence length parameter $k\sigma_\mu$ has the values 5, 10, and 100. The results show that both the 22° and 46° halos gradually disappear as the coherence length decreases, the same explanation also holds for corona and glory for water droplets. The

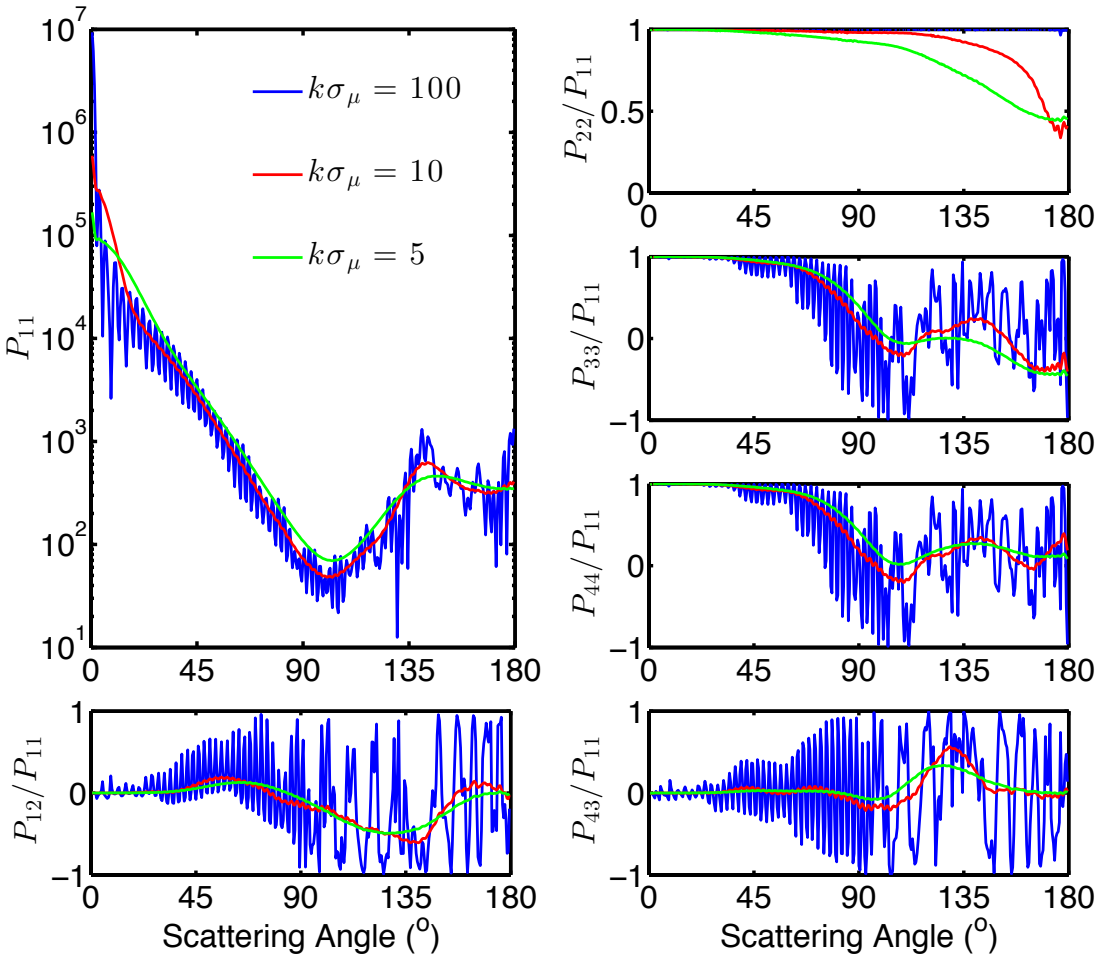

Figure 5.7: Mueller matrix elements for a water droplet of size parameter $x = 80$ and refractive index $n = 1.33$. The coherence length parameter σ_μ has values of 5, 10 and 100.

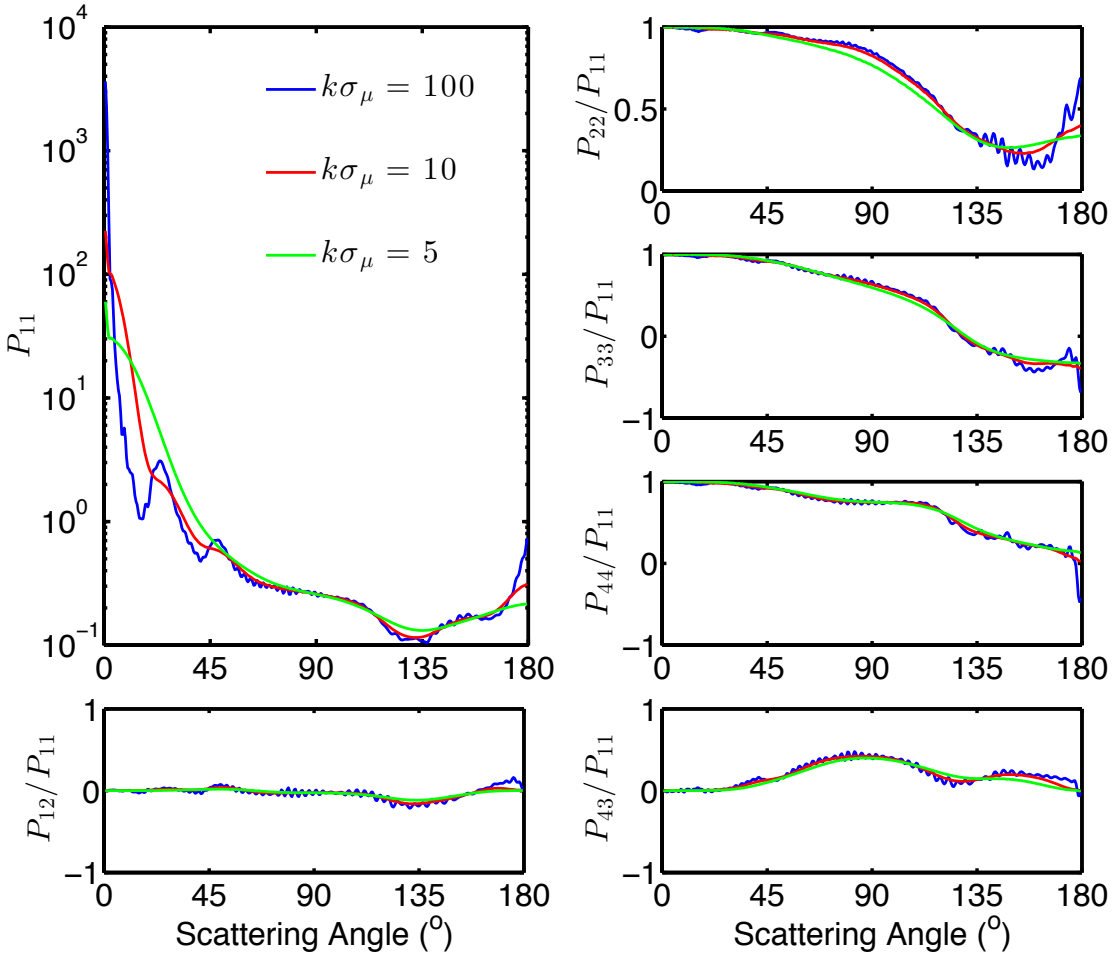

Figure 5.8: Mueller matrix elements for a hexagonal ice crystal with size parameter $kL = 2ka = 150$, where L is the height and a is the semi-width, and refractive index $n = 1.31$. The coherence length parameter $k\sigma_\mu$ has values of 5, 10 and 100.

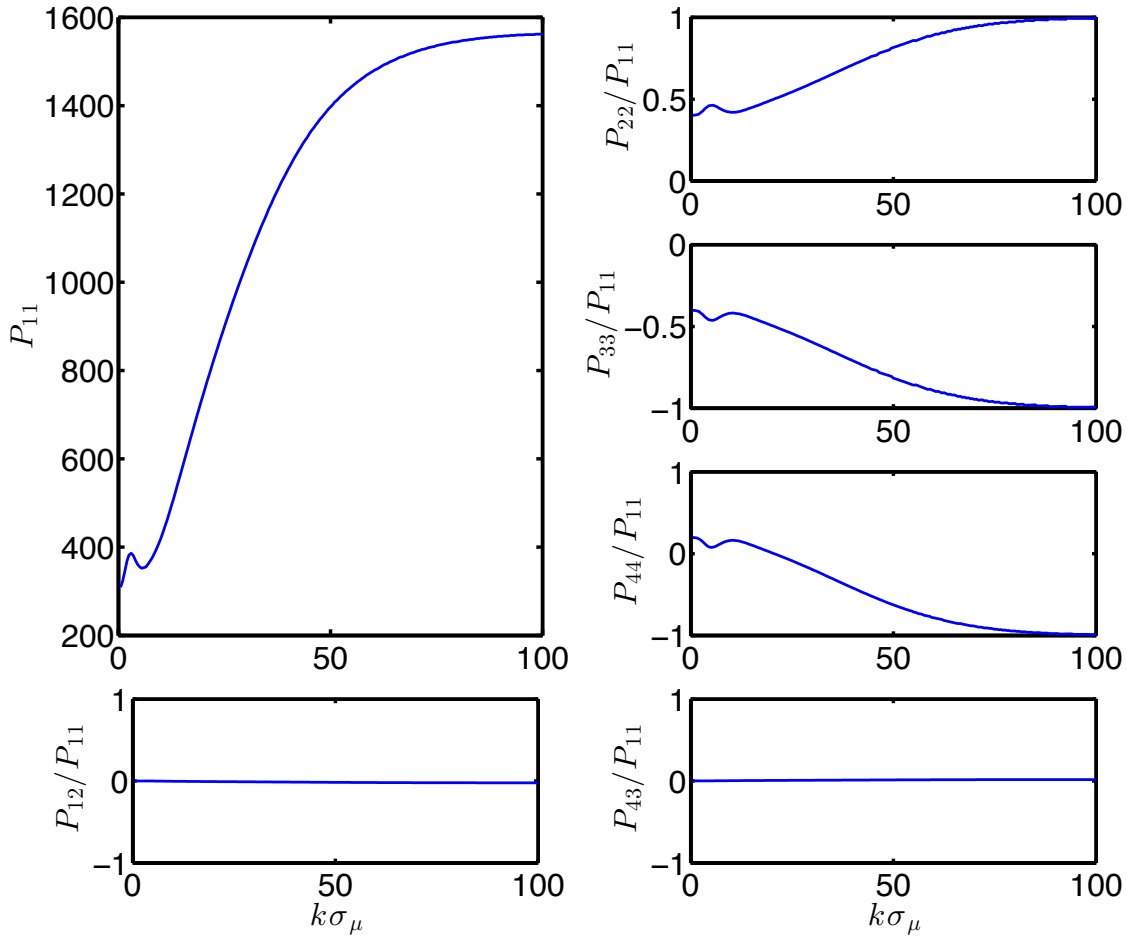

Figure 5.9: Mueller matrix elements for a water droplet in the backward direction ($180°$). The coherence length parameter $k\sigma_\mu$ is from 0 to 100. The size parameter of the water droplet is $x = 80$ and the refractive index is $n = 1.33$.

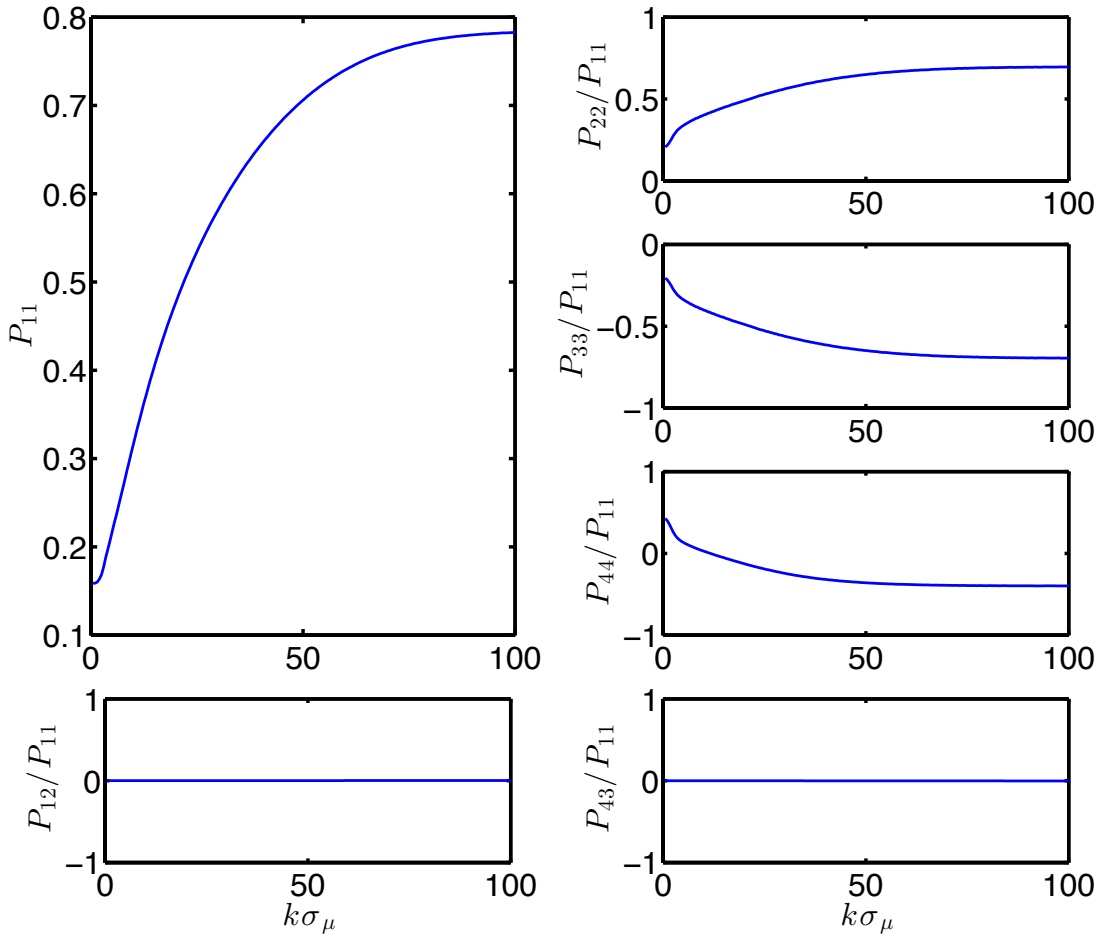

Figure 5.10: Mueller matrix elements for a hexagonal ice crystal in the backward direction (180°). The coherence length parameter $k\sigma_\mu$ is from 0 to 100. The remaining parameters are the same as Fig. 5.8.

Mueller matrix elements for the water droplet and ice crystal in the backward direction are shown in Fig. 5.9 and Fig. 5.10, respectively. We found similar results to those of small spheres.

5.5 Conclusions and Discussions

The conventional Lorenz-Mie formalism is generalized to the case when the incident light is partially coherent. For the Gaussian Schell-model beams, the Mueller matrix and spectral degree of coherence for the scattered field is derived analytically and the formalism is validated by DDA simulation. The Results suggest that the reduced Mueller matrix elements P_{22}/P_{11}, P_{33}/P_{11}, and P_{44}/P_{11} in the backward direction strongly depend on the degree of coherence of the incident light. The same formalism is applied to randomly orientated water droplets and hexagonal ice crystals. We find that the corona and glory phenomena associated with water droplets and halos with hexagonal ice crystals disappear if the incident light is highly incoherent.

The relevance of these results to atmospheric radiation is three-fold. First, despite the fact that the solar source is completely incoherent, which is presumably thermal emission, the sunlight reaching the surface of the earth acquires a certain degree of correlation through the process of propagation. This is a straightforward result of the van Cittert-Zernike theorem [49, 50], and a rough estimation reveals that the sunlight has a spatial coherence length of about 60 μm [26]. Given the size of large atmospheric particles, the finite coherence length of sunlight will have observable effects on the pattern of the scattered field. Second, when using a laser beam instead of natural solar light in remote sensing, the light beam becomes partially coherent when passing through atmospheric turbulence. Therefore, it is of practical interest to investigate the effect of spatial coherence in light scattering. Third, even though there is not a variant of the radiative transfer equation in which the scattering matrix derived in this paper can be inserted, the results obtained

here shed light on what results can be expected in a multiple scattering situation. As it is shown here, all Mueller matrix elements become smoother as the coherence of incident light deteriorates, one would naturally expect the same thing to happen in a multiple scattering system. As a matter of fact, the effect of spatial coherence on scattering from an optically inhomogeneous medium was studied by Sukhov *et al.* [43], and they found that the spread of the scattered intensities are more limited when the incident light is incoherent when compared with the fully coherent case.

Thus our results provide a potential method to determine coherence length and for possible applications in atmospheric remote sensing.

6. EFFECTS OF INCOHERENCE ON PARTICLE CHARACTERIZATION USING DIGITAL HOLOGRAPHIC MICROSCOPY

Digital holography microscopy has proven to be efficient and accurate in characterizing and tracking colloidal particles. It has shown to be able measure the radius and refractive index with 1% accuracy and the three-dimensional position with nanometer resolution in real time. To create high contrast holograms, the illumination normally used is a coherent laser beam. Using partially coherent illumination, we are able to take into consideration the effects of incoherence due to light source fluctuations and medium turbulence that the particle is subjected to. We computed holograms at different degrees of coherence using Gaussian Schell-model beams, showing reduced contrast when the coherence of illumination deteriorates. By fitting the obtained holograms to coherent Lorenz-Mie theory, the retrieved parameters of the particles show that holography is rather robust against incoherence. We also demonstrate the possibility of retrieving coherence length based on partially coherent Lorenz-Mie theory.

6.1 Introduction

Digital holography microscopy (DHM) has been successfully used to characterize and track colloidal particles [3, 30]. By fitting the recorded hologram to the full Lorenz-Mie theory, the parameters of the particle such as the particle size, refractive index and three-dimensional position, can be retrieved with high accuracy and efficiency [3]. One of the assumptions in the theory is that the laser beam used is fully coherent; however, the question that naturally arises is how coherent does the light need to be before the method becomes untenable [25, 26, 24]? Historically, a partially coherent light beam was utilized in holography to reduce speckle due to high coherence [51]. Holography using partially coherent illumination was also investigated theoretically by Kozacki et al. [52, 53], and

reduced resolution was reported. More recently, it was demonstrated experimentally by Gopinathan et al. [54] that reducing the coherence of light could broaden the impulse response in DHM. However, the effects of incoherence in particle characterization using DHM have never been considered in the literature.

Based on the incoherent Lorenz-Mie theory by Liu et al. [55], we computed the holograms produced by homogenous colloidal particles at various degrees of coherence when using Gaussian Schell-model beams [26]. The obtained holograms are then put into a similar fitting algorithm used by Lee et al. [3], who treated the illumination as a fully coherent plane wave. It turns out that the retrieval algorithm is rather robust against incoherence, with retrieved parameters relatively insensitive to the coherence length of the illumination. We found that when the illumination has wavelength 632 nm, as long as the coherence length is at least 2 μm, the retrieved parameters are indistinguishable from those in the fully coherent case, which partially explains the reason why holographic microscopy offers such high precision in particle characterization and tracking.

We also modified the fitting algorithm to incorporate the incoherence effects when calculating the holograms, which enables us to retrieve the coherence length of the illumination from an input hologram. Even though the algorithm becomes less efficient when compared with fitting to the standard Lorenz-Mie theory, it does provide an accurate estimation of the coherence length, especially when it is comparable to the wavelength.

6.2 Theory

In this work, we consider a similar holographic setup used in [3, 56], except that the illumination is replaced by a Gaussian Shell-model beam. We denote z_0 as the distance between the plane that contains the light source and the plane that contains the particle, and z_p as the distance between the particle plane and the hologram plane at which the interference pattern is recorded by a digital camera. The laser beam also passes through

a microscope before being registered, and therefore, the hologram is magnified with a magnification ratio determined by the specific instrument.

A monochromatic and partially coherent beam propagating in the $\hat{z}$ direction can be written using the angular spectrum representation [26]

$$\mathbf{E}^{(i)}(\boldsymbol{\rho}, z, \omega) = \int_{\left|\hat{\mathbf{u}}'_\perp\right| \leq 1} \mathbf{e}^{(i)}\left(\hat{\mathbf{u}}'_\perp, \omega\right) \exp\left(ik\left(\hat{\mathbf{u}}'_\perp \cdot \boldsymbol{\rho} + u'_z(z - z_0)\right)\right) d^2\hat{\mathbf{u}}'_\perp, \tag{6.1}$$

where the notations have the same meanings as those in Eq. (5.5), except that the three-dimensional coordinate $\mathbf{r}$ in Eq. (5.5) is now expressed as $(\boldsymbol{\rho}, z)$.

In the far field region, the scattered field from a homogenous sphere was obtained similarly as Eq. (5.33)

$$\mathbf{E}^{(s)}\left(r\hat{\mathbf{u}}, \omega\right) = \frac{\exp(ikr)}{-ikr} \int \mathbf{A}\left(\hat{\mathbf{u}}, \hat{\mathbf{u}}'\right) \cdot \mathbf{e}^{(i)}\left(\hat{\mathbf{u}}'_\perp, \omega\right) e^{-iku'_z z_0} d^2\mathbf{u}'_\perp, \tag{6.2}$$

where we used the fact that

$$r\hat{\mathbf{u}} = (\boldsymbol{\rho}, z). \tag{6.3}$$

Note that there is an extra phase factor $e^{-iku'_z z_0}$ compared with Eq. (5.33). The total field is then

$$\mathbf{E}^{(r)}\left(r\hat{\mathbf{u}}, \omega\right) = \int d^2\hat{\mathbf{u}}'_\perp e^{-iku'_z z_0} \left[\frac{e^{ikr}}{-ikr} \mathbf{A}\left(\hat{\mathbf{u}}, \hat{\mathbf{u}}'\right) + e^{ikr\hat{\mathbf{u}}'\cdot\hat{\mathbf{u}}}\right] \mathbf{e}^{(i)}\left(\hat{\mathbf{u}}'_\perp, \omega\right), \tag{6.4}$$

from which the cross-spectral density matrix (CSDM) can be calculated using Eq. (5.2)

and the result reads

$$\mathbf{W}(r\hat{\mathbf{u}}, r\hat{\mathbf{u}}, \omega) = \int d^2\hat{\mathbf{u}}'_\perp d^2\hat{\mathbf{u}}''_\perp e^{ik_z(u'_z - u''_z)z_0} \left\{ \frac{1}{k^2 r^2} \mathbf{A}^* \left(\hat{\mathbf{u}}, \hat{\mathbf{u}}'\right) \cdot \tilde{\mathbf{W}}^{(i)} \left(\hat{\mathbf{u}}'_\perp, \hat{\mathbf{u}}''_\perp, \omega\right) \right.$$
$$\cdot \mathbf{A}^T \left(\hat{\mathbf{u}}, \hat{\mathbf{u}}''\right) + e^{-ikr(\hat{\mathbf{u}}' - \hat{\mathbf{u}}'')\cdot\hat{\mathbf{u}}} \tilde{\mathbf{W}}^{(i)} \left(\hat{\mathbf{u}}'_\perp, \hat{\mathbf{u}}''_\perp, \omega\right) - \frac{e^{-ikr}}{-ikr} e^{ikr\hat{\mathbf{u}}''\cdot\hat{\mathbf{u}}} \mathbf{A}^* \left(\hat{\mathbf{u}}, \hat{\mathbf{u}}'\right)$$
$$\left. \cdot \tilde{\mathbf{W}}^{(i)} \left(\hat{\mathbf{u}}'_\perp, \hat{\mathbf{u}}''_\perp, \omega\right) + \frac{e^{-ikr}}{-ikr} e^{ikr\hat{\mathbf{u}}'\cdot\hat{\mathbf{u}}} \tilde{\mathbf{W}}^{(i)} \left(\hat{\mathbf{u}}'_\perp, \hat{\mathbf{u}}''_\perp, \omega\right) \cdot \mathbf{A}^T \left(\hat{\mathbf{u}}, \hat{\mathbf{u}}'\right) \right\}. \tag{6.5}$$

Here $\tilde{\mathbf{W}}^{(i)} \left(\hat{\mathbf{u}}'_\perp, \hat{\mathbf{u}}''_\perp, \omega\right)$ is the angular correlation matrix defined in Eq. (5.9). Without loss of generality, we restrict ourselves to a specific class of partially coherent beams, the Gaussian Schell-model beams, which have the following CSDM at the source plane

$$\mathbf{W}^{(i)}_{lm}(\boldsymbol{\rho}_1, \boldsymbol{\rho}_2, \omega) = a_l a_m b_{lm} \exp\left(-\frac{\boldsymbol{\rho}_1^2 + \boldsymbol{\rho}_2^2}{4\sigma_S^2}\right) \exp\left(-\frac{(\boldsymbol{\rho}_1 - \boldsymbol{\rho}_2)^2}{2\sigma_\mu^2}\right), \tag{6.6}$$

The parameter σ_S can be interpreted as the width of the beam, σ_μ as the coherence length, and the remaining parameters in Eq. (6.6) determine the polarization of the beam. Furthermore, we take the same limit as Ref. [55] by letting the width of the beam go to infinity, which leads to

$$\mathbf{W}^{(i)}_{lm}(\boldsymbol{\rho}, \boldsymbol{\rho}, \omega) = a_l a_m b_{lm}, \tag{6.7}$$

$$\begin{aligned} \tilde{\mathbf{W}}^{(i)} \left(\hat{\mathbf{u}}'_\perp, \hat{\mathbf{u}}''_\perp, \omega\right) &= a_l a_m b_{lm} \frac{k^2\sigma_\mu^2}{2\pi} \exp\left(-\frac{1}{2}k^2\sigma_\mu^2 \left|\hat{\mathbf{u}}'_\perp\right|^2\right) \delta^{(2)}\left(\hat{\mathbf{u}}'_\perp - \hat{\mathbf{u}}''_\perp\right) \\ &= \mathbf{W}^{(i)}_{lm}(z = z_0) \frac{k^2\sigma_\mu^2}{2\pi} \exp\left(-\frac{1}{2}k^2\sigma_\mu^2 \left|\hat{\mathbf{u}}'_\perp\right|^2\right) \delta^{(2)}\left(\hat{\mathbf{u}}'_\perp - \hat{\mathbf{u}}''_\perp\right), \end{aligned} \tag{6.8}$$

where $\mathbf{W}^{(i)}_{lm}(z = z_0)$ is the polarization matrix of the incident light at the source plane

[26]. Substituting the above equations into Eq. (6.5), we arrive at

$$\begin{aligned}\mathbf{W}\left(r\hat{\mathbf{u}}, r\hat{\mathbf{u}}, \omega\right) &= \frac{k^2\sigma_\mu^2}{2\pi}\int d^2\hat{\mathbf{u}}'_\perp \exp\left(-\frac{1}{2}k^2\sigma_\mu^2\left|\hat{\mathbf{u}}'_\perp\right|^2\right)\Big\{\mathbf{W}^{(i)}(z=z_0) \\ &+\frac{1}{k^2r^2}\cdot\mathbf{W}^{(i)}(z=z_0)\cdot\mathbf{A}^T\left(\hat{\mathbf{u}},\hat{\mathbf{u}}'\right) \\ &-\frac{1}{kr}(ie^{-i\alpha}\mathbf{A}^*\left(\hat{\mathbf{u}},\hat{\mathbf{u}}'\right)\cdot\mathbf{W}^{(i)}(z=z_0) \\ &-ie^{i\alpha}\mathbf{W}^{(i)}(z=z_0)\cdot\mathbf{A}^T\left(\hat{\mathbf{u}},\hat{\mathbf{u}}'\right)\,)\Big\}, \end{aligned} \tag{6.9}$$

where $\alpha = kr\left(1-\hat{\mathbf{u}}'\cdot\hat{\mathbf{u}}\right)$.

The interference pattern recorded by the camera is determined by the intensity of the total field

$$I(\rho) = \mathrm{Tr}\mathbf{W}\left(r\hat{\mathbf{u}}, r\hat{\mathbf{u}}, \omega\right)\Big|_{z=z_p}, \tag{6.10}$$

with z_p being the distance between the particle plane and the hologram plane. We consider a linearly polarized illumination, which has a simple polarization matrix at the source plane

$$\mathbf{W}^{(i)}(z=z_0) = \begin{pmatrix} 1 & 0 \\ 0 & 0 \end{pmatrix}. \tag{6.11}$$

Eq. (6.10) can be then explicitly written as

$$\begin{aligned} I(\rho) &= \frac{k^2\sigma_\mu^2}{2\pi}\int d^2\hat{\mathbf{u}}'_\perp \exp\left(-\frac{1}{2}k^2\sigma_\mu^2\left|\hat{\mathbf{u}}'_\perp\right|^2\right)\Big\{1+\frac{1}{k^2r^2}\left(|\mathbf{A}_{11}|^2+|\mathbf{A}_{21}|^2\right) \\ &-\frac{2}{kr}\mathrm{Re}\left(ie^{-i\alpha}\mathbf{A}^*_{11}\right)\Big\}. \end{aligned} \tag{6.12}$$

Note that after a series of assumptions and simplifications, the effects of finite coherence are reduced to a single parameter $k\sigma_\mu$. As mentioned in Ref. [3], the hologram can be normalized by the background when the particle is absent. In this case, the background

hologram is simply

$$\begin{aligned} I_0(\rho) &= \mathrm{Tr}\mathbf{W}_0\left(r\hat{\mathbf{u}}, r\hat{\mathbf{u}}, \omega\right)\Big|_{z=z_p} \\ &= \frac{k^2\sigma_\mu^2}{2\pi}\int d^2\hat{\mathbf{u}}'_\perp \exp\left(-\frac{1}{2}k^2\sigma_\mu^2\left|\hat{\mathbf{u}}'_\perp\right|^2\right)\mathrm{Tr}\mathbf{W}^{(i)}(z=z_0) \\ &= 1. \end{aligned} \tag{6.13}$$

Therefore, we have the normalized hologram

$$B(\rho) = \frac{I(\rho)}{I_0(\rho)} = I(\rho). \tag{6.14}$$

Compared with the radial profile obtained in Ref. [3](Eq. (3)), the above equation has one more free parameter σ_μ, apart from the particle size a_p, the three-dimensional position r_p and the refractive index n_p.

Measured holograms are then fitted to Eq. (6.14) using the Levenberg-Marquardt nonlinear least-squares minimization algorithm [57]. Once the properties of the particle are all known, this method effectively retrieves the coherence length of the illumination.

6.3 Numerical results

Following the experimental setup used in Ref. [3], the He-Ne laser beam with wavelength $\lambda = 0.632\ \mu m$ was utilized. We also chose the medium that the particle is immersed in to be pure water, which has refractive index $n_m = 1.3326$ at temperature 25 °C for $\lambda = 0.632\ \mu m$.

As an application of the theoretical formalism we derived in the last section, we first computed the holograms and their corresponding radial profiles at various coherence lengths. It is shown (Fig. 6.1 and Fig. 6.2) that reducing coherence length leads to a smoother radial profile, and the radial profile gradually converges as the coherence length

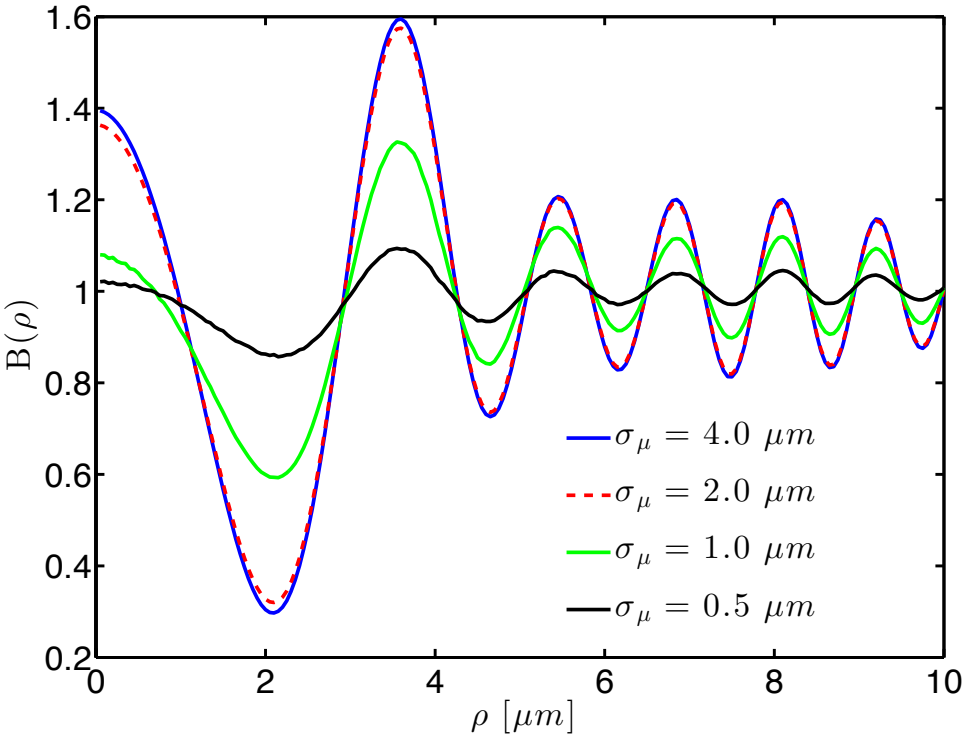

Figure 6.1: The radial profiles at various coherence lengths. The particle has radius $a = 1$ μm, refractive index $n = 1.55$ and axial position $z_p = 20$ μm.

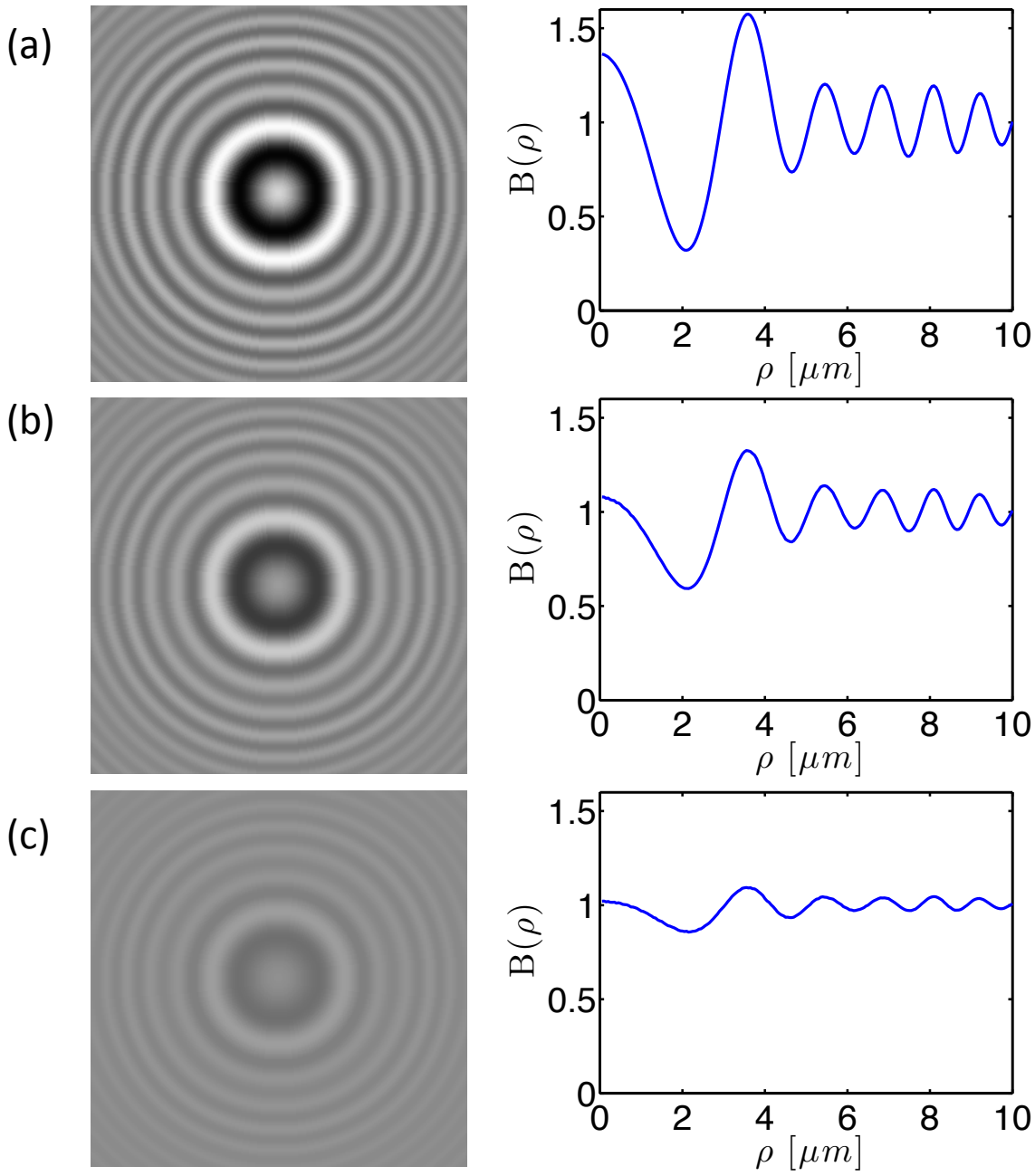

Figure 6.2: Holograms and their corresponding radial profiles. (a) $\sigma_\mu = 2\ \mu m$, (b)$\sigma_\mu = 1\ \mu m$, (c)$\sigma_\mu = 0.5\ \mu m$. The rest of the parameters are the same as Fig. 6.1.

increases, approaching the fully coherent case. While the contrast of the hologram varies as the coherence changes, the positions of both minima and maxima remain invariant. Four different coherence lengths, 0.5, 1.0, 2.0 and 4.0 μm, are considered. The particle size is fixed at $a_p = 1.0\ \mu m$ and refractive index $n_p = 1.55$. The particle position is chosen in such a way that the camera lies in the far field region with $z_p = 20\ \mu m$.

Table 6.1: Retrieved coherence lengths compared with correct values. The parameters are the same as Fig. 6.1.

Correct value [μm]	Initial guess [μm]	Retrieved value [μm]
5.0	2.0	4.65
4.0	2.0	4.00
3.0	3.0	3.00
2.0	1.0	2.00
0.5	1.0	0.50

We then use the generated holograms as inputs in the fitting algorithm based on Eq. (6.14), attempting to retrieve the properties of the particle together with the degree of coherence of the illumination. With initial guesses chosen sufficiently close to the final solution, which can be achieved by imposing a constraint on each parameter, the algorithm is able to obtain the correct parameters iteratively. Here we focus on retrieving the coherence length from a given hologram while fixing the rest of the parameters. As shown in Table. 6.1, the algorithm correctly produces all coherence lengths up to 4 μm. The failure at 5 μm is attributed to the fact that all holograms are nearly identical when the coherence length exceeds 4 μm.

We also investigated the effects of incoherence on particle characterization using holographic microscopy. Instead of fitting measured holograms to Eq. (6.14), holograms computed at different degrees of coherence are fitted using the conventional Lorenz-Mie theory

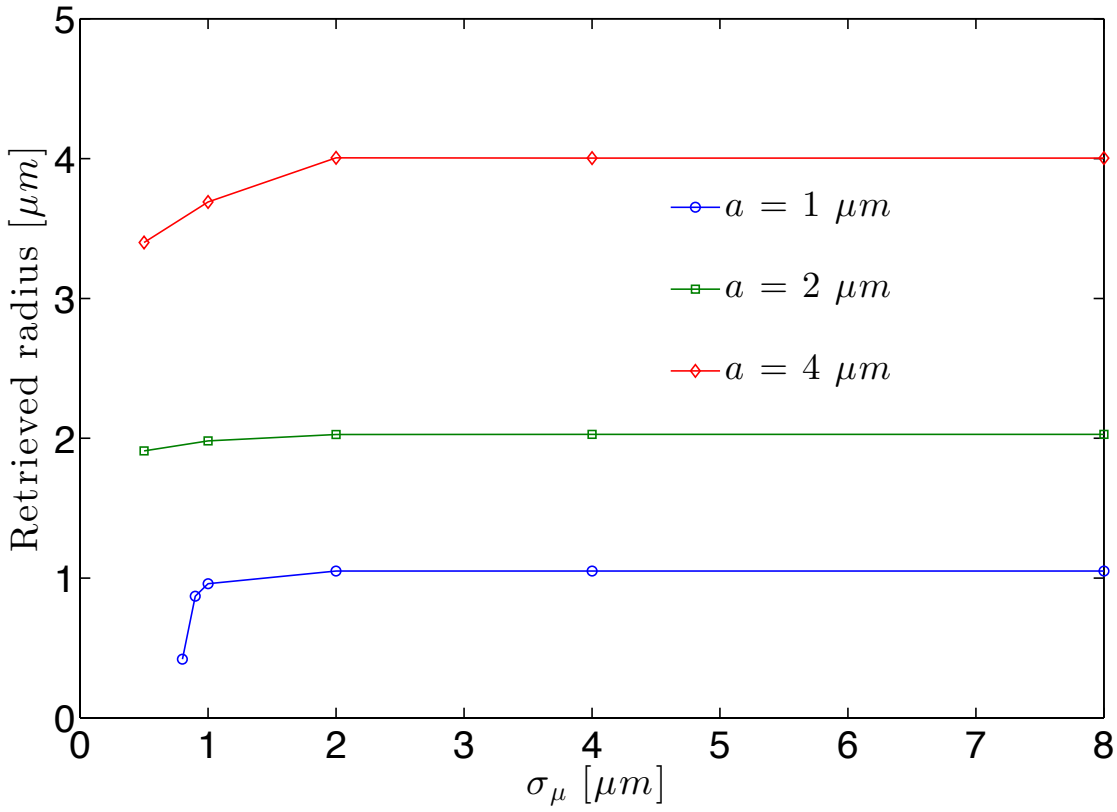

Figure 6.3: Retrieved radii at different coherence lengths. Three cases are considered, a = 1, 2 and 4 μm. The particle has fixed refractive index $n_p = 1.55$ and axial position $z_p = 20$ μm.

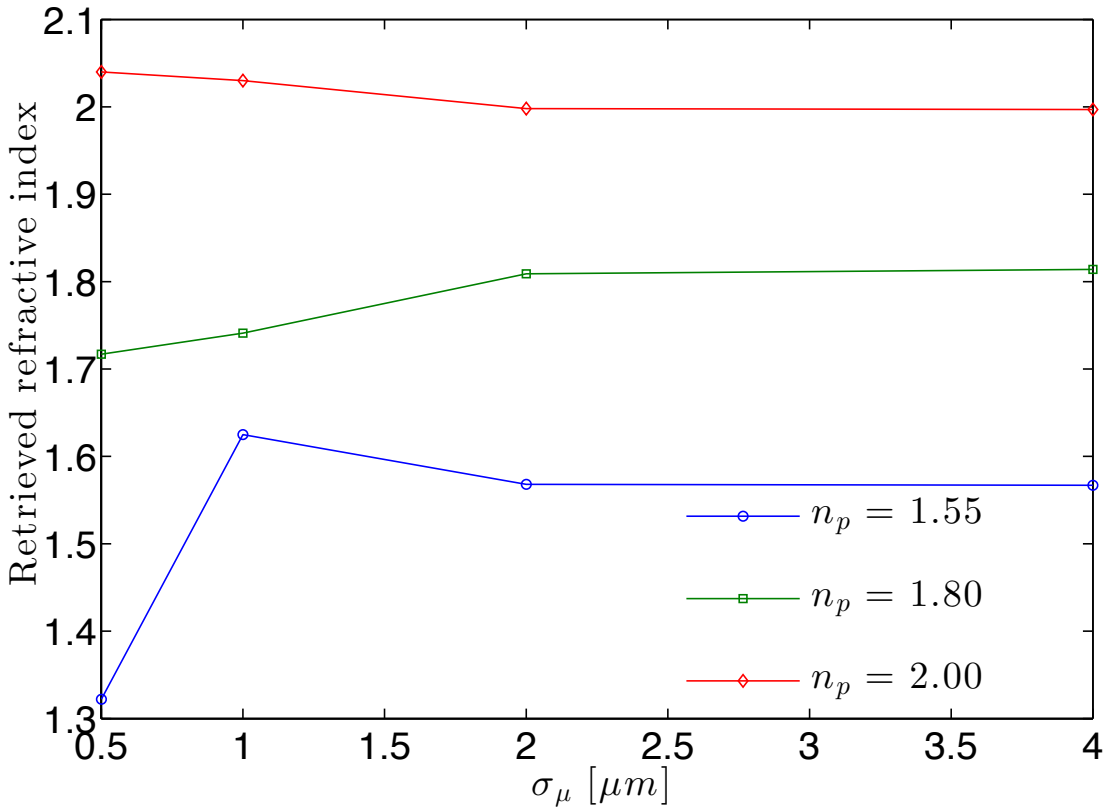

Figure 6.4: Retrieved refractive indices at different coherence lengths. Three cases are considered, n_p = 1.55, 1.80 and 2.00. The particle has fixed radius $a_p = 1\ \mu m$ and axial position $z_p = 40\ \mu m$.

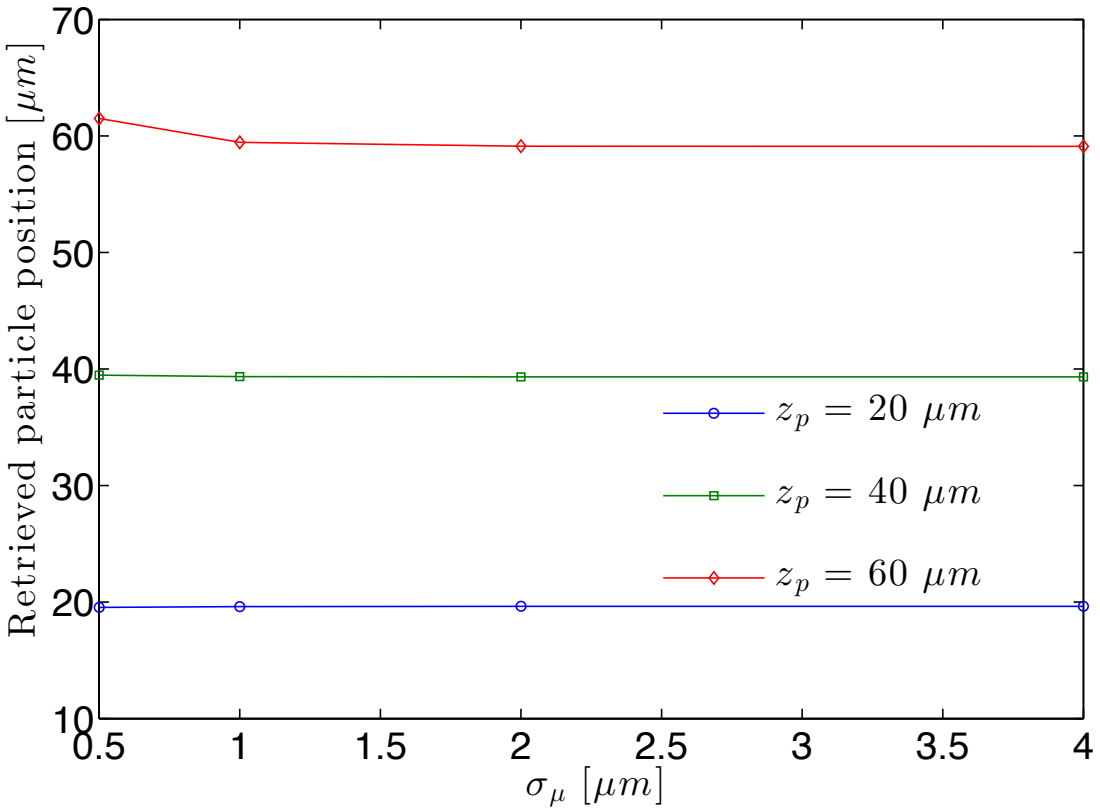

Figure 6.5: Retrieved axial positions at different coherence lengths. Three cases are considered, z_p = 20, 40 and 60 μm. The particle has fixed refractive $n_p = 1.55$ and radius $a_p = 1.0$ μm.

[34]. Interestingly, it turns out that the retrieved parameters are rather insensitive to incoherence. As shown in Fig. 6.3, 6.4 and 6.5, the fitting algorithm consistently produces correct parameters, as long as the coherence length is at least 2 μm, regardless of the particle size, refractive index or position. This is due to the fact when the coherence length is that large, the radial profile is extremely close to that of Lorenz-Mie theory. What is more intriguing is that the axial position is retrieved correctly over a vast range of coherence lengths (Fig. 6.5). This result can be partially ascribed to the special dependence of the radial profile on the coherence length (Fig. 6.1), with all maxima and minima remaining fixed even though the contrast varies significantly. Consequently, the minimum deviation can be achieved only when all peaks and valleys match, despite the fact that the curves are not identical.

6.4 Conclusions

We have investigated the effects of incoherence on particle characterization using digital holographic microscopy. A formalism describing the radial profile of a hologram using partially coherent illumination is derived analytically, and subsequently applied to a fitting algorithm, aimed at retrieving both the properties of the particle and the coherence of the illumination used. The numerical results reveal that the incoherence reduces the contrast of the hologram, while the fitting algorithm proves to be robust against incoherence. It is found that in the region that $k\sigma_\mu \gg 1$ *, the results will be indistinguishable from that of Lorenz-Mie theory. We also demonstrated the possibility of retrieving the coherence length of a partially coherent beam from measured holograms, which have implications in studying the coherence of light.

*It is worth noting that all previous works compared the coherence length with particle size because the wavelength was fixed, and Eq. (6.13) evidently confirms the sole dependence on $k\sigma_\mu$.

7. CONCLUSIONS

In this dissertation, we studied two different factors that affects the properties of light scattering: the chirality of the scatterer and the degree of coherence of the incident beam. Considerable efforts were made to understand the theoretical and practical implications of those two topics.

In Chapter 2, we did a general survey of the terminology and concepts. The Mueller matrix was introduced to characterize the single scattering properties of a particle. Specially, the effects of mirror symmetry on the structure of Mueller matrices were also investigated. In Chapter 3, we briefly reviewed the numerical methods (the Lorenz-Mie theory and DDA method) used in this dissertation. These methods served as the basic tools to compute different the Mueller matrices of different particles in the next few chapters.

In Chapter 4, we studied the light scattering of dinoflagellates based on the plywood model. We proposed details and features oriented models for a single chromosome and nucleus, and computed their Mueller matrices. Our results not only gave insights on the effects of chirality on light scattering, but also provided a potential technique to monitor and detect red tides using the backscattering signals.

In Chapter 5, we extended the Lorenz-Mie theory and the DDA method to include partially coherent light beams. After we introduced the coherence theory of light, an analytical formula was derived for the partially coherent Mueller matrix of a sphere. This formula was subsequently verified by comparing with DDA simulations. We then applied the theory to atmospherical particles such as water droplets and ice crystals. It was revealed that backscattering Mueller matrix elements are strongly correlated with the degree of coherence of the light beams, which has practical implications in remote sensing.

Finally in Chapter 6, we applied our extended Lorenz-Mie theory to study the effects

of incoherence on particle characterization using digital holographic microscopy. Relationships between the contrast of a hologram and the coherence length of the light beam were also investigated. It was proved that the digital holographic microscopy method is rather robust against incoherence. As a generalization of the conventional method, we also demonstrated that the coherence length could be extracted from the measured hologram.

REFERENCES

[1] A. Gautier, L. Michel-Salamin, E. Tosi-Couture, A. W. McDowall, and J. Dubochet, "Electron microscopy of the chromosomes of dinoflagellates in situ: confirmation of bouligand's liquid crystal hypothesis," Journal of Ultrastructure and Molecular Structure Research **97**, 10–30 (1986).

[2] T. van Dijk, D. G. Fischer, T. D. Visser, and E. Wolf, "Effects of spatial coherence on the angular distribution of radiant intensity generated by scattering on a sphere," Phys Rev Lett **104**, 173902 (2010).

[3] S. H. Lee, Y. Roichman, G. R. Yi, S. H. Kim, S. M. Yang, A. van Blaaderen, P. van Oostrum, and D. G. Grier, "Characterizing and tracking single colloidal particles with video holographic microscopy," Opt Express **15**, 18275–82 (2007).

[4] K. A. Steidinger, E. W. Truby, and C. J. Dawes, "Ultrastructure of the red tide dinoflagellate gymnodinium breve. i. general description2,3," Journal of Phycology **14**, 72–79 (1978).

[5] P. J. Rizzo, M. Jones, and S. M. Ray, "Isolation and properties of isolated nuclei from the florida red tide dinoflagellate gymnodinium breve (davis)," J Protozool **29**, 217–22 (1982).

[6] C. A. Heil and K. A. Steidinger, "Monitoring, management, and mitigation of karenia blooms in the eastern gulf of mexico," Harmful Algae **8**, 611–617 (2009).

[7] K. G. Sellner, G. J. Doucette, and G. J. Kirkpatrick, "Harmful algal blooms: causes, impacts and detection," Journal of Industrial Microbiology and Biotechnology **30**, 383–406 (2003).

[8] K. A. Steidinger, "Historical perspective on karenia brevis red tide research in the gulf of mexico," Harmful Algae **8**, 549–561 (2009).

[9] Y. Bouligand, M. O. Soyer, and S. Puiseux-Dao, "La structure fibrillaire et l'orientation des chromosomes chez les dinoflagellés," Chromosoma **24**, 251–287 (1968).

[10] R. L. Rill, F. Livolant, H. C. Aldrich, and M. W. Davidson, "Electron microscopy of liquid crystalline dna: direct evidence for cholesteric-like organization of dna in dinoflagellate chromosomes," Chromosoma **98**, 280–286 (1989).

[11] D. B. Shapiro, M. S. Quinbyhunt, and A. J. Hunt, "Origin of the induced circular-polarization in the light-scattering from a dinoflagellate," Ocean Optics X **1302**, 281–289 (1990).

[12] D. B. Shapiro, A. J. Hunt, M. S. Quinbyhunt, and P. G. Hull, "Circular-polarization effects in the light-scattering from single and suspensions of dinoflagellates," Underwater Imaging, Photography, and Visibility **1537**, 30–41 (1991).

[13] C. Bustamante, M. F. Maestre, and I. Tinoco, "Circular intensity differential scattering of light by helical structures .1. theory," Journal of Chemical Physics **73**, 4273–4281 (1980).

[14] C. Bustamante, M. F. Maestre, and I. Tinoco, "Circular intensity differential scattering of light by helical structures .2. applications," Journal of Chemical Physics **73**, 6046–6055 (1980).

[15] C. Bustamante, I. Tinoco, and M. F. Maestre, "Circular intensity differential scattering of light by helical structures .3. a general polarizability tensor and anomalous scattering," Journal of Chemical Physics **74**, 4839–4850 (1981).

[16] C. Bustamante, I. Tinoco, and M. F. Maestre, "Circular intensity differential scattering of light .4. randomly oriented species," Journal of Chemical Physics **76**, 3440–3446 (1982).

[17] S. B. Singham, C. W. Patterson, and G. C. Salzman, "Polarizabilities for light-scattering from chiral particles," Journal of Chemical Physics **85**, 763–770 (1986).

[18] D. B. Shapiro, A. J. Hunt, M. S. Quinbyhunt, M. F. Maestre, P. G. Hull, and K. Kaheng, "A theoretical and experimental-study of polarized-light scattering by helices," Ocean Optics Xi **1750**, 56–72 (1992).

[19] D. B. Shapiro, P. G. Hull, Y. Shi, M. S. Quinbyhunt, M. F. Maestre, J. E. Hearst, and A. J. Hunt, "Toward a working theory of polarized-light scattering from helices," Journal of Chemical Physics **100**, 146–157 (1994).

[20] G. Mie, "Articles on the optical characteristics of turbid tubes, especially colloidal metal solutions." Annalen Der Physik **25**, 377–445 (1908).

[21] B. T. Draine, "The discrete-dipole approximation and its application to interstellar graphite grains," Astrophysical Journal **333**, 848–872 (1988).

[22] B. T. Draine and P. J. Flatau, "Discrete-dipole approximation for scattering calculations," JOSA A **11**, 1491–1499 (1994).

[23] M. A. Yurkin and A. G. Hoekstra, "The discrete-dipole-approximation code adda: Capabilities and known limitations," Journal of Quantitative Spectroscopy & Radiative Transfer **112**, 2234–2247 (2011).

[24] L. Mandel and E. Wolf, *Optical Coherence and Quantum Optics* (Cambridge University Press, New York, 1995).

[25] M. Born and E. Wolf, *Principle of Optics* (Cambridge University Press, New York, 1999).

[26] E. Wolf, *Introduction to the Theory of Coherence and Polarization of Light* (Cambridge University Press, Cambridge, 2007).

[27] D. Cabaret, S. Rossano, and C. Brouder, "Mie scattering of a partially coherent beam," Optics Communications **150**, 239–250 (1998).

[28] J. J. Greffet, M. De La Cruz-Gutierrez, P. V. Ignatovich, and A. Radunsky, "Influence of spatial coherence on scattering by a particle," J Opt Soc Am A Opt Image Sci Vis **20**, 2315–20 (2003).

[29] D. G. Fischer, T. van Dijk, T. D. Visser, and E. Wolf, "Coherence effects in mie scattering," J Opt Soc Am A Opt Image Sci Vis **29**, 78–84 (2012).

[30] F. C. Cheong, B. Sun, R. Dreyfus, J. Amato-Grill, K. Xiao, L. Dixon, and D. G. Grier, "Flow visualization and flow cytometry with holographic video microscopy," Opt Express **17**, 13071–9 (2009).

[31] H. van de Hulst, *Light scattering by small particles* (Dover, New York, 1981).

[32] C. F. Bohren and E. E. Clothiaux, *Fundamentals of atmospheric radiation: an introduction with 400 problems* (Wiley-VCH, Weinheim, 2006).

[33] G. B. Rybicki and A. P. Lightman, *Radiative processes in astrophysics* (Wiley-VCH, Weinheim, 2008).

[34] C. F. Bohren and D. R. Huffman, *Absorption and scattering of light by small particles* (Wiley-VCH, Weinheim, 1998).

[35] D. G. Anderson and R. Barakat, "Necessary and sufficient conditions for a mueller matrix to be derivable from a jones matrix," JOSA A **11**, 2305–2319 (1994).

[36] J. Hovenier, H. Van de Hulst, and C. Van der Mee, "Conditions for the elements of the scattering matrix," Astronomy and Astrophysics **157**, 301–310 (1986).

[37] Z.-F. Xing, "On the deterministic and non-deterministic mueller matrix," Journal of modern optics **39**, 461–484 (1992).

[38] E. S. Fry and G. W. Kattawar, "Relationships between elements of the stokes matrix," Applied optics **20**, 2811–2814 (1981).

[39] C. Van der Mee and J. Hovenier, "Structure of matrices transforming stokes parameters," Journal of mathematical physics **33**, 3574–3584 (1992).

[40] E. M. Purcell and C. R. Pennypacker, "Scattering and absorption of light by nonspherical dielectric grains," The Astrophysical Journal **186**, 705–714 (1973).

[41] C. Bustamante, M. F. Maestre, D. Keller, and I. Tinoco, "Differential scattering (cids) of circularly polarized-light by dense particles," Journal of Chemical Physics **80**, 4817–4823 (1984).

[42] P. Yang and K. N. Liou, "Finite-difference time domain method for light scattering by small ice crystals in three-dimensional space," Journal of the Optical Society of America a-Optics Image Science and Vision **13**, 2072–2085 (1996).

[43] S. Sukhov, D. Haefner, J. Bae, D. Ma, D. R. Carter, and A. Dogariu, "Effect of spatial coherence on scattering from optically inhomogeneous media," J Opt Soc Am A Opt Image Sci Vis **29**, 85–8 (2012).

[44] L. Bi, P. Yang, G. W. Kattawar, and M. I. Mishchenko, "Efficient implementation of the invariant imbedding t-matrix method and the separation of variables method applied to large nonspherical inhomogeneous particles," Journal of Quantitative Spectroscopy & Radiative Transfer **116**, 169–183 (2013).

[45] M. Lahiri and E. Wolf, "Theory of refraction and reflection with partially coherent electromagnetic beams," Physical Review A **86**, 043815 (2012).

[46] G. J. Gbur, "Simulating fields of arbitrary spatial and temporal coherence," Opt Express **14**, 7567–78 (2006).

[47] X. Xiao and D. Voelz, "Wave optics simulation approach for partial spatially coherent beams," Opt Express **14**, 6986–92 (2006).

[48] B. J. Davis, "Simulation of vector fields with arbitrary second-order correlations," Opt Express **15**, 2837–46 (2007).

[49] P. H. van Cittert, "Die wahrscheinliche schwingungsverteilung in einer von einer lichtquelle direkt oder mittels einer linse beleuchteten ebene," Physica **1**, 201–210 (1934).

[50] F. Zernike, "The concept of degree of coherence and its application to optical problems," Physica **5**, 785–795 (1938).

[51] T. Iwai and T. Asakura, "Speckle reduction in coherent information processing," Proceedings of the Ieee **84**, 765–781 (1996).

[52] T. Kozacki and R. Jóźwicki, "Near field hologram registration with partially coherent illumination," Optics Communications **237**, 235–242 (2004).

[53] T. Kozacki and R. Jozwicki, "Digital reconstruction of a hologram recorded using partially coherent illumination," Optics Communications **252**, 188–201 (2005).

[54] U. Gopinathan, G. Pedrini, and W. Osten, "Coherence effects in digital in-line holographic microscopy," J Opt Soc Am A Opt Image Sci Vis **25**, 2459–66 (2008).

[55] J. P. Liu, L. Bi, P. Yang, and G. W. Kattawar, "Scattering of partially coherent electromagnetic beams by water droplets and ice crystals," Journal of Quantitative Spectroscopy & Radiative Transfer **134**, 74–84 (2014).

[56] M. Gao, P. Yang, D. McKee, and G. W. Kattawar, "Mueller matrix holographic method for small particle characterization: theory and numerical studies," Appl Opt **52**, 5289–96 (2013).

[57] (Berlin).

APPENDIX A

THE COHERENCE LENGTH OF SUNLIGHT

Here we give a brief discussion about the coherence length of sunlight. According to the van Cittert-Zernike theorem [49, 50], the radiation from a completely incoherent light source can be coherent in the far distance. This is because the propagation of the mutual coherence function which describes the degree of coherence is governed by wave equations. Given arbitrary mutual coherence function at the source and appropriate boundary condition, the mutual coherence function can be obtained by solving the wave equations [24]. Therefore, starting from the most incoherent source, defined by the following correlation function

$$\langle \phi(\mathbf{r})\phi(\mathbf{r}')\rangle = I(\mathbf{r})\delta^{(2)}\left(\mathbf{r}-\mathbf{r}'\right), \tag{A.1}$$

the field could be highly coherent at sufficiently far away.

For a thermal source like sun, Eq. (A.1) accurately approximates the correlation function of the field at two points $\mathbf{r}$ and $\mathbf{r}'$. Given the distance between the sun and the earth compared with size of the sun, the light propagating to earth is rather unilateral. This means that the Huygens-Fresnel principle can be could to compute the field at two locations $\mathbf{r}_1$ and $\mathbf{r}_2$ on earth

$$\psi\left(\mathbf{r}_1\right) = \frac{i}{\lambda}\int_S \phi(\mathbf{r})\frac{e^{ikR_1}}{R_1}d^2\mathbf{r}, \tag{A.2}$$

$$\psi\left(\mathbf{r}_2\right) = \frac{i}{\lambda}\int_{S'} \phi(\mathbf{r})\frac{e^{ikR_2}}{R_2}d^2\mathbf{r}', \tag{A.3}$$

where $R_1 = |\mathbf{r}_1 - \mathbf{r}|$, $R_2 = |\mathbf{r}_2 - \mathbf{r}'|$ and the integrals are over the surface of the sun. It

follows from the above equations that

$$\langle \psi(\mathbf{r}_1)\psi^*(\mathbf{r}_2)\rangle = \frac{1}{\lambda^2}\int_S\int_{S'} \langle \phi(\mathbf{r})\phi^*(\mathbf{r}')\rangle \frac{e^{ik(R_2-R_1)}}{R_1R_2} d^2\mathbf{r}d^2\mathbf{r}'. \tag{A.4}$$

This equation essentially describes how the correlation function propagates in space. After substituting Eq. (A.1) into Eq. (A.4), we obtain

$$\langle \psi(\mathbf{r}_1)\psi^*(\mathbf{r}_2)\rangle = \frac{1}{\lambda^2}\int_{S'} I(\mathbf{r}') \frac{e^{ik(R_2-R_1)}}{R_1R_2} d^2\mathbf{r}', \tag{A.5}$$

here R_1 is now $|\mathbf{r}_1 - \mathbf{r}'|$. The degree of coherence is then given by

$$\eta(\mathbf{r}_1, \mathbf{r}_2) = \frac{\langle \psi(\mathbf{r}_1)\psi^*(\mathbf{r}_2)\rangle}{\sqrt{I(\mathbf{r}_1)I(\mathbf{r}_2)}}, \tag{A.6}$$

where

$$I(\mathbf{r}_i) = \frac{1}{\lambda^2}\int_{S'} \frac{I(\mathbf{r}')}{R_i^2} d^2\mathbf{r}', \quad (i = 1, 2). \tag{A.7}$$

As a simplification, we assume the sun to be a disk of radius a and homogenous intensity I. Denoting $\mathbf{r}_1 = \mathbf{s}_1 r_1$, $\mathbf{r}_2 = \mathbf{s}_2 r_2$ and using the following approximation as $R_i \gg a$

$$R_i \approx r_i - \mathbf{s}_i \cdot \mathbf{r}', \tag{A.8}$$

we have

$$\eta(\mathbf{r}_1, \mathbf{r}_2) = \frac{e^{ik(r_2-r_1)}}{\pi a^2}\int_{|\mathbf{r}'|\le a} e^{-ik(\mathbf{s}_2-\mathbf{s}_1)\cdot\mathbf{r}'} d^2\mathbf{r}'. \tag{A.9}$$

We choose a special case when $r_1 = r_2 = r$ and express $\mathbf{r}_1$ and $\mathbf{r}_2$ in cylindrical coordinate

$$\mathbf{r}_1 = (\boldsymbol{\rho}_1, z) = (\rho_1\mathbf{s}_{1\perp}, z), \quad \mathbf{r}_2 = (\boldsymbol{\rho}_2, z) = (\rho_2\mathbf{s}_{2\perp}, z). \tag{A.10}$$

The integral in Eq. (A.9) can be evaluated and the result reads

$$\eta(\mathbf{r}_1, \mathbf{r}_2) = 2J_1(x)/x, \tag{A.11}$$

where $x = ka|\mathbf{s}_{1\perp} - \mathbf{s}_{2\perp}| = ka|\boldsymbol{\rho}_1 - \boldsymbol{\rho}_2|/r$ and $J_1(x)$ is the Bessel function of the first kind. Eq. (A.11) describes how the field correlates in the transverse direction. Note that $|\eta(x)|$ starts from 1 at $x = 0$ and gradually decreases to 0 in a oscillatory way as x increases. If we define the coherence length σ_μ as the distance between $\boldsymbol{\rho}_1$ and $\boldsymbol{\rho}_2$, i.e. $\sigma_\mu = |\boldsymbol{\rho}_1 - \rho_2|$, such that the degree of coherence drops to 0.5, then we find that

$$x = ka\sigma_\mu/r = 2.215. \tag{A.12}$$

Thus the coherence length is

$$\sigma_\mu = 0.353\lambda r/a. \tag{A.13}$$

Using the solid angle of the sun observed at the earth $\Delta\Omega = \pi a^2/r^2$, the coherence length can be expressed as

$$\sigma_\mu = 0.625\frac{\lambda}{\sqrt{\Delta\Omega}}. \tag{A.14}$$

Given that the sold angle of sun is about 6.79×10^{-5} sr, the coherence length at wavelength 500 nm is

$$\sigma_\mu = 0.625 \times \frac{0.5\ \mu m}{\sqrt{6.79 \times 10^{-5}}} = 38\ \mu m. \tag{A.15}$$

A more rough estimation using $\lambda/\sqrt{\Delta\Omega}$ would yield a value about 61 μm.